

Thesis for the Degree of Doctor of Philosophy

# **Improved Variational Methods in Medical Image Enhancement and Segmentation**

**Phan Tran Ho Truc**

Department of Computer Engineering

Graduate School

Kyung Hee University

Seoul, Korea

February, 2009

# Improved Variational Methods in Medical Image Enhancement and Segmentation

**Phan Tran Ho Truc**

Department of Computer Engineering

Graduate School

Kyung Hee University

Seoul, Korea

February, 2009

# Improved Variational Methods in Medical Image Enhancement and Segmentation

by

**Phan Tran Ho Truc**

Advised by

**Dr. Sungyoung Lee**

Submitted to the Department of Computer Engineering  
and the Faculty of the Graduate School of  
Kyung Hee University in partial fulfillment  
of the requirements for the degree of  
Doctor of Philosophy

## **Dissertation Committee:**

Prof. Young-Tae Park, Ph.D.....  
Prof. Oksam Chae, Ph.D.....  
Prof. Tae-Seong Kim, Ph.D.....  
Prof. Young-Koo Lee, Ph.D. ....  
Prof. Brian J. d'Auriol, Ph.D.....  
Prof. Sungyoung Lee, Ph.D.....

# Improved Variational Methods in Medical Image Enhancement and Segmentation

by

Phan Tran Ho Truc

Submitted to the Department of Computer Engineering  
on December 9, 2008, in partial fulfillment of the  
requirements for the degree of  
Doctor of Philosophy

## Abstract

Medical procedures have become a critical application area that makes substantial use of image processing. Medical image processing tasks mainly deal with image enhancement and segmentation, i.e., filtering, sharpening, and bringing out image details, and quantitatively measuring medical conditions such as vessel size, tumor volume, or bone fracture length. Over a long time, medical image processing problems were tackled by a pool of heuristic and low level mathematical operators. Simple heuristic approaches, e.g., histogram equalization, can provide surprisingly good results; however, one cannot know exactly when and why they work or do not work. Recently, the use of variational methods in image processing has emerged as an interesting research topic. Variational methods can be based on either the optimization of a energy functional or the design of a partial differential equation (PDE) whose steady state is the solution of the problem at hand. The advantage of these methods is that the theory behind the concept is well defined. However, the direct application of variational method (as it is) to medical image processing suffers from limited performance since medical images are of very poor quality. It means that purely image-driven methods can hardly work for medical images. In order to find a better solution, one has search on a solution space that is constrained by prior knowledge about the object of interest.

In this thesis, I proposed two novel variational algorithms for medical image processing that incorporate knowledge about the structure of interest (vessels, tissues, or bones, etc.) and the imaging modality which is usually known in advance. The first algorithm involved the design of a PDE for curvilinear structure enhancement. Curvilinear structures are targeted as they resemble the image representation of an important organ: blood vessel, which is critical in diagnosis of many injuries in heart, retina, or brain, etc. Here, the prior knowledge is the fact that a vessel has linear elongated structure and a Gaussian profile across its width (the intensity is highest at the vessel's center and gradually decreased towards its two sides). This is because the blood itself or the contrast agent it carries determines the contrast of the vessel, leading to higher intensity at the vessel's center and lower intensity at its sides. Unlike conventional approaches that use Hessian

tensor to detect the elongated structure and suffer from the junction suppression problem, the proposed approach utilizes directional filter bank (DFB). DFB provides more global directional information than the Hessian tensor does. The proposed approach was shown to be able to overcome the junction suppression problem.

The second algorithm involved the development of an active contour for inhomogeneous structure segmentation. Here, the prior knowledge resides in the fact that distinct organs shall generate distinct configurations (intensity) in the image. As a result, density function of the foreground (object of interest) should be at far distance from that of the background. Chan-Vese model expresses this “difference” characteristic by only the mean values of the foreground and the background, which is effective for largely homogeneous structures. However, objects in medical images, e.g., bones in CT images, are often inhomogeneous. The proposed model therefore expresses the “difference” characteristic using the whole density function itself and reflects it to the energy functional in the form of a Bhattacharyya distance. Minimization of the proposed energy functional leads to a novel active contour model that can robustly segment inhomogeneous objects.

The two proposed models have been extensively evaluated using various synthetic images as well as real medical images such as angiography and CT in comparison with many existing approaches. Experimental results showed that the proposed models provide better performances most of the time.

Thesis Supervisor: Sungyoung Lee

Title: Professor

## Acknowledgments

I would like to thank Prof. Sungyoung Lee and Prof. Young-Koo Lee, whose excellent supervising and guidance have always inspired me, not only for providing me the opportunity to carry out this work in the Ubiquitous Computing Laboratory but also for leaving me a lot of freedom to do that.

I wish to express my deep gratitude to Prof. Tae-Seong Kim, who drew my interest to variational approaches in image processing, and Prof. Md. A. U. Khan, without whose instructions the work in Chapter 3 would certainly not be accomplished. Apart from their invaluable advices and discussions, they taught me how to write my ideas down in a way that gives other people a chance to understand them as well.

Special thanks I would like to address to Prof. Ok-Sam Chae whose interesting lectures equipped me with fundamental and necessary knowledge in digital image processing.

I am also in debt of my thesis committee whose comments helped to very much improve the presentation of the thesis.

Many thanks to my friends in the Ubiquitous Computing Lab, the Bio-imaging Lab, and especially the Activity Recognition Team for their collaboration and encouragement over the last four years. Also to Leslie Lamport and Donald Knuth for L<sup>A</sup>T<sub>E</sub>X and T<sub>E</sub>X, without which I would have had much less fun formatting my thesis.

Last but not least, this thesis will never be completed without the constant support and encouragement from my family. Thank you, Mom, Dad, and Aunt 6. I also owe a lot of thanks to my brother and little sister whose efforts of taking over my duty in taking care of our parents have helped to keep my mind on this work. Very special thanks to my wife, Phuong Toan, who ensured a warm home for me to come back after hard lab. days, for her understanding and love.

# Contents

<b>List of Figures</b>	<b>10</b>
<b>List of Tables</b>	<b>12</b>
<b>1 Introduction</b>	<b>13</b>
<b>2 Variational Methods in Image Processing</b>	<b>20</b>
2.1 Diffusion Filtering . . . . .	22
2.1.1 Linear diffusion and scale-space properties . . . . .	23
2.1.2 Isotropic nonlinear diffusion . . . . .	25
2.1.3 Anisotropic diffusion . . . . .	26
2.2 Structure Tensor . . . . .	27
2.3 Hessian Tensor . . . . .	29
2.4 Directional Filter Bank . . . . .	31
2.4.1 First stage of DFB . . . . .	33
2.4.2 Second stage of DFB . . . . .	34
2.4.3 Third stage of DFB . . . . .	34
2.5 Active Contours . . . . .	36
2.5.1 Basic concepts . . . . .	36
2.5.2 Traditional AC . . . . .	40
2.5.3 Gradient Vector Flow AC . . . . .	41
2.5.4 (Original) Geometric AC . . . . .	43

2.5.5	Geodesic AC . . . . .	45
2.5.6	GVF-Geometric AC . . . . .	46
2.5.7	Chan-Vese AC . . . . .	47
2.6	Relation between Diffusion Filters and Active Contours . . . . .	49
2.7	Summary . . . . .	52
<b>3</b>	<b>Curvilinear Structure Enhancement</b>	<b>54</b>
3.1	Hessian Based Enhancement Filter . . . . .	56
3.2	DDFB Based Enhancement Filter . . . . .	57
3.2.1	Decimation-free directional filter bank . . . . .	58
3.2.2	A comparative analysis between DDFB and DFB . . . . .	63
3.2.3	Step 1: construction of directional images . . . . .	65
3.2.4	Step 2: directional image enhancement . . . . .	66
3.2.5	Step 3: recombination of enhanced directional images . . . . .	68
3.3	Application: Vessel Enhancement . . . . .	69
3.3.1	Junction suppression . . . . .	73
3.3.2	Noise sensitivity . . . . .	75
3.3.3	Real data . . . . .	79
3.3.4	Discussions . . . . .	83
<b>4</b>	<b>Inhomogeneous Object Segmentation</b>	<b>87</b>
4.1	Problems of Chan-Vese Active Contours . . . . .	89
4.2	Density Distance Augmented Chan-Vese Active Contours (Aug. CV AC) . . . . .	90
4.2.1	Implementation . . . . .	95
4.2.2	Preliminary results . . . . .	95
4.3	Application: Bone Segmentation From CT Images . . . . .	98
4.3.1	Parameter setting and tuning . . . . .	101
4.3.2	Testing data . . . . .	102
4.3.3	Evaluation method . . . . .	104

4.3.4	Sensitivity to $\beta$ . . . . .	104
4.3.5	Topology-adaptability and initialization-insensitivity . . . . .	104
4.3.6	Experiment 1 - Performance at Various Contrast Levels . . . . .	105
4.3.7	Experiment 2 - Performance at Various Noise Levels . . . . .	109
4.3.8	Experiment 3 - Performance with Real Data . . . . .	109
4.3.9	Discussions . . . . .	113
<b>5</b>	<b>Contributions and Conclusions</b>	<b>115</b>
	<b>Publications</b>	<b>119</b>
	<b>Bibliography</b>	<b>122</b>

# List of Figures

2-1	Smoothing a vessel image with Gaussian kernel of different scales. . . . .	24
2-2	Example of coherence-enhancing diffusion. . . . .	30
2-3	The directional filter bank structure. . . . .	32
2-4	Downsampling and rotation effects of Quincunx matrix $Q$ . . . . .	33
2-5	Eight sample directional subbands of an image. . . . .	35
2-6	Natural topological change handling of the level-set method. . . . .	39
2-7	Inability to move into boundary concavities of a traditional snake. . . . .	42
2-8	Sample result of the gradient vector flow snake. . . . .	44
2-9	All possible relative positions of the curve with respect to the object. . . . .	48
2-10	De-noising a retinal image with self-snakes. . . . .	51
2-11	Taxonomy of variational methods in image processing. . . . .	53
3-1	Block diagram of the proposed enhancement framework. . . . .	59
3-2	The decimation-free directional filter bank structure. . . . .	61
3-3	Rules used to shift resampling and downsampling matrix to the right. . . . .	62
3-4	Eight sample directional images obtained using DDFB. . . . .	64
3-5	Results of non-uniform illumination removal using homomorphic filter. . . . .	66
3-6	Angiography images with typical hindrances for accurate vessel-tree reconstruction. . . . .	70
3-7	Block diagrams of conventional Hessian-based and correlation-based approaches. . . . .	72

3-8	Vessel enhancement results for a synthetic image. . . . .	74
3-9	Testing data with a size of $512 \times 512$ and various amount of white noise. . .	77
3-10	Sample vessel enhancement results. . . . .	78
3-11	Performance plots of various enhancement filters vs. noise levels. . . . .	79
3-12	Qualitative enhancement results for two cardiac angiography images. . . . .	80
3-13	Best and worst enhancement results for the Utrecht database in terms of AUC measures. . . . .	81
3-14	Performance plots vs. sample number for the Utrecht database. . . . .	82
3-15	Mean and SD bar plots of AUC vs. noise levels for 40 noise-added ground truths of the retinal images. . . . .	84
3-16	The coordinates $Oxy$ is rotated to $Ox'y'$ by a counterclockwise angle $\theta$ . . .	86
4-1	Failure of the Chan-Vese active contour on capturing an inhomogeneous object. . . . .	90
4-2	CV fitting term $F(C)$ at every iteration of the CV AC evolution process. .	91
4-3	Results of the Aug. CV AC with various values of $\beta$ . . . . .	96
4-4	CV fitting term $F(C)$ at every iteration of the Aug. CV AC evolution process.	97
4-5	Segmentation result for a CT image. . . . .	97
4-6	Typical CT bone images with challenging obstacles for accurate segmentation.	99
4-7	Real CT data set. . . . .	103
4-8	Performances of Aug. CV AC applied on the real CT data set vs. $\beta$ values.	105
4-9	Topology-adaptability and initialization-sensitivity of various AC models. .	106
4-10	Performance at various contrast levels. . . . .	107
4-11	Plots of error means vs. contrast levels. . . . .	107
4-12	Performance at various noise levels. . . . .	110
4-13	Plots of error means vs. SNR. . . . .	110
4-14	Two sample CT image segmentation results of five various AC models. . . .	111
4-15	Qualitative performance comparison between CV AC and Aug. CV AC and the 3D-DOCTOR software. . . . .	112

# List of Tables

3.1	Mean and SD of the AUC of the three methods performed on the Utrecht database. . . . .	83
4.1	Level-set parameters of the classical AC models. . . . .	89
4.2	Parameter settings for Experiment 1. . . . .	106
4.3	Mean and SD of error measures for Contrast data set. . . . .	108
4.4	Parameter settings for Experiment 2. . . . .	109
4.5	Mean and SD of error measures for Noisy data set. . . . .	111
4.6	Parameter settings for Experiment 3. . . . .	111
4.7	The mean and SD of error measures of AC models and the 3D-DOCTOR software performed on sixteen CT images. . . . .	113

# Chapter 1

## Introduction

Image processing is an important component of modern technologies because human depends so much on the visual information. About 99% information we perceive about the world is obtained with our eyes [111]. In other words, images are better than any other information form for us to perceive. A digital image is an image of a continuous world obtained by sampling and quantization. The idea is to superimpose a regular grid on an analogue image and to assign a discrete quantity to each square of the grid. Mathematically, a digital image may be defined as a two-dimensional function,  $I(x, y)$ , where  $x$  and  $y$  are spatial coordinates. Each pair of coordinates  $(x, y)$  is called a *pixel*, for picture element, and its value,  $I$ , represents for a certain feature of the image. For example, it can be the intensity, described by a single band (0 to 255) in gray-scale images, a vector field of two components, or a color vector of three bands: red, green, and blue. Another important characteristic of an image is its resolution (or size). It is the number of rows and columns in the image. The higher the resolution, the closer the digital image to the physical world.

A digital image processor can be thought of as an input-output system, where the input  $I_0$  is an acquired image and the output  $F = T[I_0]$  can be generally any combinations of features that are visually meaningful. For example,  $F$  could be a de-noised version of the input image, the layout of object boundaries, the disjoint regions associated with distinct

objects, or the relative depth of different objects in a scene. In general, given the targeted feature  $F$  is known, it is often possible to find a *forward problem* that generates an image observation  $I_0$  from  $F$ . However, most image processing problems are ill-posed *inverse problems*, i.e., one has to recover or detect  $F$  from  $I_0$ . This inversion is either instable or non-unique and thus is ill-posed. That is the reason why designing and computing  $T$  are challenging and there exist no invasive methods that work for most of the image processing problems.

Digital image processing has impact on many technical endeavor areas. The first one to mention is remote sensing, an application field where people need to analyze, measure, or interpret scenes at a distance. Image acquisition used for these purposes is usually based on the visual and infrared bands of the electromagnetic spectrum. The mission of image processing here is to provide tools to track and quantify changes in forests, water supplies, urbanization, pollution, etc. or to observe and forecast weather. Also using the visual bands, video surveillance is another important area. The main task here is to detect unusual activity of an object by analyzing its motion from a sequence of frames. In robotics, images acquired from optical robotic sensors must be processed with accounting for perspective geometry and photogrammetric distortions. The processed images here are used to support autonomous navigation, target identification, and threat avoidance. Many other applications where image processing is involved include character recognition, fingerprint analysis, quality control, and 3-D reconstruction of scenes from images.

Medical procedures have also become a critical area that makes substantial use of image processing. Medical images can be acquired using various modalities such as classical X-ray imaging or modern computer aided CT, MRI, and PET imaging which are based on a wide spectrum ranging from gamma rays, X-rays, to ultrasounds. Whereas image processing tasks in the above-mentioned fields are performed independently by a machine, depending on the development of artificial intelligence algorithms, medical image processing is often

a partnership of human and machine. Medicine is clearly of human enterprise. The detections of pathologies like stenoses or lesions often require decisions from a medical expert and are ill-suited for execution by a computer. In contrast, computers are more suitable for preprocessing tasks of filtering, sharpening, and bringing out image details or for quantitative measurement of medical conditions such as vessel size, tumor volume, or bone fracture length. These types of processes are tedious and require high accuracy as well as maximal result reproducibility which cannot be guaranteed in human manual processes.

Medical image processing can therefore be roughly grouped into three categories:

- *Enhancement*: Medical images are often noisy due to the acquisition process and the objects of interest are not well distinguished from others. Enhancement is to bring out obscured details in an image to improve their appearance. Enhancing vessels in low contrasted X-ray angiography images or tumor detection from CT images is such an example.
- *Segmentation*: This is the task to partition an image into disjoint regions corresponding to distinct organs or objects.
- *Registration*: This task involves the fusion of various information from multiple imaging modalities, leading to a more powerful diagnostic tool.

Over a long time, medical image processing problems were tackled by a pool of low level mathematical operators. These methods are largely heuristic and originated from 1-D signal processing theory, treating the matter as a high-dimensional form. They mainly involve in filtering (linear or not), frequency analysis, and some basic concepts of probability and statistic. This type of processing treats images as complicated audio or radio-frequency signals, reflecting a bias towards electrical engineering. They are, however, very common and often covered by any image processing textbook; see e.g., [50] for more details.

To date, more sophisticated tools have been developed, emerging in three main directions [23]: stochastic modeling, wavelets, and variational approaches. Stochastic modeling considers an image either as a composition of an ideal (deterministic) image with some random part or as a typical sample of a random field like Markov random field. The methods in this category include statistical pattern theory, learning theory, Bayesian inference theory for signal and parameter estimation, and stochastic algorithms such as Monte-Carlo simulation, simulated annealing, and the EM algorithm. These methods are suitable for images with statistical nature. They are even more powerful when combined with filtering techniques, dealing with transformed feature spaces rather than pixel domains.

Wavelet theory is inherited from signal processing and decomposition techniques. Unlike Fourier transform, which mixes long-range spatial information and thus makes itself less ideal for handling localized visual features like edges, wavelets present locality using localized bases, which are organized according to different scales or resolutions. Apart from spatial localization, wavelets are able to reveal important visual cues such as jumps or edges: wavelet coefficients of a generic piecewise smooth image have significant values along those discontinuities but are mostly negligible at others. Hence, wavelets are efficient tools for adaptive image representation and compression.

Variational techniques primarily refer to the optimization of cost functions. All one need to do is to define a cost functional or energy functional which characterizes the image structure that one desires to enhance or detect. Then, the optimization of the cost function is usually implemented using the calculus of variations, leading to a partial differential equation (PDE) whose steady state corresponds to the solution of the visual perception task. In some cases, there exist variational methods that directly design such a PDE without defining any energy functional. Traditionally applied in physics, variational methods have gained significant attention over the past decade in addressing image restoration and enhancement, image segmentation, tracking, and stereo reconstruction among other

problems.

Among many techniques aforementioned, I focus on variational methods in this thesis due to several reasons. Firstly, most of the existing methods can be recast variationally; see [23] for a demonstration of intrinsic interconnection between various approaches. Secondly, unlike in heuristic algorithms, the theory behind the concept in variational methods is well established. Energy functionals and PDEs are, of course, written in a continuous setting, making the existence and the uniqueness of the solution able to be proven. It is the theory of *viscosity solutions* [29] that makes this feasible because digital images are often not smooth enough to yield derivatives in classical sense. Once those proofs are obtained, what one needs to do next is just to discretize the PDEs using available and extensive numerical schemes which belong to a mature research field nowadays. I think that it is easier to understand the physical realities and then to stimulate the intuition necessary to propose new models by reasoning in a continuous framework.

Thirdly, without a guiding variational principle, heuristic approaches become very complex. Using an energy functional and a descent algorithm, one can easily state when one result (e.g., segmentation) is better than another.

Finally, the use of the calculus of variations in the optimization process is an important strength that allows one to integrate many terms and build quite complicated cost functionals to cope with the problem at hand. So, with variational framework, it is easier to incorporate knowledge about the structure to be analyzed. In medical image analysis, the use of prior knowledge is particularly attractive since the structure of interest (vessel, tissue, or bone) as well as the imaging modality are usually known in advance. Also, it arises by necessity: medical image quality is usually so poor that a given processing task has to search on a solution space that is constrained with prior knowledge in order to find a sensible solution. Moreover, the use of prior knowledge, given in the form of a model, reduces the number of degrees of freedom compared to model-free analysis.

A common way to incorporate prior knowledge is that one first defines a set of features (color, shape, size, texture, ...) which can be obtained from a training set or directly given by the user and then performs model matching to detect objects that have features matched with the pre-defined features [125, 107, 66, 92]. I consider this way as extrinsic knowledge usage. The methods belonging to this category would require more efforts from the user as compared to approaches that may identify, extract, and make use of intrinsic knowledge. It is my conviction that there exists intrinsic knowledge usage in medical image processing such that better performance can be obtained without requiring additional efforts to select training set or define feature constraints. By intrinsic knowledge, I mean the knowledge about the characteristics an object has by its very nature, regardless of its environment or situation. For example, a blood vessel intrinsically has curvilinear structure or knee bone has inhomogeneous nature.

This work explores the intrinsic knowledge-incorporated variational methods in medical image processing. Both technical and medical research communities have left their imprint on the thesis: the chapters report on the development and evaluation of enhancement and segmentation algorithms for medical imagery. Enhancement and segmentation are targeted because they are very fundamental tasks in medical image processing as introduced above and other processing like registration can efficiently performed using their results. Specifically, Chapter 2 briefly reviews existing variational methods in the literature. The first part of Chapter 3 introduces a novel method to enhance curvilinear structures in an image. The main idea is to adapting Hessian-based filters to be used in directional images obtained using directional filter bank (DFB), which permits the directional estimation without Hessian eigen-analysis. Here, the intrinsic elongated characteristic of the structure of interest makes it naturally suitable for analysis using DFB. Then, in the latter part of the chapter, the method is applied to enhance vessels in angiography images which is an important process in vascular disease diagnosis or surgery

planning and performing. In a similar presentation manner, Chapter 4 describes my proposed active contour (AC) model for image segmentation and evaluates its performance as a technique for automatic bone segmentation from CT images in comparison against that of classical AC models and a commercial software. Bones in CT images are chosen as the regions of interest since they have several segmentation challenges such as weak edges, gaps on edges, texture areas, and blurred inter-bone regions. Here, the intrinsic knowledge, reflected in the proposed energy functional, are the facts that bone regions in CT images are highly inhomogeneous and their characteristics are statistically different from that of the background. Finally, the contributions are summarized and concluded in Chapter 5 before the bibliography.

## Chapter 2

# Variational Methods in Image Processing

As introduced in Chapter 1, variational methods can be based on either the optimization of a energy functional or the design of a PDE whose steady state is the solution of the problem at hand. The ideas of using variational methods in image processing can be traced back at least to Jain [54] in 1977. However, the field did not attract much research interests until the concept of *scale space* was introduced in two independent works [59] and [137]. In this concept, an image is represented and analyzed at multiple scales. Multiscale analysis is natural in vision because objects become larger if one moves close to the scene and smaller if one moves away. Hence, suppose that one is looking for a face in an image; it can occupy either the whole image or just a tiny part of it. This is different from other sensing such as tactile sensing in which an object's size obtained by tactile sensor always remains same since one has to touch the object in order to sense it or auditory sensing in which one specific temporal scale is given to the vibration of one's vocal cord. In these two seminal works, multiscale representation of an image was obtained using Gaussian filtering at various scales, which was proven to be equivalent to deforming the image at various

amount of time based on the classical heat equation, leading to an *isotropic diffusion* flow.

Then, in early 1990s, Perona and Malik proposed a *nonlinear diffusion* filter [100] which later became one of the most influential works in the field. Unlike isotropic diffusion in which the information is diffused equally everywhere, nonlinear diffusion limits the diffusivity around some areas of interest like edges in order to preserve them. The work opened up a large number of researches on PDE-based image processing community both theoretically and practically [5, 109, 90, 104, 127, 136]. Especially, in [132, 133], Weickert proposed to further control the diffusivity not only at preferred locations but also at certain directions. The model is thus called *anisotropic diffusion* filter, which was shown to be very effective in enhancing coherent structures. To determine the direction of the structure, many approaches have been used, ranging from local ones like *structure tensor* or *Hessian tensor* to more global tools like directional filter bank, which all will be described in this chapter.

It was proven by many research groups that the famous *mean curvature motion* [42, 4] (sometimes called *geometric heat flow*) can also define a scale space. This flow has therefore been utilized in solving a number of image processing problems, especially segmentation. The idea is to move a curve or surface with the velocity determined by its curvature. Such a curve is called active contour or snake which was first introduced by Kass et al. [57]. Apart from the direct designs of curvature-based PDEs, the Mumford-Shah energy functional for segmentation [84] is also an influential work that has initiated many segmentation models. Another crucial contribution to the area is the level-set method developed by Osher and Sethian [91]. This approach not only provides an efficient means for numerical implementations of active contours but also naturally solves the hard problem of topological change handling which took up a lot of efforts previously.

The goal of this chapter is to give an overview of the above-mentioned techniques based on which two novel models for medical image processing were proposed and will be

introduced in the following chapters.

## 2.1 Diffusion Filtering

Diffusion filtering has become a powerful and well-established tool in image enhancement. The basic idea is to smooth an image using the *diffusion equation*, which is known as the *heat equation* in many physical processes

$$\frac{\partial I(\mathbf{x}, t)}{\partial t} = \operatorname{div} (D \cdot \nabla I) \quad (2.1)$$

where  $I(\mathbf{x}, 0) = I_0 : \mathbb{R}^2 \rightarrow \mathbb{R}$  is the input image,  $\mathbf{x} = (x, y)$  the spatial location,  $t$  an artificial time variable,  $\nabla I$  the gradient of the image, and  $D$  the *diffusion tensor*, which is a positive definite symmetric matrix. Here, image intensity is considered as mass concentration and accordingly the intuition of diffusion is to balance concentration differences without creating or destroying mass. The process where a pixel gains less mass from its larger neighbors than it loses to its smaller neighbors is called *forward diffusion*. The reverse process is *backward diffusion*, where a pixel loses less mass to its smaller neighbors than it obtains from its larger neighbors. If  $D$  is replaced by a positive scalar-valued *diffusivity*  $g$ , one has *isotropic* diffusion, where the information is diffused equally in all directions, as opposed to *anisotropic* in the general case, where diffusion in some directions is more emphasized than in others. The general isotropic diffusion equation is then written as

$$\frac{\partial I(\mathbf{x}, t)}{\partial t} = \operatorname{div} (g \nabla I) \quad (2.2)$$

where  $g$  is any scalar-valued function.

### 2.1.1 Linear diffusion and scale-space properties

The simplest isotropic diffusion corresponds to the case where the diffusivity  $g$  is constant over the whole image. In particular, when  $g = 1$ , one obtain

$$\partial_t I = \Delta I = \operatorname{div}(\nabla I) \quad (2.3)$$

where  $\Delta$  denotes the Laplacian operator. The solution is given by

$$I(\mathbf{x}, t) = \left( G_{\sqrt{2t}} * I \right) (\mathbf{x}) \quad G_\sigma(\mathbf{x}) = \frac{1}{2\pi\sigma^2} \exp\left(-\frac{\mathbf{x}^2}{2\sigma^2}\right) \quad (2.4)$$

meaning that stopping the evolution process after a time  $t \geq 0$  is equivalent to the convolution of the input image with a Gaussian kernel  $G_\sigma$  with standard deviation  $\sigma = \sqrt{2t}$  [131]. Larger values of  $t$  yield larger levels of smoothing; see Figure 2-1. This defines a *scale space* for the image, which is a family of gradually smoother versions of it. Note that any scale  $t_i$  can be obtained either from a scale  $t_j$  ( $t_j < t_i$ ) or from the original image. The scale space analysis provides a step to semantical description of an image from a pixel basis because it introduces a hierarchy of image features. This theory is more than 20 years old [134] and detailed treatment of its various aspects can be found in [69, 119] and the references therein.

Gaussian filtering (2.4) is regarded as a (standard) linear approach to reduce additive noise. As can be seen in Figure 2-1, the image gets more and more simplified and noise is removed very well. However, the method suffers from two major disadvantages. One is, important features such as edges are smoothed as well and thus harder to be detected. The other is, the locations of edges are dislocated when moving from finer to coarser scales. To find the right location of structures at a coarse scale, one has to trace back to the original image [137], which is not an easy task, especially when junctions and bifurcations are involved.

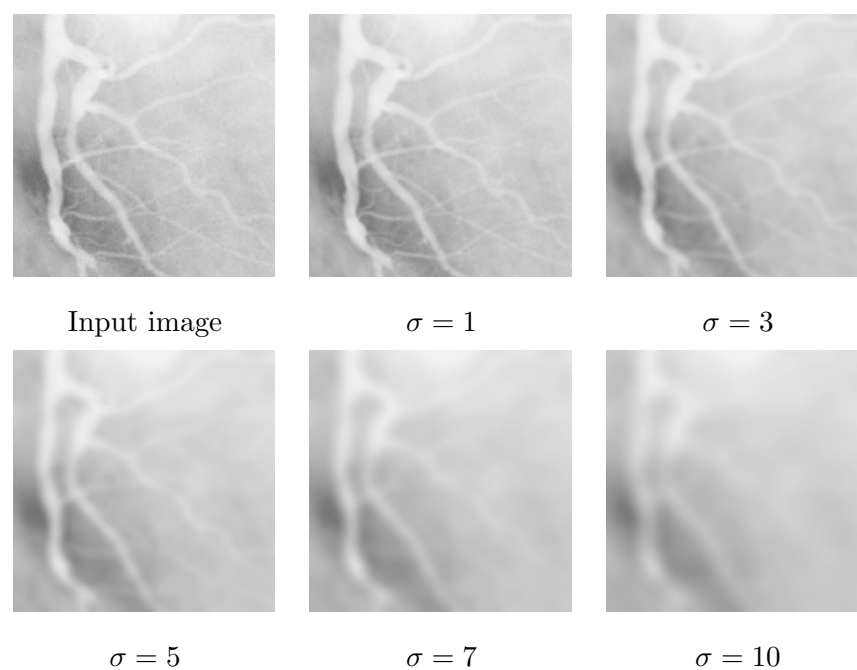


Figure 2-1: Smoothing a vessel image with Gaussian kernel of different scales. Note how small vessels are gradually removed when the scale increases.

### 2.1.2 Isotropic nonlinear diffusion

A natural way to alleviate both problems of linear diffusion is to introduce a location-dependent diffusivity that limits or stops the diffusion in important areas, leading to a nonlinear isotropic diffusion. For example, one wishes to obtain a denoising process that preserves the edges' contrast and location. Then, one can use an edge-stopping function  $g(|\nabla I|)$  satisfying  $g(s) \rightarrow 0$  as  $s \rightarrow +\infty$ . Here,  $|\nabla I|$  serves as an edge detector: higher value of  $|\nabla I|$  corresponds to higher likelihood to be an edge. The diffusion equation then reads

$$\partial_t I = \operatorname{div} (g(|\nabla I|) \nabla I). \quad (2.5)$$

Since the diffusivity  $g$  is a decreasing function which approaches 0 in the vicinity of an edge, it reduces the smoothing amount around edges. The outcome of the filter depends considerably on choosing this function. The first formulation of this kind was introduced by Perona and Malik [100] who proposed two different diffusivity functions:

$$g(|\nabla I|) = \frac{1}{1 + |\nabla I|^2 / \lambda^2} \quad (2.6)$$

$$g(|\nabla I|) = \exp\left(-\frac{|\nabla I|^2}{2\lambda^2}\right) \quad (2.7)$$

where  $\lambda > 0$  is a so-called *contrast parameter*. To study the behavior of this parameter, let's consider the 1-D case for simplicity and denote  $\Phi(\partial_x I) \equiv g(|\partial_x I|) \partial_x I$ , leading to

$$\partial_t I = \partial_x (\Phi(\partial_x I)) = \Phi'(\partial_x I) \Delta I. \quad (2.8)$$

Two formulations of  $\Phi'(\partial_x I)$  corresponding to two diffusivity functions in (2.6) and (2.7) can be derived as

$$\Phi'(\partial_x I) = \frac{\lambda^2 (\lambda^2 - |\partial_x I|^2)}{(\lambda^2 + |\partial_x I|^2)^2} \quad (2.9)$$

$$\Phi'(\partial_x I) = (1 - |\partial_x I|^2 / \lambda^2) \exp\left(-\frac{|\partial_x I|^2}{2\lambda^2}\right). \quad (2.10)$$

In both cases,  $\Phi'(\partial_x I) > 0$  (i.e., forward diffusion) if  $|\partial_x I| < \lambda$  and vice versa,  $\Phi'(\partial_x I) < 0$  (i.e., backward diffusion) if  $|\partial_x I| > \lambda$ . Forward diffusion smooths the contrasts and backward diffusion enhances them. Therefore, contrast parameter  $\lambda$  determines how large the gradient of an edge must be in order for the edge to be preserved.

We should note that studying the stability of the above model is not trivial. Of course, a reasonable regularization provided by numerical schemes can stabilize the process. However, to reduce the dependence of stabilization on numerical implementations, one can apply spatial regularization directly on the continuous equation. Catta et al. [22] proposed to replace the diffusivity  $g(|\nabla I|)$  of the Perona-Malik model by  $g(|\nabla I_\sigma|)$  where  $I_\sigma = G_\sigma * I$ , leading to

$$\partial_t I = \operatorname{div} (g(|\nabla I_\sigma|) \nabla I). \quad (2.11)$$

In [135, 68], the parameters  $\sigma$  and  $\lambda$  were made time-dependent. The spatial regularization with additional *scale parameter*  $\sigma$  helps the Perona-Malik model eliminate false edges caused by noises.

### 2.1.3 Anisotropic diffusion

All diffusion schemes discussed so far (linear or not) rely on a scalar-valued diffusivity and thus are isotropic, i.e., the diffusion amount is same in all directions. In some applications where edges are noisy, it is desirable to reduce the diffusion across edges only while maintaining the smoothing along edges. These requirements can be satisfied by replacing the scalar-valued diffusivity with a matrix-valued diffusion tensor  $D$  which is constructed by defining its orthogonal eigenvectors and eigenvalues. The main idea is to align the eigenvectors to the directions along which the contrast is smoothed and assign the smoothing amount to the corresponding eigenvalues. For example, one can construct the eigenvectors  $\mathbf{v}_1, \mathbf{v}_2$  of  $D$  such that  $\mathbf{v}_1 \parallel \nabla I_\sigma$  and  $\mathbf{v}_2 \perp \nabla I_\sigma$  and choose the corresponding eigenvalues

$\lambda_1$  and  $\lambda_2$  as

$$\lambda_1 = g(|\nabla I_\sigma|) \quad (2.12)$$

$$\lambda_2 = 1. \quad (2.13)$$

The diffusion tensor is then calculated as  $D = Q \text{diag}(\lambda_i) Q^T$  where  $Q$  is a matrix comprised of the normalized  $\mathbf{v}_1$  and  $\mathbf{v}_2$  as its columns. The resulting filter will limit the diffusion in  $\mathbf{v}_1$  direction (across edges) while allow constant smoothing in  $\mathbf{v}_2$  direction (along edges).

Another motivation for introducing direction-specific smoothing arises from cases where coherent flow-like structures are to be enhanced [132, 133]. To this end, sophisticated structure descriptors other than  $\nabla I_\sigma$  are needed. Such tools can be obtained using *structure tensor*, *Hessian tensor*, or *directional filter bank*, which are described next.

## 2.2 Structure Tensor

Structure tensor (a.k.a. *second-moment matrix* or *scatter matrix*) is a matrix field that can be used in orientation estimation and image structure analysis. Since it was first introduced in [45] and in [14] in an equivalent formulation, structure tensor has shown its usefulness in many computer vision tasks such as corner detection [45, 53], diffusion filter [132, 133], texture analysis [106, 15, 73], and optical flow calculation [15, 16].

A simple orientation-estimation at a pixel  $\mathbf{x}$  can be obtained using the gradient information  $\nabla I(\mathbf{x})$ . However, images are often noisy, making the estimates different from the real orientation at the respective pixel. Also, from a practical perspective, one is more interested in the dominant orientation in a neighborhood of a pixel rather than its very local orientation. Therefore the gradient at a specific pixel is replaced with the structure information of its neighbors weighted by a Gaussian kernel. This is done by convolving the gradient with a Gaussian window, leading to  $\nabla I_\sigma$  as an orientation approximation.

Nevertheless, Gaussian smoothing of the gradient can cause cancelation effects in some

structures such as thin lines. The gradient is positive at one side of the line whereas negative at the other side. Thus they are likely to cancel each other out during smoothing. To avoid this problem, the structure tensor is given in form of a outer product of the gradient, leading to a symmetric positive semi-definite matrix

$$J_0 = \nabla I \nabla I^T = \begin{bmatrix} (\partial_x I)^2 & \partial_x I \partial_y I \\ \partial_x I \partial_y I & (\partial_y I)^2 \end{bmatrix}. \quad (2.14)$$

$J_0$  is referred to as the *unsmoothed structure tensor*. For a certain neighborhood of scale  $\rho$ , the structure tensor is computed as

$$J_\rho = G_\rho * J_0. \quad (2.15)$$

The smoothing of the structure tensor has the same effect of that of the gradient  $\nabla I_\sigma$ , i.e., it increases the accuracy of the orientation estimation in real images since it makes the structure tensor more robust to noise. Besides, smoothing allows to estimate the dominant orientation at the neighboring pixels where the gradient is close to zero. The dominant orientation is determined as the structure tensor's eigenvector associated with the largest eigenvalue. This can be proved using least square error method; see [128]. The total square error between the estimated orientation  $\mathbf{q}$  and the gradient calculated on a neighborhood of scale  $\rho$  is

$$\int_{\Omega} G_\rho |\nabla I - (\nabla I^T \mathbf{q}) \mathbf{q}|^2 d\mathbf{x} = \int_{\Omega} G_\rho [\nabla I^T \nabla I - \mathbf{q}^T (\nabla I \nabla I^T) \mathbf{q}] d\mathbf{x} \quad (2.16)$$

where  $\Omega$  is the image domain and  $(\nabla I^T \mathbf{q}) \mathbf{q}$  the projection of  $\nabla I$  on  $\mathbf{q}$ . Minimizing the error is equivalent to maximizing

$$\int_{\Omega} G_\rho \mathbf{q}^T (\nabla I \nabla I^T) \mathbf{q} d\mathbf{x}. \quad (2.17)$$

Because  $\mathbf{q}$  is independent on  $\mathbf{x}$  within the Gaussian window, this leads to maximizing

$$\mathbf{q}^T \left( \int_{\Omega} G_\rho (\nabla I \nabla I^T) d\mathbf{x} \right) \mathbf{q} = \mathbf{q}^T J_\rho \mathbf{q}. \quad (2.18)$$

Thus, the orientation  $\mathbf{q}$  that satisfies the least square error criterion is the eigenvector associated with the largest eigenvalue of the structure tensor  $J_\rho$ .

In general, the smoothed structure tensor is not singular and its eigenvalues  $\mu_1, \mu_2$  reveal three different structures:

- $\mu_1 \approx \mu_2 \approx 0$ : homogeneous areas, almost no principal direction
- $\mu_1 \approx 0, \mu_2 \gg 0$ : lines, one principal direction
- $\mu_1 \gg 0, \mu_2 \gg 0$ : corners, more than one principal direction.

Since  $\mu_2 \geq \mu_1$ , its corresponding eigenvector  $\mathbf{q}_2$  is the orientation across edge whereas the other eigenvector  $\mathbf{q}_1$  gives the coherence direction. The coherence information can be measured by, e.g.,  $(\mu_2 - \mu_1)^2$ .

Due to the above characteristic, structure tensor was successfully used in anisotropic diffusion filter to enhance coherent structures [132, 133]. To this end, the diffusion tensor  $D$  is designed to have eigenvectors same as  $J_\rho$  with the corresponding eigenvalues chosen as

$$\begin{aligned} \lambda_1 &= \begin{cases} \eta & \text{if } \mu_2 = \mu_1, \\ \eta + (1 - \eta) \exp\left(-\frac{C}{(\mu_2 - \mu_1)^{2n}}\right) & \text{else,} \end{cases} \\ \lambda_2 &= \eta \end{aligned} \tag{2.19}$$

where  $n \in \mathbb{N}$ ,  $C > 0$ , and  $\eta \in (0, 1)$ . Figure 2-2 shows a sample result of this filter applied to enhance a fingerprint whose coherent structure is of particular importance.

## 2.3 Hessian Tensor

Similar to the gradient and the structure tensor which use first-order derivative to determine the dominant orientation, the Hessian tensor considers second-order derivative. The

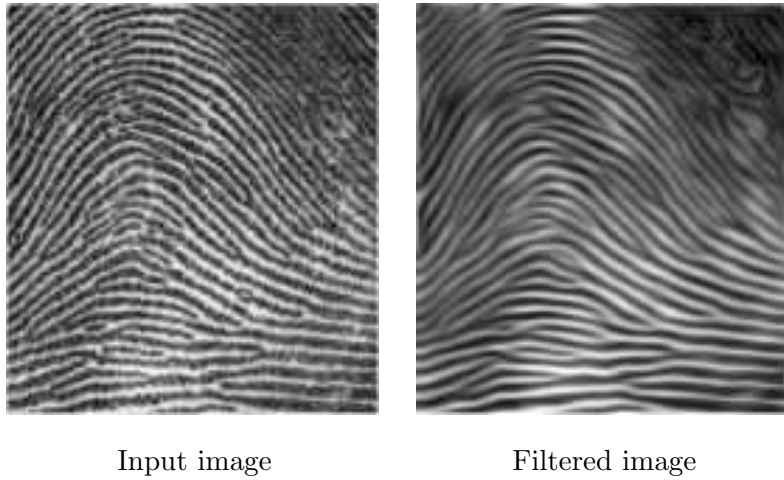


Figure 2-2: Example of coherence-enhancing diffusion (2.19). Noise is removed while important structure is maintained and even enhanced.

Hessian matrix of a image  $I(x, y)$  is given by

$$\begin{bmatrix} \partial_{xx}I & \partial_{xy}I \\ \partial_{xy}I & \partial_{yy}I \end{bmatrix}. \quad (2.20)$$

The Hessian's eigenvector corresponding to the largest eigenvalue (in magnitude) is considered as the orientation across the image feature (edge) and the other eigenvector (its perpendicular orientation) the orientation along image feature.

For line-like structures, there are two main reasons to use second-order derivatives rather than first-order derivatives [19]. One is, line-like structures are characterized by oscillations and thus yield large second-order derivatives but do not generate large first-order derivatives. The other is, edges yield large first-order derivatives at their centers while generating large second-order ones at their sides. This is important because information about the centers only is not enough to capture the whole lines of different widths. In Hessian-based approaches, a line-like structure is declared when the ratio between the minimum and maximum principal curvatures, which are determined by the Hessian eigen-

values, is low. And its direction is considered to be the eigenvector corresponding to the smallest eigenvalue in absolute value. This information was exploited in [48, 114, 62, 118] to enhance blood vessels in medical images, which will be described more in the following chapter.

## 2.4 Directional Filter Bank

All the structure descriptors mentioned so far provide the structure information limited to a local neighborhood. For applications dealing with edges, being local can be an advantage as edge point is a local event. In fact, as can be seen above, the nonlinear diffusion filters and related PDE schemes enjoy such advantage and provide very impressive performances. On the other hand, treatment of edge curve which consists of connected edge points requires less local methods. Directional filter bank (DFB), introduced by Bamberger and Smith [8], is such a method. It was shown that DFB can decompose the spectral region of an input image into  $n = 2^k$  ( $k = 1, 2, \dots$ ) wedge-shaped like passbands which correspond to linear features in a specific direction in spatial domain. Although there are similar methods such as fan filters and wavelets, DFB is unique in its ability to provide nonredundant subbands with a high angular resolution, precise reconstruction, and computational efficiency. Initially, DFB was designed to provide image compression [10]. Later on in [97, 11], it was used in collaboration with directional energy for image enhancement purpose. Recently in [95], DFB and directional energy were tuned to provide fingerprint recognition.

One major drawback of the original DFB proposed in [8] was that subbands become visually distorted due to frequency aliasing. One possible solution to this was provided by Park et al. [98], where it was pointed out that frequency aliasing was produced due to non-diagonalization of overall downsampling matrix. Then the authors proposed a new DFB structure in [99] as follows.

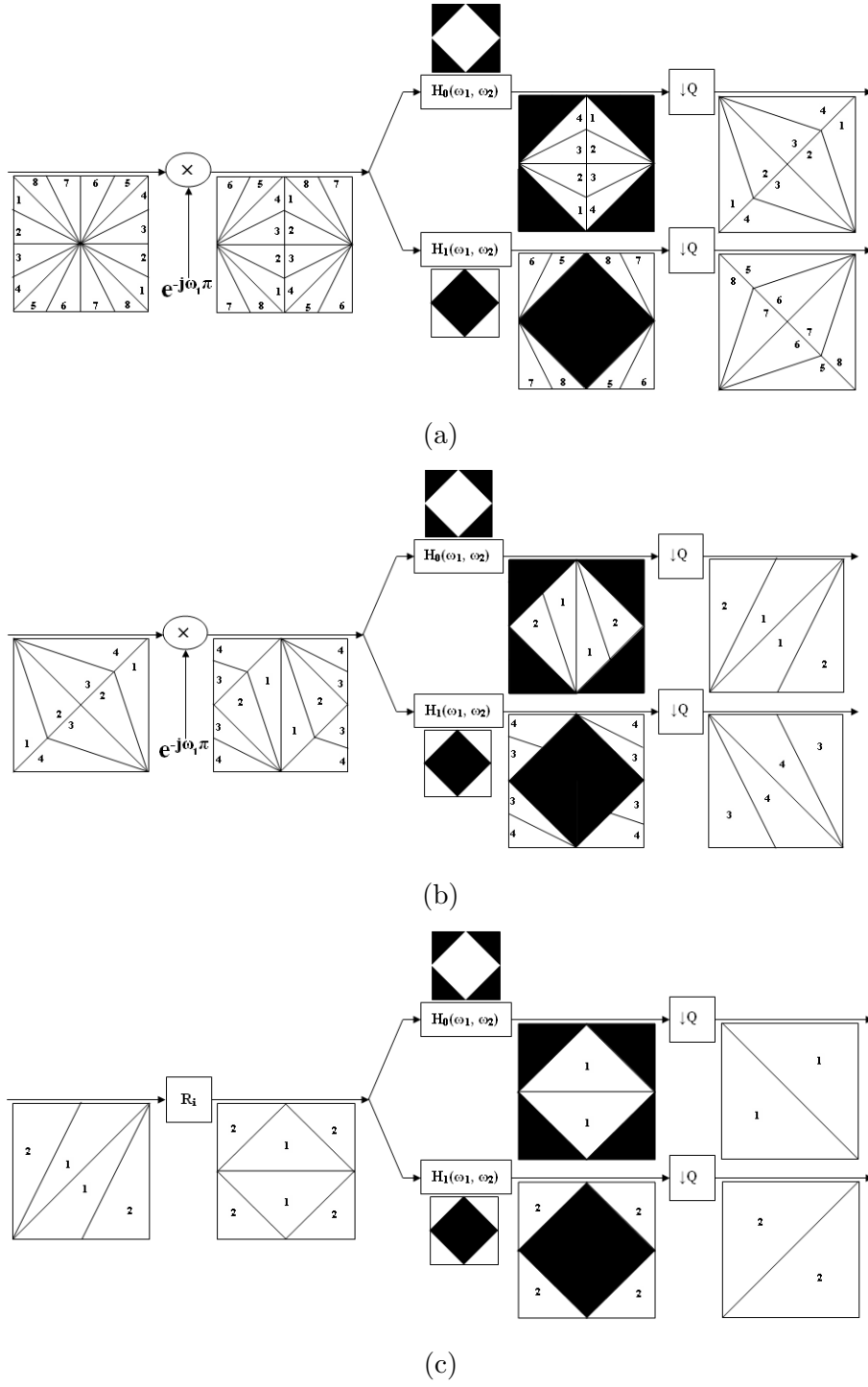


Figure 2-3: The DFB structure in [99]. a) First stage, b) Second stage, and c) Third stage. Subbands produced by the first stage are used as input to the second stage and so on.

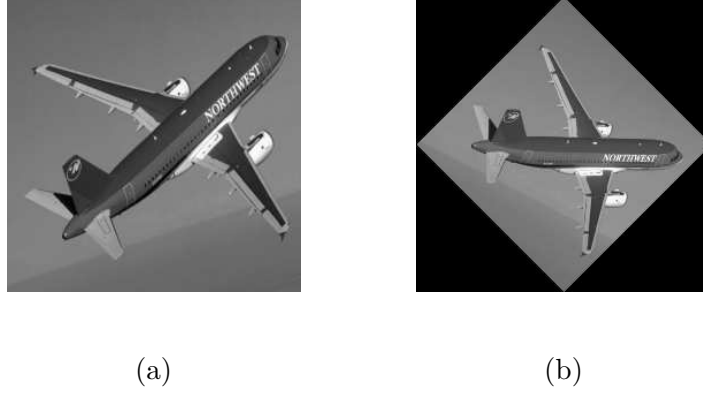


Figure 2-4: Downsampling and rotation effects of Quincunx matrix  $Q$ . a) Original airplane image and b) after Quincunx downsampling.

#### 2.4.1 First stage of DFB

Construction of the first stage of DFB requires a pair of diamond-shaped like passband filters,  $H_0(\omega_1, \omega_2)$  and  $H_1(\omega_1, \omega_2)$ , a modulator, and Quincunx downsampling matrix as shown in Figure 2-3(a), where  $\varpi = (\omega_1, \omega_2)^T$  is a pair of 2D Fourier frequency variables. Modulator used in this stage shifts frequency spectrum of an input image by  $\pi$  in any of the two directions. In this structure,  $Q$  is a Quincunx non-separable downsampling  $2 \times 2$  matrix which not only downsamples but also rotates the image at an angle of  $45^\circ$ ; see Figure 2-4. Mathematically in the spatial domain it is represented as

$$z_d[\mathbf{m}] = z[Q\mathbf{m}], \quad (2.21)$$

where  $\mathbf{m} \in \mathbb{N}^2$  denotes the set of all integer pairs,  $z[\mathbf{m}]$  a 2D discrete signal,  $z_d$  the Quincunx downsampled version of  $z$ , and  $Q = \begin{bmatrix} 1 & 1 \\ -1 & 1 \end{bmatrix}$ .

### 2.4.2 Second stage of DFB

Requirements for construction of the second stage of DFB are same as those for the first one. Subbands produced by the first stage are used as input to the second stage. Figure 2-3(b) shows the spectral geometry of subbands created by the second stage. It is evident that these subbands have parallelogram-shaped geometry.

### 2.4.3 Third stage of DFB

The additional requirements for construction of the third stage (see Figure 2-3(c)) as compare to the first and second are resampling and post-sampling matrices. Resampling matrices  $R_i$  are used to map parallelogram-shaped passbands to diamond-shaped passbands. Four different resampling matrices are applied in third stage which are

$$R_1 = \begin{bmatrix} 1 & 1 \\ 0 & 1 \end{bmatrix} \quad R_2 = \begin{bmatrix} 1 & -1 \\ 0 & 1 \end{bmatrix}$$

$$R_3 = \begin{bmatrix} 1 & 0 \\ 1 & 1 \end{bmatrix} \quad R_4 = \begin{bmatrix} 1 & 0 \\ -1 & 1 \end{bmatrix}.$$

Post-sampling matrices  $B_i$  are used to convert the overall non-diagonal sampling matrix to the diagonal one. Up till the second stage the overall downsampling matrix remains diagonal, due to which subbands are visually correct. But in the third stage or onward, the overall downsampling matrix becomes non-diagonal resulting in visually distorted subbands. By applying  $B_i$ , the visual distortion created by non-diagonalization of overall sampling matrix is removed, making the subbands visually correct. Note that due to the presence of downsampling matrices, the subbands are smaller in size as compare to the input image.

Figure 2-5 shows eight directional subbands of the airplane image in Figure 2-4 (a) obtained using DFB. Each subband correspond to a unique angular orientation.

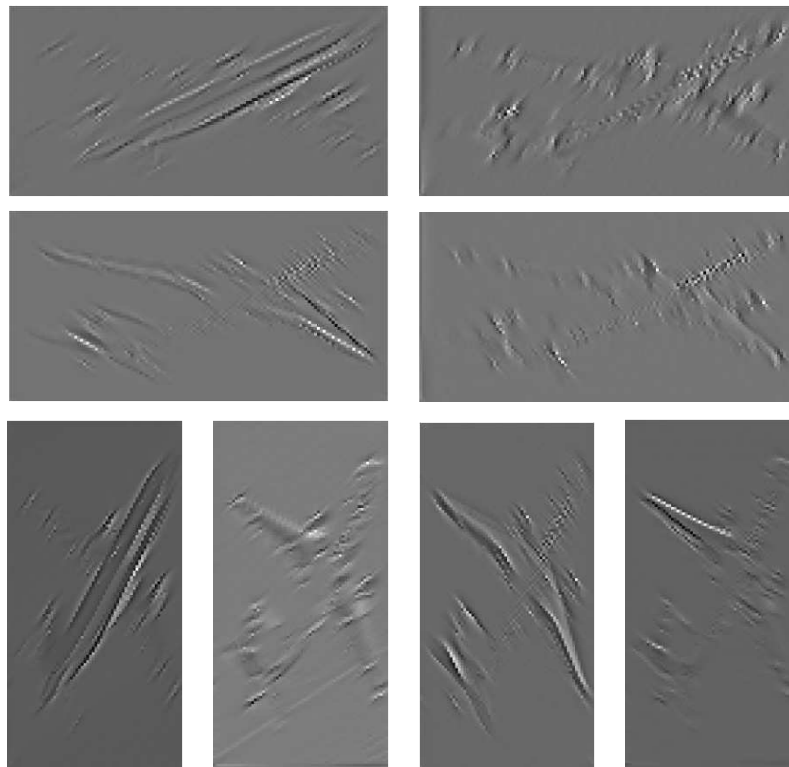


Figure 2-5: Eight directional subbands of the airplane image in Figure 2-4 (a) decomposed using DFB.

## 2.5 Active Contours

Another less local method to handle edge curve as mentioned in the previous section is active contours (ACs). First introduced by Kass et al. [57] in 1988, ACs (a.k.a. snakes or deformable curves) has attracted much attention in image segmentation research community. The underlying idea is that an initial contour is first specified and then pulled by image-dependent forces towards the edges of the objects of interest. To date, there are two main types of ACs in the literature: parametric and geometric ACs, the complete review of which is beyond the scope of this thesis. Instead, only some representative works of each type will be introduced in the following subsections after necessary and basic concepts are provided.

### 2.5.1 Basic concepts

#### Curve evolution

Consider a family of closed planar curves deforming in time  $C(p, t) = [x(p, t), y(p, t)]$  where  $t$  denotes time and  $p$  ( $0 \leq p \leq 1$ ) parameterizes the curve. Suppose that this family of curve moves under a general velocity field  $\vec{\mathcal{V}}$

$$\begin{cases} \frac{\partial C(p, t)}{\partial t} = \vec{\mathcal{V}} = \mathcal{V}_{\parallel}(p, t)\vec{\mathcal{T}}(p, t) + \mathcal{V}_{\perp}(p, t)\vec{\mathcal{N}}(p, t) \\ C(p, 0) = C_0(p) \end{cases} \quad (2.22)$$

where  $\vec{\mathcal{T}}$  and  $\vec{\mathcal{N}}$  are respectively the unit Euclidean tangent and the (inward) unit Euclidean normal and  $\mathcal{V}_{\parallel} = \vec{\mathcal{V}} \cdot \vec{\mathcal{T}}$  and  $\mathcal{V}_{\perp} = \vec{\mathcal{V}} \cdot \vec{\mathcal{N}}$  the tangent and normal components of  $\vec{\mathcal{V}}$ , respectively.

We are interested in the geometry of the curve, denoted by  $\text{Geo}[C(p, t)]$ . Parameterizing the curve  $C$  with another parameter  $q = q(p, t)$ ,  $\partial_p q > 0$ , we have

$$\text{Geo}[C(p, t)] = \text{Geo}[C(q, t)]. \quad (2.23)$$

Epstein and Gage proved in [39] via the following lemma, that under certain conditions, the tangential velocity does not affect the geometry of the deformation.

**Lemma 2.1.** *If  $\mathcal{V}_\perp$  is a geometric intrinsic of the curve, i.e., a function does not depend on the parameterization, then the geometry of  $C(p, t)$  satisfying (2.22) is identical to that of the family of curve  $C(q, t)$  satisfying*

$$\frac{\partial C(q, t)}{\partial t} = \mathcal{V}_\perp(q, t)\vec{\mathcal{N}}(q, t) \quad (2.24)$$

*In other words, the geometry of the deformation is only affected by the normal velocity. The tangential velocity influences the parameterization only, not the geometry.*

*Proof.* See [39]. □

The job of curve evolution is then to design the function  $\mathcal{V}_\perp$  that solves the problem at hand. One of the most studied such function is  $\mathcal{V}_\perp = \kappa$ , where  $\kappa$  is the Euclidean curvature defined by  $\partial_{ss}C = \kappa\vec{\mathcal{N}}$  with  $s$  the Euclidean arc-length which is a particular parameterization satisfying  $|\partial_s C| = 1$ . Then the evolution equation (2.24) reads

$$\partial_t C = \kappa\vec{\mathcal{N}} = \partial_{ss}C. \quad (2.25)$$

This equation is called the *mean curvature motion* (MCM) [42, 4] or the *Euclidean shortening flow* as it is obtained from the minimization of the length energy

$$E(C) = \oint |\partial_s C| ds = \int_C ds. \quad (2.26)$$

As a result, it shrinks the Euclidean perimeter while evolving. It is also called the *geometric heat flow* due to its very similar form with the linear heat equation in (2.3). Note that the MCM flow is however nonlinear since arc-length  $s$  is a time-dependent function. This interesting characteristic makes the flow very well studied in the literature.

**Level-set framework**

Apart from explicit representation using its parameterization, a curve can be implicitly represented by a level set of a function  $\phi(\mathbf{x}, t) : \mathbb{R}^2 \times [0, T) \rightarrow \mathbb{R}$  such that

$$C = \{\mathbf{x} \in \mathbb{R}^2 : \phi(\mathbf{x}, t) = c\} \quad (2.27)$$

where  $c$  is a real constant. The curve, as above, is moving under the influence of a normal velocity

$$\frac{\partial C}{\partial t} = \nu_{\perp} \vec{\mathcal{N}}. \quad (2.28)$$

We now have to find the evolution of  $\phi$  such that its level set moves in the same manner as  $C$  does. Differentiating (2.27) with respect to  $t$ , we obtain

$$\frac{\partial \phi}{\partial t} + \nabla \phi \cdot \frac{\partial C}{\partial t} = 0. \quad (2.29)$$

and combining with (2.28), we get

$$\frac{\partial \phi}{\partial t} + \nabla \phi \cdot \nu_{\perp} \vec{\mathcal{N}} = 0. \quad (2.30)$$

Recalling that the unit inward normal is given by  $\vec{\mathcal{N}} = -\frac{\nabla \phi}{|\nabla \phi|}$  ( $\phi$  is assumed to be positive outside the curve and negative inside), we end up with

$$\frac{\partial \phi}{\partial t} = \nu_{\perp} |\nabla \phi|. \quad (2.31)$$

Note that the level-set value  $c$  vanishes after the derivative is taken, meaning that all the level sets move under the same flow, independently to  $c$ . So, without loss of generality, the zero level set is usually chosen to represent for the curve. When a function evolves according to (2.31), all of its level sets obey the flow in (2.28). The evolution is performed using only geometric measures, making itself independent of the curve's parameterizations.

The MCM (2.25) can be rewritten in the level-set framework as

$$\frac{\partial \phi}{\partial t} = \kappa |\nabla \phi| \quad \kappa = \operatorname{div} \frac{\nabla \phi}{|\nabla \phi|}. \quad (2.32)$$

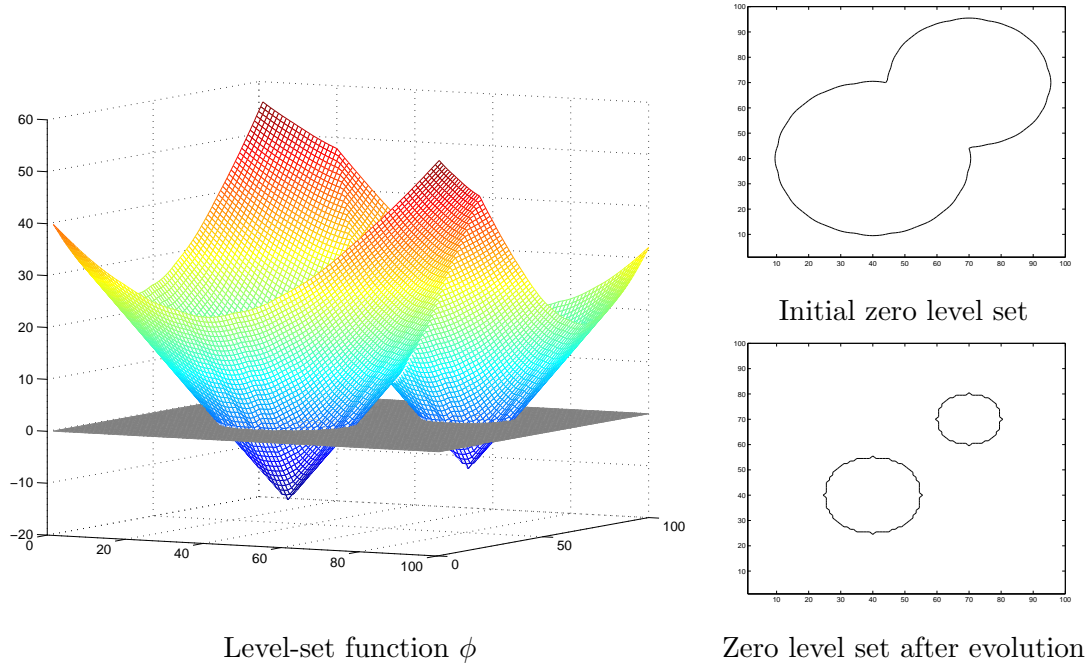


Figure 2-6: Natural topological change handling of the level-set method.

One major advantage of the level-set method is that it can naturally handle topology changes. The function  $\phi$  moves up and down on a fixed coordinate system without changing its topology as long as  $\mathcal{V}_\perp$  is smooth. However, the level set corresponding to the curve may split or merge as  $\phi$  evolves; see Figure 2-6. More details about this method can be found in [91, 116, 89].

### Mumford-Shah functional

One way to segment an image is to construct its simplified version that consists of homogeneous regions separated by sharp edges. In a variational framework, the idea can be formulated as: starting from an image  $I(\mathbf{x})$ , one looks for a pair  $(f, \Gamma)$  such that  $f$  is a piecewise smooth version of  $I$  and  $\Gamma$  is the set of edges. This was introduced by Mumford

and Shah [84] via the energy functional

$$E(f, \Gamma) = \int_{\Omega} (f - I)^2 d\mathbf{x} + \lambda \int_{\Omega - \Gamma} |\nabla f|^2 d\mathbf{x} + \nu \int_{\Gamma} ds \quad (2.33)$$

where  $\Omega \in \mathbb{R}^N$  is the image plane and  $\lambda$  and  $\nu$  are positive weighting constants. In this functional, the first and second terms ensures  $f$  is close to  $I$  and varies slowly inside separated regions whereas the last term makes the boundary  $\Gamma$  as short as possible to guarantee its smoothness. The Mumford-Shah functional provides a very general formulation, in the form of an optimization problem for image segmentation. However, studying this energy is not trivial since it involves two unknowns  $f$  and  $\Gamma$  of different natures:  $f$  is a function defined on an  $N$ -dimensional space whereas  $\Gamma$  is an  $(N - 1)$ -dimensional set.

An simplified version of the Mumford-Shah functional, which is called the *cartoon limit* and obtained when  $\lambda = 0$ , is used to provide a piecewise constant approximation of  $I$

$$E(f, \Gamma) = \int_{\Omega} (f - I)^2 d\mathbf{x} + \nu \int_{\Gamma} ds. \quad (2.34)$$

In this case,  $f$  is equal to the mean values of  $I$  on the connected components of  $\Omega - \Gamma$  and thus  $E$  becomes a function of only  $\Gamma$ . A large amount of work has been devoted to this special case [84, 79, 80, 75].

### 2.5.2 Traditional AC

The traditional snake introduced by Kass et al. [57] is a parameterized curve  $C(p) = [x(p), y(p)]$ ,  $p \in [0, 1]$  that moves through the image to seek a minimum state of the energy functional

$$E(C) = \int_0^1 \left( \frac{\alpha}{2} |C'(p)|^2 + \frac{\beta}{2} |C''(p)|^2 + E_{ext}(C(p)) \right) dp \quad (2.35)$$

where  $\alpha > 0$  and  $\beta > 0$  are weighting parameters that respectively control the elasticity and rigidity of the curve,  $C'(p) = \frac{\partial C}{\partial p}$ ,  $C''(p) = \frac{\partial^2 C}{\partial p^2}$ , and  $E_{ext}$  an external energy. In this functional, the first two terms define a internal energy that serves to control the smoothness

of the curve whereas the external energy is responsible for attracting the curve towards the image features of interest (object's boundaries). Using the calculus of variation and the gradient descent, one can derive the evolution flow for the above snake as

$$\partial_t C(p, t) = \alpha C''(p, t) - \beta C''''(p, t) - \nabla E_{ext}. \quad (2.36)$$

For example, in edge detection,  $E_{ext}$  can be defined as

$$E_{ext}(C(p)) = -\lambda |\nabla I(C(p))| \quad \lambda > 0. \quad (2.37)$$

Then, the snake will evolve according to (2.36) to search in a class of smooth curves for a curve  $C^*(p)$  for which  $|\nabla I(C^*(p))|$  is maximal. This is also a way to regularize the edge detection problem.

### 2.5.3 Gradient Vector Flow AC

Since the traditional snake is driven by the gradient of the image, it suffers from two main problems. The first one is limited *capture range*, i.e., the initial contour should be close to the true boundary to guarantee correct convergence. This is due to the fact that gradient has significant magnitude only within a vicinity of an edge and is zero outside. The second problem is the inability to move into *boundary concavities* [34, 1]; see Figure 2-7. Cohen and Cohen [28] proposed a balloon force to increase the capture range but it still could not solve the latter issue. On the other hand, pressure forces [27] can solve the boundary concavity problem but create two new difficulties: in choosing appropriate value and direction of the forces.

In [139], Xu and Prince proposed a new AC model that satisfactorily solved both problems and thus became a state-of-the-art model of this kind. The authors replaced the potential force  $-\nabla E_{ext}$  in (2.36) with a novel external force field called *gradient vector flow* (GVF). In order to build up this field, an appropriate edge map function  $f(x, y)$

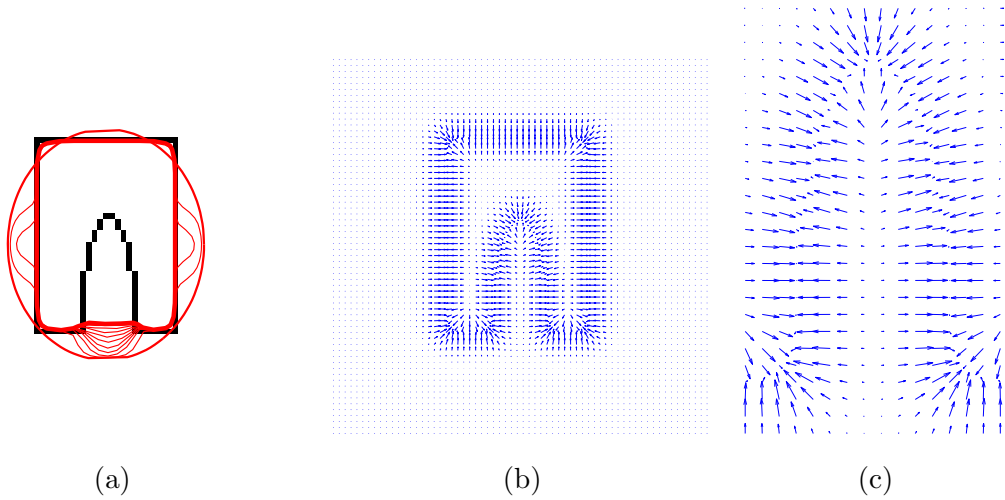


Figure 2-7: (a) Evolution of a traditional snake, (b) gradient of the image, and (c) its zoomed-in area. The initial curve must be within the capture range of the potential force (the gradient, in this case). The curve cannot evolve into the boundary concavity because the forces point horizontally in opposite directions.

having larger values near the image edges is first chosen. To this end, an image gradient function is usually considered for its simplicity:

$$f(x, y) = |\nabla I_\sigma(x, y)|^2. \quad (2.38)$$

The GVF is then defined as a two-dimensional vector field  $[u(x, y), v(x, y)]$  that minimizes the following energy functional

$$\varepsilon(u, v) = \int_{\Omega} \mu(|\nabla u|^2 + |\nabla v|^2) + |\nabla f|^2 |[u, v] - \nabla f|^2 \, dx \, dy \quad (2.39)$$

where  $\Omega \subset \mathbb{R}^2$  is the image plane and  $\mu$  a noise-control parameter. This functional keeps the GVF field nearly same as the gradient of the edge map,  $\nabla f$ , in the neighborhood of the boundaries, where  $|\nabla f|$  is large. At the same time, the field still has significant values in the homogeneous regions, where  $|\nabla f|$  gets close to 0, via a diffusion process. One can optimize  $[u(x, y), v(x, y)]$  using the gradient descent method and the calculus of variations

$$\partial_t u = \mu \Delta u - (u - \partial_x f) |\nabla f|^2 \quad \partial_t v = \mu \Delta v - (v - \partial_y f) |\nabla f|^2. \quad (2.40)$$

The GVF AC was proposed for boundary extraction in the following way:

$$\partial_t C(p) = \alpha C''(p) - \beta C''''(p) + [\hat{u}, \hat{v}] \quad (2.41)$$

where  $[\hat{u} = u/\sqrt{u^2 + v^2}, \hat{v} = v/\sqrt{u^2 + v^2}]$  is the normalized GVF (NGVF) served as the external force pulling the curve towards object boundaries. This model has an increased capture range and can deal with concave regions; see Figure 2-8.

#### 2.5.4 (Original) Geometric AC

The AC models discussed so far are of parametric type since the energy depends on the parameterizations of the curve yet not on the objects' geometry, i.e., they are non-intrinsic. Also, they cannot handle topological changes to simultaneously detect multiple objects. Many special (usually heuristic) procedures have been proposed in detecting

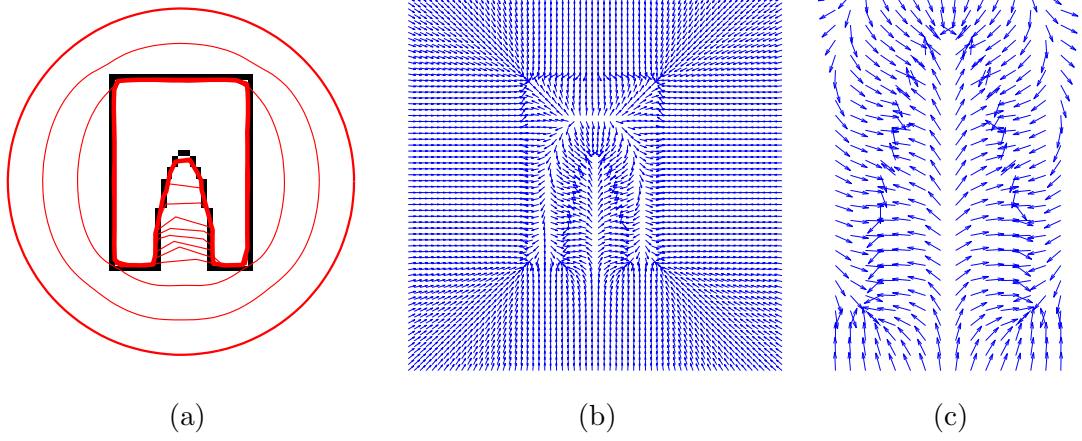


Figure 2-8: (a) Evolution of the GVF AC, (b) the external GVF force, and (c) its zoomed-in area. The GVF force has a much larger the capture range compared to the traditional force and it points upward into the concavity region, which helps the snake correctly converge.

possible splitting and merging [65, 123, 77] but prior knowledge about the number of objects needs to be given.

A novel model called the *Geometric AC*, proposed independently by Caselles et al. [20] and by Malladi et al. [74], can handle topology changes without any additional task. The model is based on the MCM and the level-set framework where the curve  $C$  is represented by the zero level set of a Lipschitz function  $\phi : \Omega \rightarrow \mathbb{R}$  which is usually defined as a signed distance function such that

$$\begin{cases} C &= \{\mathbf{x} \in \Omega : \phi(\mathbf{x}) = 0\}, \\ \text{inside}(C) &= \{\mathbf{x} \in \Omega : \phi(\mathbf{x}) < 0\}, \\ \text{outside}(C) &= \{\mathbf{x} \in \Omega : \phi(\mathbf{x}) > 0\}. \end{cases} \quad (2.42)$$

The Geometric AC evolution flow is given by

$$\partial_t \phi = g \cdot (\kappa + V_0) \cdot |\nabla \phi| \quad (2.43)$$

where  $V_0$  is a real constant and  $g = g(\mathbf{x})$  an edge-based function which approaches 0 on the edges and 1 in other regions, e.g.,  $g(\mathbf{x}) = e^{-\frac{1}{\sigma_e^2} |\nabla I_\sigma(\mathbf{x})|^2}$  with  $\sigma_e$  a scaling factor. In this flow, the curvature  $\kappa$ -based flow has the properties of smoothing the curve, while  $V_0$  shrinks or expands the contour along its normal direction at a constant velocity. The product  $g \cdot (\kappa + V_0)$  determines the overall evolution speed of level sets of  $\phi(\mathbf{x}, t)$ . At the same time, the main use of  $g$  has the effect of stopping the curve when it reaches to the object boundaries.

### 2.5.5 Geodesic AC

The Geometric AC overcomes the limitation of the traditional snakes in capturing multiple objects without prior knowledge of their exact number and without using special topological change detecting procedures. This model is motivated by not an energy minimization but a curve evolution method where the convergence of the curve depends on an edge function  $g(\mathbf{x})$ . This works well in general for objects that have good contrast. However, if there are weak edges and/or gaps along edges, the evolving curve tends to pass through these areas because gradient values are not large enough for  $g(\mathbf{x})$  to approach 0.

Another geometric-type snake was introduced in [21, 142] using an energy to search for a curve of minimal weighted length (geodesic curve). The so-called *Geodesic AC* model was proven to be a special case of the traditional snake. Considering the traditional snake energy (2.35) with  $\beta = 0$ , one have

$$E(C) = \int_0^1 \left( \frac{\alpha}{2} |C'(p)|^2 - \lambda |\nabla I(C(p))| \right) dp. \quad (2.44)$$

This can be generalized by replacing the edge detector  $-|\nabla I|$  with a strictly decreasing function  $g(|\nabla I|^2)$ , leading to

$$E(C) = \int_0^1 \left( \frac{\alpha}{2} |C'(p)|^2 + \lambda g(|\nabla I(C(p))|^2) \right) dp. \quad (2.45)$$

Using Maupertuis' principle of least action, minimizing  $E(C)$  in (2.45) is equivalent to minimizing the weighted length [21]

$$L_R = \int_0^1 g(|\nabla I(C(p))|) |C'(p)| dp = \int_C g(|\nabla I(C(s))|) ds. \quad (2.46)$$

We observe that this length is obtained by weighting the Euclidean length element  $ds$  in classical length definition (2.26) with  $g(|\nabla I(C(s))|)$ , which characterizes the object's boundary. This means that in order to detect the object, one can search for the path of minimal edge-weighted length  $L_R$ , leading to the Geodesic AC flow (via the gradient descent method)

$$\partial_t C = g\kappa \vec{\mathcal{N}} - (\nabla g \cdot \vec{\mathcal{N}}) \vec{\mathcal{N}}. \quad (2.47)$$

The level-set implementation of this flow is given by

$$\partial_t \phi = g\kappa |\nabla \phi| + \nabla g \cdot \nabla \phi. \quad (2.48)$$

In a more general case, one may wish to add a constant velocity  $V_0$  (which is equivalent to adding an area constraint to the energy), for example to increase the convergence speed, obtaining

$$\partial_t \phi = g \cdot (\kappa + V_0) \cdot |\nabla \phi| + \nabla g \cdot \nabla \phi. \quad (2.49)$$

Comparing this with the Geometric AC (2.43), we see that the extra stopping term  $(\nabla g \cdot \nabla \phi)$  is used to increase the attraction of the evolving contour towards an edge, of special help when the edge has different gradient values and/or gaps along it.

### 2.5.6 GVF-Geometric AC

Inspired from the observations that the GVF consists of the optimal direction to be followed to reach the object boundaries and that evolving the contour in the direction of its normal is a main characteristic of the geometric active contours, Paragios et al. [93] proposed an integration of GVF into the Geometric AC as

$$\partial_t C = g \left( \kappa + V_0 K(\mathbf{x}) + (1 - |K(\mathbf{x})|) [\hat{u}, \hat{v}] \cdot \vec{\mathcal{N}} \right) \vec{\mathcal{N}} \quad (2.50)$$

or in its equivalent level-set formulation

$$\partial_t \phi = g \left\{ (\kappa + V_0 K(\mathbf{x})) |\nabla \phi| - (1 - |K(\mathbf{x})|) [\hat{u}, \hat{v}] \cdot \nabla \phi \right\} \quad (2.51)$$

where  $[\hat{u}, \hat{v}]$  is the normalized GVF and  $K(\mathbf{x}) = \text{sign}([\hat{u}, \hat{v}] \cdot \vec{\mathcal{N}}) e^{-\delta |[\hat{u}, \hat{v}] \cdot \vec{\mathcal{N}}|}$  with  $\delta$  a scaling factor.  $K(\mathbf{x})$  approaches 1 when the normal vector  $\vec{\mathcal{N}}$  and the GVF  $[\hat{u}, \hat{v}]$  are close to orthogonal and 0 otherwise.

In the above flow,  $(1 - |K(\mathbf{x})|) [\hat{u}, \hat{v}]$  has the effect of a bidirectional flow that moves the curve towards object boundaries from either sides whereas  $V_0 K(\mathbf{x})$  serves as an adaptive balloon force used to determine the evolution when the bidirectional flow term becomes inactive. Similar to that of the Geometric AC, the overall speed of this curve evolution is coupled with the edge-driven information via the stopping term  $g$ .

### 2.5.7 Chan-Vese AC

Chan and Vese [24] proposed an alternative form of AC based on the Mumford and Shah functional for segmentation [84]. Unlike other level set-based ACs which rely much on the gradient of the image as the stopping term and thus have unsatisfactory performance in noisy images, the CV AC model utilizes instead the homogeneity characteristic of an object. In this case, the image  $I$  is assumed to be consisted of two areas with approximately piecewise-constant intensities, of different value  $c_{in}$  and  $c_{out}$ . The “fitting” term is defined as

$$F(C) = F_1(C) + F_2(C) = \int_{inside(C)} |I(\mathbf{x}) - c_1|^2 d\mathbf{x} + \int_{outside(C)} |I(\mathbf{x}) - c_2|^2 d\mathbf{x} \quad (2.52)$$

where  $c_1$  and  $c_2$  are respectively the average intensities inside and outside the variable curve  $C$ . As can be seen in Figure 2-9, the “fitting” term is minimized if the curve  $C$  is placed exactly on the boundary of the two areas.

One can regularize the solution by constraining the length of the curve and the area

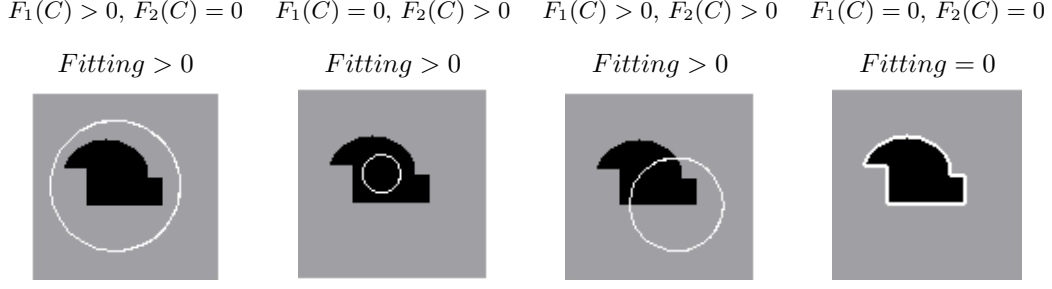


Figure 2-9: All possible positions of the curve. When it is on the boundary of the object, the “fitting” term is minimized.

inside it, leading to the energy

$$E(C) = \nu \text{Length}(C) + V_0 \text{Area}(\text{inside}(C)) + F(C) \quad (2.53)$$

where  $\nu$  and  $V_0$  are constants. For the level-set formulation, the Heaviside function  $H(\cdot)$  is used

$$H(u) = \begin{cases} 1, & \text{if } u \geq 0 \\ 0, & \text{if } u < 0. \end{cases} \quad (2.54)$$

The energy then reads

$$E(C) = \nu \int_{\Omega} |\nabla H(\phi(\mathbf{x}))| d\mathbf{x} + V_0 \int_{\Omega} H(-\phi(\mathbf{x})) d\mathbf{x} + \int_{\Omega} |I(\mathbf{x}) - c_1|^2 H(-\phi(\mathbf{x})) d\mathbf{x} + \int_{\Omega} |I(\mathbf{x}) - c_2|^2 H(\phi(\mathbf{x})) d\mathbf{x}. \quad (2.55)$$

The solution for minimizing this energy is obtained [24] by gradient descent method as

$$\partial_t \phi = |\nabla \phi| [\nu \kappa + V_0 + (I - c_1)^2 - (I - c_2)^2]. \quad (2.56)$$

This flow evolves the curve, looking for a two-phase segmentation of the image, given by  $\hat{I}(\mathbf{x}) = c_{in} H[\phi(\mathbf{x})] + c_{out}(1 - H[\phi(\mathbf{x})])$ .

For multiphase cases [129], we can write illustratively the formulations for four phases

or classes (and therefore using the two level-set functions  $\phi_1$  and  $\phi_2$ ) as

$$\begin{aligned}\frac{\partial \phi_1}{\partial t} &= |\nabla \phi_1| \left\{ \nu_1 \kappa_1 - V_{01} - [(u_0 - c_{11})^2 - (u_0 - c_{01})^2] H(\phi_2) \right. \\ &\quad \left. - [(u_0 - c_{10})^2 - (u_0 - c_{00})^2] (1 - H(\phi_2)) \right\} \\ \frac{\partial \phi_2}{\partial t} &= |\nabla \phi_2| \left\{ \nu_2 \kappa_2 - V_{02} - [(u_0 - c_{11})^2 - (u_0 - c_{10})^2] H(\phi_1) \right. \\ &\quad \left. - [(u_0 - c_{01})^2 - (u_0 - c_{00})^2] (1 - H(\phi_1)) \right\}\end{aligned}$$

where  $\nu_i$  and  $V_{0i}$  are constants,  $\kappa_i = \operatorname{div} \left( \frac{\nabla \phi_i}{|\nabla \phi_i|} \right)$ ,  $i = \{1, 2\}$ , and

$$c_{11}(\phi) = \text{average}(u_0) \text{ in } \{\mathbf{x} : \phi_1(\mathbf{x}) > 0, \phi_2(\mathbf{x}) > 0\},$$

$$c_{10}(\phi) = \text{average}(u_0) \text{ in } \{\mathbf{x} : \phi_1(\mathbf{x}) > 0, \phi_2(\mathbf{x}) < 0\},$$

$$c_{01}(\phi) = \text{average}(u_0) \text{ in } \{\mathbf{x} : \phi_1(\mathbf{x}) < 0, \phi_2(\mathbf{x}) > 0\},$$

$$c_{00}(\phi) = \text{average}(u_0) \text{ in } \{\mathbf{x} : \phi_1(\mathbf{x}) < 0, \phi_2(\mathbf{x}) < 0\}.$$

## 2.6 Relation between Diffusion Filters and Active Contours

The Geodesic AC flow in (2.48) can be rewritten as

$$\partial_t \phi = |\nabla \phi| \operatorname{div} \left( g(I) \frac{\nabla \phi}{|\nabla \phi|} \right) \quad (2.57)$$

where  $g$  is the edge function. This equation deals with two functions: the level-set function  $\phi$  and the image  $I$ . Consider a special case when  $\phi = I$ , meaning that the auxiliary level-set function is selected as the image itself. Then, one obtains

$$\partial_t I = |\nabla I| \operatorname{div} \left( g(I) \frac{\nabla I}{|\nabla I|} \right). \quad (2.58)$$

A straightforward interpretation of (2.58) is that each of the level sets of the image moves under the geodesic flow, searching for its minimal edge-weighted length, leading to a smoother image. This flow is thus called self-snakes. The smoothing effect of the flow can be made clearer by rewriting it as

$$\partial_t I = \mathcal{F}_{\text{diffusion}} + \mathcal{F}_{\text{shock}} \quad (2.59)$$

where

$$\mathcal{F}_{\text{diffusion}} = g(I)|\nabla I|\operatorname{div}\left(\frac{\nabla I}{|\nabla I|}\right), \quad (2.60)$$

$$\mathcal{F}_{\text{shock}} = \nabla g(I) \cdot \nabla I. \quad (2.61)$$

Expanding  $\mathcal{F}_{\text{diffusion}}$ , one has

$$\mathcal{F}_{\text{diffusion}} = g(I) \frac{\partial_{xx}I(\partial_y I)^2 - 2\partial_x I \partial_y I \partial_{xy}I + \partial_{yy}I(\partial_x I)^2}{(\partial_x I)^2 + (\partial_y I)^2}. \quad (2.62)$$

On the other hand, denoting  $\xi$  as the direction perpendicular to the gradient  $\nabla I$ , that is,  $\xi = \frac{[-\partial_y I, \partial_x I]}{\sqrt{(\partial_x I)^2 + (\partial_y I)^2}}$ , and calculating the second-order directional derivative of  $I$  in the direction of  $\xi$ , one obtains

$$\partial_{\xi\xi}I = \frac{\partial_{xx}I(\partial_y I)^2 - 2\partial_x I \partial_y I \partial_{xy}I + \partial_{yy}I(\partial_x I)^2}{(\partial_x I)^2 + (\partial_y I)^2}. \quad (2.63)$$

This means that

$$\mathcal{F}_{\text{diffusion}} = g(I)\partial_{\xi\xi}I \quad (2.64)$$

and that the term  $\mathcal{F}_{\text{diffusion}}$  diffuses the image in the direction of  $\xi$  (perpendicular to  $\nabla I$ , or parallel to edges) with the amount determined by  $g(I)$  which can be chosen as in the snakes model.

The other term,  $\nabla g \cdot \nabla I$ , looks very much like a shock filter for image deblurring [90]. Therefore, the self-snakes flow (2.58) acts as a combination of anisotropic diffusion and shock filtering, leading to the dual effects: smoothing along edges and enhancing across them. Figure 2-10 shows an example of self-snakes flow applied on a retinal image.

Now, if one divides  $\nabla I$  from the self-snakes flow and selects a function  $\hat{g}(I)$  satisfying  $\hat{g}(I) = \frac{g(I)}{|\nabla I|}$ , the flow comes down to the Perona-Malik model

$$\partial_t I = \operatorname{div}(\hat{g}(I)\nabla I). \quad (2.65)$$

This relation is interesting since it by somehow shows the intrinsic connection between the Geodesic AC and the Perona-Malik flow, two of the most influential works in the field.

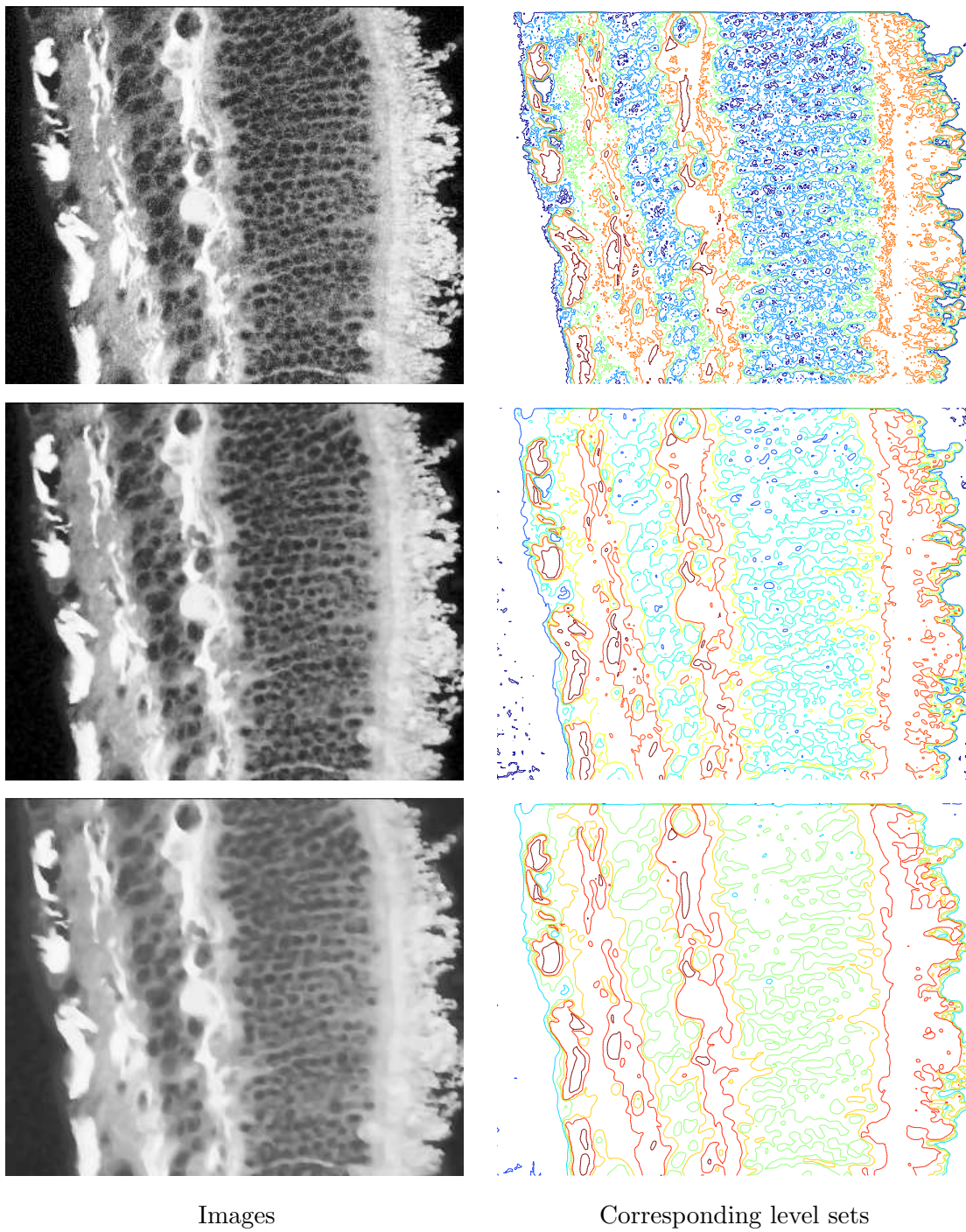


Figure 2-10: De-noising a retinal image with self-snakes. Top to bottom: original image and its de-noised versions after 10 iterations and 30 iterations, respectively. Note how edges are preserved.

## 2.7 Summary

This chapter has presented a number of variational models for image processing in general and enhancement and segmentation in particular. As we have seen, one of the simplest and earliest variational models for enhancement is linear diffusion filter which was proven to be equivalent to classical Gaussian filtering. And then, since Perona-Malik model of nonlinear diffusion was introduced, a large amount of research has been devoted to the understanding of mathematical properties of this and related variational formulations [6, 22, 143] and its relations with other image processing techniques [113, 117, 146], to its modification for fast and precise implementations or for specific applications [49], to the development of more stable functions [5, 22, 86, 143], and to the introduction of directional diffusivity, leading to the anisotropic diffusion flow of Weickert. To support the directional estimation in anisotropic diffusion, many operators have been introduced, including structure tensor, Hessian tensor, and directional filter bank.

In segmentation community, the snakes model of Kass et al. has opened up a very interesting research direction. Many snakes models have been proposed such as the GVF AC, the Geometric AC, the Geodesic AC, the GVF-Geometric AC, the Chan-Vese AC, to name a few. They can be classified based on how the contour is represented, leading to the parametric and geometric types, or how the flow is derived, leading to the energy-based or the curve evolution-based types. The field is still busy; more and more snakes models continue to be introduced yearly and even monthly (see e.g., [108, 51, 138, 122, 121, 78, 67] and the references therein).

Moreover, the Geodesic AC, one of the most influential works, was shown to be intrinsically connected to the Perona-Malik model for enhancement. This amazing relation reinforces the fact that variational methods play a more and more important role as a modern technique in image processing. A rough taxonomy of variational methods is given in Figure 2-11, where the knowledge-incorporated enhancement and segmentation are the

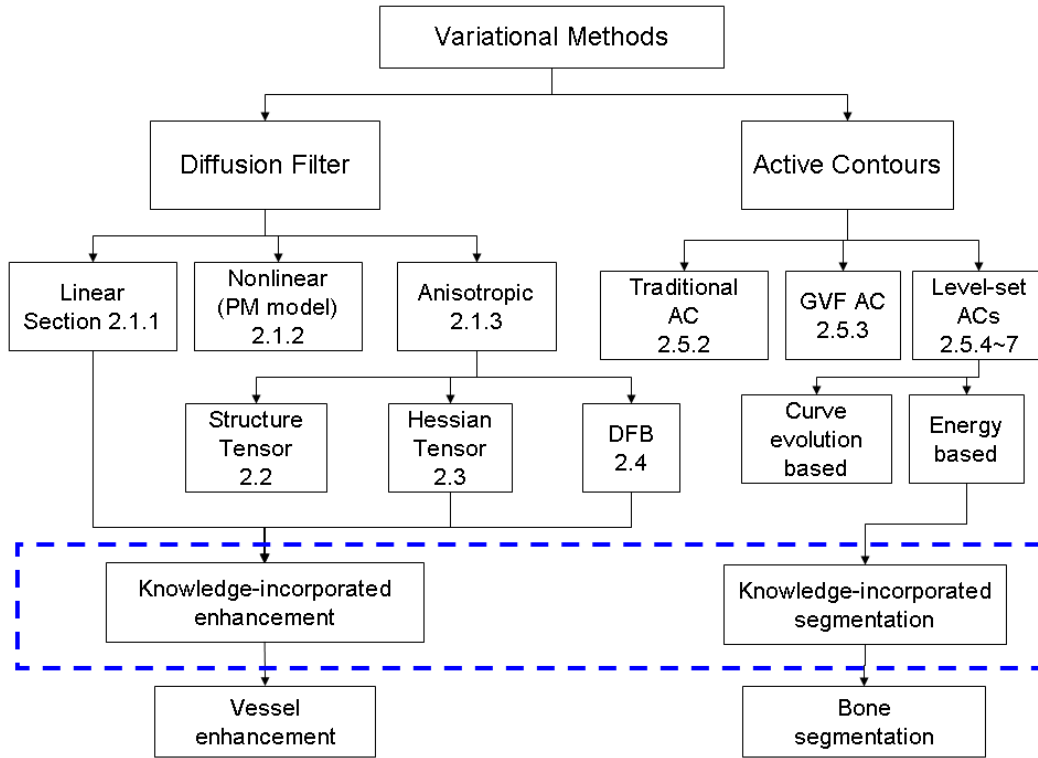


Figure 2-11: Taxonomy of variational methods in image processing.

two proposed models that will be described in the next two chapters. As applications, the proposed models are applied to vessel enhancement and bone segmentation in medical imagery, respectively.

## Chapter 3

# Curvilinear Structure Enhancement

Image enhancement refers to sharpening certain features of interest of an image, based upon which other visual decisions made afterwards are more correctly and robustly. The features can be image contrast, boundaries, edges, or lines. Here, I would like to differentiate enhancement of image contrast from that of object structures. The former deals with improving the appearance of the whole image and there are a huge body of literature devoted to it, ranging from classical noise reduction methods like spatial- and frequency-based filtering, histogram modification [50] to diffusion filtering. The latter is to bring out details that are obscured. Among many structures of this kind, lines are of much interest since they have many applications, especially in remote sensing, military, and medical areas. There, it can be used to extract linear (or curvilinear) features such as roads, railroads, rivers, or blood vessels.

Initially, line enhancement can be done using purely image-driven methods same as in contrast enhancement tasks. These techniques are “bottom-up” approaches which are fully automatic. Being fully automatic is ideal from an operator’s point of view, but their

efficacy is limited to applications where the images are of good quality. Unfortunately, medical images are often not among these good quality images due to the acquisition methods that require much safety considerations. One would not open the whole human body to picture blood vessels inside it (even doing so, one still hardly gets the whole vessel tree). Instead, one may use less invasive techniques such as angiography where X-ray and contrast agents are used to take arterial system images. However, the structures of interest (vessels) are surrounded by many other organs, making the resulting image noisy and blurred.

To deal with medical images, many “top-down” approaches have been proposed over the last decade. The main idea is to introduce *prior knowledge* about the structure in a form of a model to aid the image analysis tasks. The model can be of image acquisition, object being imaged, or human observer. Under the variational framework, it is easy for such prior knowledge to be incorporated. The following section reviews a popular Hessian-based filter for enhancing line-like structures where the prior knowledge is expressed in the form of a local discriminant function that is based on the eigenvalues of the Hessian tensor of the image. Multiscale analysis is used in the filter to capture lines of various sizes. The filter can highlight line structures very well but sometimes causes junction suppression, which in turn yields discontinued lines. Section 3.2 presents a novel filter, called DDFB-based filter, to overcome the limitation of the Hessian-based filter. In the proposed filter, together with the knowledge used in the Hessian-based approach, another intrinsic knowledge is incorporated: lines have directional elongated structure, which can be well detected using directional filter bank (DFB). The key concept resides in replacing the estimation of the line directions via Hessian eigenvectors by the directional information available in directional images which are obtained in advance by decomposing the input image using a DFB. Finally, Section 3.3 applied the two mentioned approaches to enhance vessels in angiography images to evaluate their performances in a clinical setting.

### 3.1 Hessian Based Enhancement Filter

An intensity image  $I(\mathbf{x})$ , where  $\mathbf{x} = (x, y)$ , can be approximated by its Taylor expansion about a point  $\mathbf{x}_0$  up to the second order

$$I(\mathbf{x}) \simeq I(\mathbf{x}_0) + \Delta\mathbf{x}^T \cdot \nabla I(\mathbf{x}_0) + \frac{1}{2} \Delta\mathbf{x}^T H(I(\mathbf{x}_0)) \Delta\mathbf{x} \quad (3.1)$$

$$\Delta\mathbf{x} = \mathbf{x} - \mathbf{x}_0 \quad (3.2)$$

where  $\nabla I(\mathbf{x}_0)$  and  $H(I(\mathbf{x}_0))$  are respectively the gradient vector and the Hessian matrix at point  $\mathbf{x}_0$ .

Without loss of generality, one assumes that the object of interest is bright over a darker background. So, a line-like structure can be modeled as a tube with a Gaussian profile across its axis, which is identical to the  $x$ -axis

$$I_0(x, y) = \frac{C}{2\pi\sigma_0^2} e^{-\frac{y^2}{2\sigma_0^2}}. \quad (3.3)$$

The Hessian of the above model is then expressed as

$$H = \begin{bmatrix} \frac{\partial^2 I_0}{\partial x^2} & \frac{\partial^2 I_0}{\partial x \partial y} \\ \frac{\partial^2 I_0}{\partial x \partial y} & \frac{\partial^2 I_0}{\partial y^2} \end{bmatrix} = \begin{bmatrix} 0 & 0 \\ 0 & \frac{y^2 - \sigma_0^2}{\sigma_0^4} I_0 \end{bmatrix} \quad (3.4)$$

and its eigenvalues and eigenvectors

$$\begin{aligned} \lambda_1 &= 0 & ; & & \lambda_2 &= \frac{y^2 - \sigma_0^2}{\sigma_0^4} I_0 \\ \vec{v}_1 &= (1, 0); & & & \vec{v}_2 &= (0, 1). \end{aligned} \quad (3.5)$$

Inside the tube,  $|y| < \sigma_0$  and thus a line-like structure is declared when  $\lambda_2 < 0$  and  $R = \left| \frac{\lambda_1}{\lambda_2} \right| \ll 1$ , leading to the enhancement filter [48]

$$\psi(\mathbf{x}) = \begin{cases} 0 & \text{if } \lambda_2 > 0, \\ \mu \exp\left(-\frac{R^2}{2\beta^2}\right) & \text{else} \end{cases} \quad (3.6)$$

where  $\mu$  and  $\beta$  are constant.

In order to capture lines with various sizes, one should compute the gradient and the Hessian at multiple scales  $\sigma$  in a certain range. In this case, the only way to ensure the well-posed properties, such as linearity, translation invariance, rotation invariance, and re-scaling invariance, is the use of linear scale space theory [44, 69], in which differentiation is calculated by a convolution with derivatives of a Gaussian

$$I_x = \sigma^\gamma G_{x,\sigma} * I ; I_y = \sigma^\gamma G_{y,\sigma} * I \quad (3.7)$$

where  $I_x$  and  $I_y$  are respectively the spatial derivatives in  $x$ - and  $y$ -direction of the image  $I(x, y)$  and  $G_{x,\sigma}$  and  $G_{y,\sigma}$  spatial derivatives of a Gaussian with standard deviation  $\sigma$ :

$$G_\sigma(x, y) = \frac{1}{2\pi\sigma^2} e^{-\frac{x^2+y^2}{2\sigma^2}}. \quad (3.8)$$

The parameter  $\gamma$  was proposed by Lindeberg [69, 70] to normalize the derivatives of the image. This normalization is necessary for comparison of the response of differentiations at multiple scales because the intensity and its derivatives are decreasing functions of scale. In line enhancement applications where no scale is preferred,  $\gamma$  is usually set to one.

When multiscale analysis is applied, the model in (3.3) is convolved with a Gaussian of standard deviation  $\sigma$ . The derivations in (3.4) and (3.5) are still correct except that  $\sigma_0$  is replaced with  $\sqrt{\sigma_0^2 + \sigma^2}$ . We can see from those derivations that at pixels inside a line ( $y^2 < \sigma_0^2$ ), we have one negative eigenvalue corresponding to the eigenvector orthogonal to the axis of the line. The other eigenvalue, which is smaller in absolute value, associates with the eigenvector having the same direction as the line axis. Note also that in this case, when the line direction ( $\vec{v}_1$ ) is aligned with the  $x$ -axis, the eigenvalues of Hessian are same as its diagonal values.

### 3.2 DDFB Based Enhancement Filter

We observe that in the Hessian-based approaches, the line's direction is first estimated via the Hessian eigenvectors and then its structure is determine based on the Hessian

eigenvalues. These are of course the local information which is prone to be erroneous in some applications due to, e.g., noise. In such cases, more global information is needed. As mentioned in the previous chapter, the DFB may be an appropriate tool to provide the global directional information. However, as discussed next, the DFB has some limitations in image analysis. Thus, a *decimation-free directional filter bank* (DDFB) is proposed and used instead. The approach is then called the DDFB-based enhancement filter. The method consists of three steps, as shown in Figure 3-1: Step 1: construction of directional images, step 2: directional image enhancement, and step 3: recombination of enhanced directional images. These steps will be described in details after the description of the DDFB.

### 3.2.1 Decimation-free directional filter bank

The subbands obtained from DFB are smaller in size as compare to the original image. The reduction in size is due to the presence of decimators. As far as image compression is concerned, decimation is a must condition. However, when DFB is employed for image analysis purposes, decimation causes two problems. One is, as one increases the directional resolution, spatial resolution starts to decrease [9], due to which one loses the correspondence among the pixels of DFB outputs. The other is, an extra process of interpolation is involved prior to enhancement or recognition computation [11, 12, 95]. This extra interpolation process not only affects the efficiency of whole system but also produces false artifacts which can be harmful especially in case of medical imagery. For example, some vessels may be broken and some can be falsely connected to some other vessels due to the artifacts produced by interpolation. So a need arises to modify directional filter bank structure in a sense that no decimation is required during analysis section. To meet that need, the authors in [41, 98] presented new rules to modify DFB. Based on those rules, the author suggests to shift the decimators and resamplers to the right of the

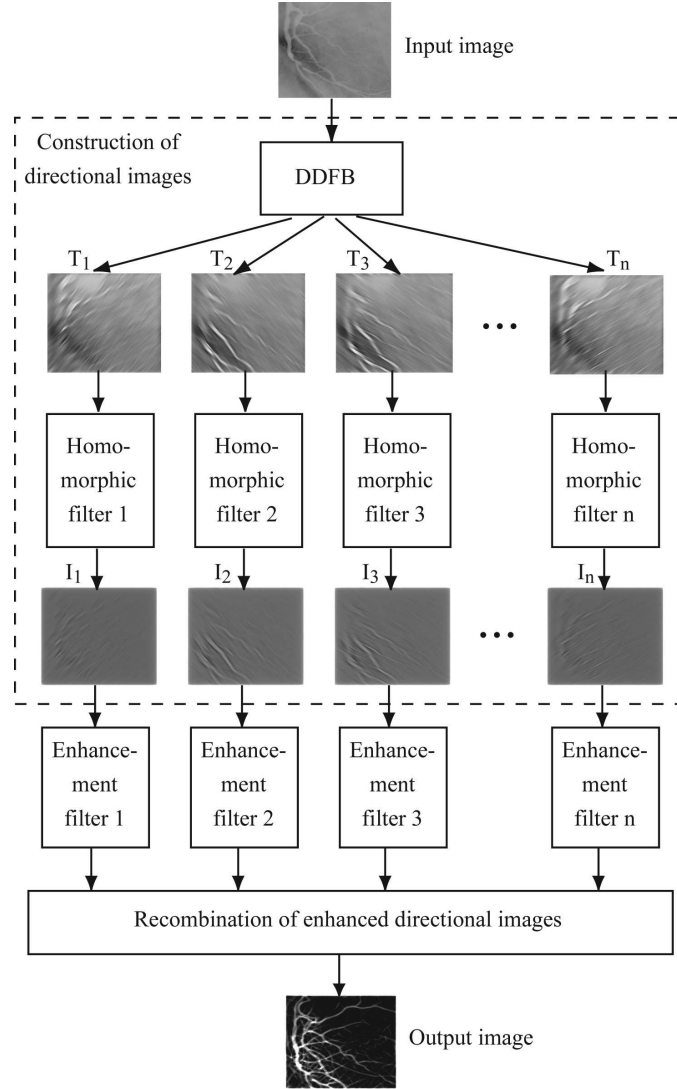


Figure 3-1: Block diagram of the proposed enhancement framework. There are three main steps: construction of directional images, line enhancement, and recombination of enhanced directional images.

filters to make a DDFB, which yields directional images rather than directional subbands. This consequently results in elimination of interpolation and naturally fits the purposes of feature analysis. The block diagram of the DDFB structure is shown in Figure 3-2.

### First stage of DDFB

Construction of the first stage of DDFB only requires two filters which are  $H_{00}(\omega_1, \omega_2)$  and  $H_{11}(\omega_1, \omega_2)$ . They have hourglass-shaped like passbands as shown in Figure 3-2(a). Hourglass-shaped filters are created by shifting the modulators present at the first stage of DFB to the left of filters using rules proposed in [11]. So the interrelation between filters used during the first stage of DFB and that of DDFB can be given as

$$H_{00}(\omega_1, \omega_2) = H_0(\omega_1 + \pi, \omega_2), \quad (3.9)$$

$$H_{11}(\omega_1, \omega_2) = H_0(\omega_1, \omega_2 + \pi), \quad (3.10)$$

where  $H_0(\omega_1, \omega_2)$  is a diamond-shaped passband filter used during the first stage of DFB. No downsampler is applied after the input image is filtered by  $H_{00}(\omega_1, \omega_2)$  and  $H_{11}(\omega_1, \omega_2)$ . By doing so, the size of outputs from the first stage becomes equal to the size of input image. Due to this reason, these outputs are named as *directional images*.

### Second stage of DDFB

The filters required for the construction of the second stage are  $H_{00}(Q^T(\omega_1, \omega_2))$  and  $H_{11}(Q^T(\omega_1, \omega_2))$ , where  $T$  represents transpose and  $Q$  is same as the Quincunx downsampling matrix in the first stage of DFB. Basically  $Q$ , which should have been in the first stage of DDFB, was shifted to the right of the second stage filter using Figure 3-3. Filters of this stage of DDFB can be related to filters of that of DFB by the following equations:

$$H_{00}(Q^T(\omega_1, \omega_2)) = H_0(Q^T(\omega_1 + \pi, \omega_2)), \quad (3.11)$$

$$H_{11}(Q^T(\omega_1, \omega_2)) = H_0(Q^T(\omega_1, \omega_2 + \pi)). \quad (3.12)$$

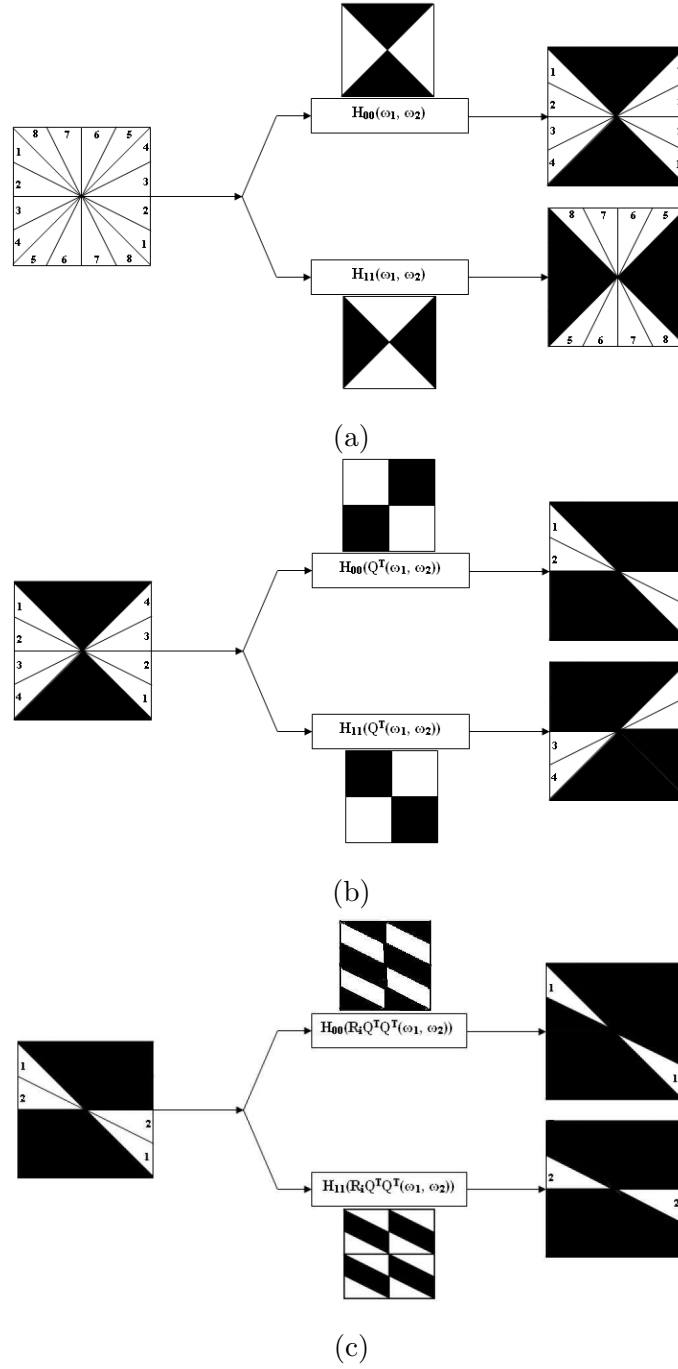


Figure 3-2: DDFB structure. a) First stage, b) Second stage, and c) Third stage. DDFB provides directional images of same size as the original image, which fits the purposes of image analysis.

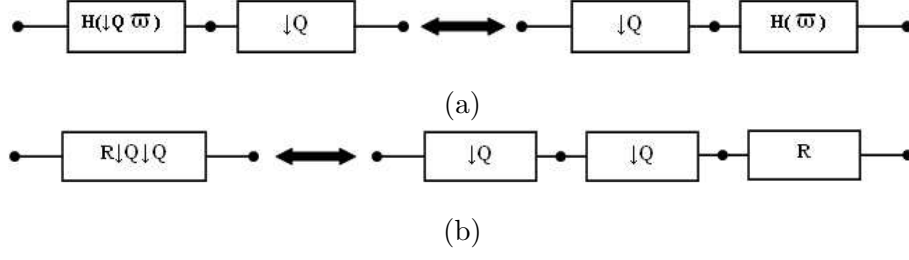


Figure 3-3: Rules used to shift resampling and downsampling matrix to the right.

Directional images obtained from the first stage of DDFB are filtered through these two filters. No further operation is required at the end of this stage. Spectral regions of directional images obtained after filtering through this stage's filters are shown in Figure 3-2(b).

### Third stage of DDFB

Filters used during the third stage of DDFB are  $H_{00}^i(\omega_1, \omega_2)$  and  $H_{11}^i(\omega_1, \omega_2)$ , where  $i = 1, 2, 3$ , and 4 as shown in Figure 3-2(c). Overall eight different filters are created to be used during this stage. Mathematically this stage of DDFB can be related to that of DFB as

$$H_{00}^i(\omega_1, \omega_2) = H_0(R_i^T Q^T Q^T(\omega_1 + \pi, \omega_2)), \quad (3.13)$$

$$H_{11}^i(\omega_1, \omega_2) = H_0(R_i^T Q^T Q^T(\omega_1, \omega_2 + \pi)), \quad (3.14)$$

where  $R_i$  and  $Q$  are respectively the same resampling and downsampling matrices as used in DFB.

Basically, one has shifted all the modulators, the downsamplers and resampling matrices present in DFB to the right of all the filters. So, at the end of the third stage, one will be left with two downsampling matrices, one resampling matrix followed by the post-sampling matrix. These matrices are not applied onto directional images. Directional images present at the third stage of DDFB are visually correct as no downsampling was

applied to input image during the whole structure of DDFB. Figure 3-4 demonstrates eight-directional images obtained by applying DDFB on the original image shown in Figure 3-6(b) with  $n = 8$  (i.e.,  $k = 3$ ).

Although eight-band DDFB is described here, it can be extended to 16-band and 32-band DDFB and so on. For this extension to take place, one can take advantage of simple extension rules for DFB as described in [96]. For a given application, to decide how many directional images are needed, one assesses how much directional resolution one is in need of, at the cost of additional computation.

Furthermore, the 2D DDFB can be extended to 3D DDFB on the same lines as 2D DFB being converted to 3D DFB as an optimum three-dimensional matched filter for linearly moving objects in noise. More details can be found in [96] where the 3D DFB is referred to as velocity selective filter bank (VSFB) for emulating the behavior of the spatio-temporal continuous wavelet transform (CWT) that has proven useful for motion estimation [83, 82]. The VSFB approach offers a computational advantage over direct implementation of the CWT in the sense that it exploits the temporal information in addition to 2D spatial coordinates which is critical in some real world applications.

### 3.2.2 A comparative analysis between DDFB and DFB

Firstly, the aliasing present in DFB is avoided by the shifting of resampling and down-sampling matrices to the right. By this way, one is able to get directional images of the same size as the original image. One of the main advantages of DDFB is the fact that due to absence of aliasing, directional images are visually correct.

Secondly, in DFB, spatial resolution decreases at least as fast as the directional resolution increases. The more one knows about the orientation of a feature, the less he knows about its length and vice versa [9]. However, in DDFB, there is no interdependency between the length and orientation of the feature. This means that increasing directional

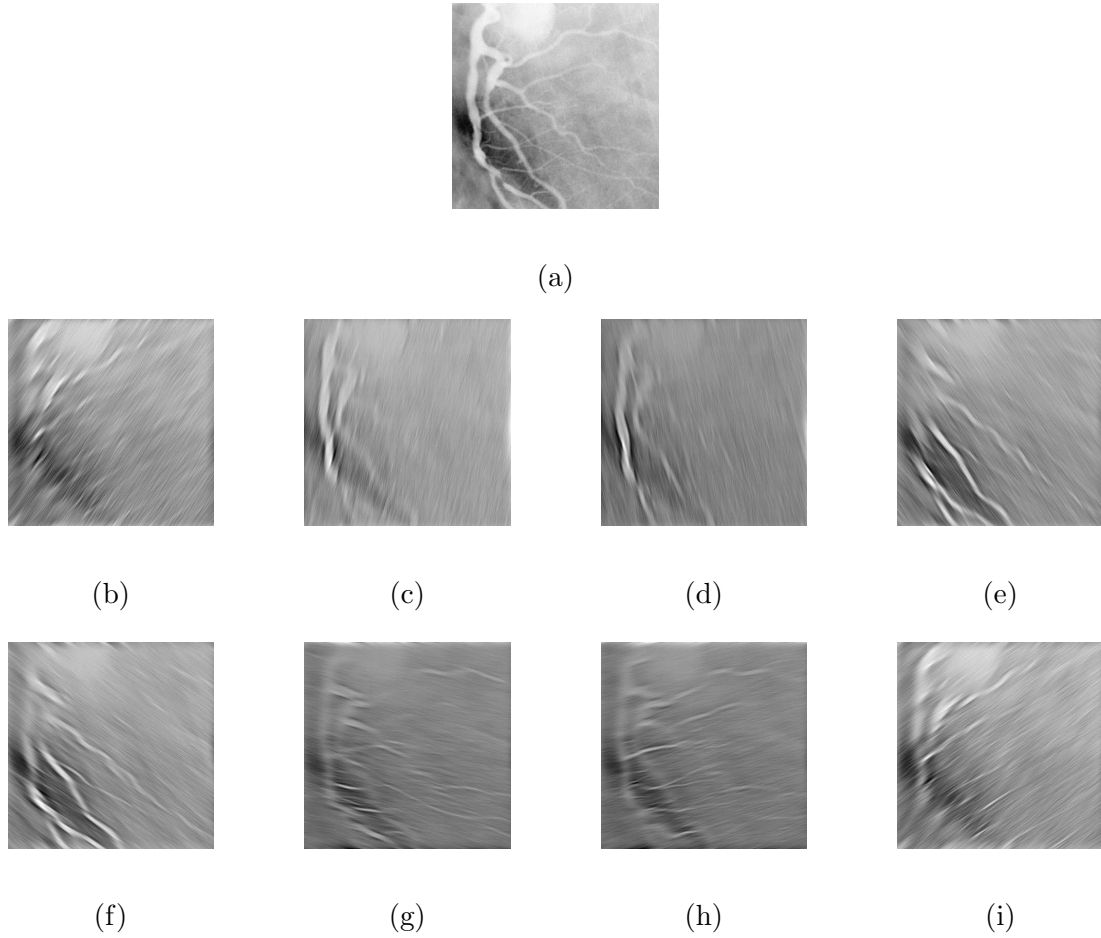


Figure 3-4: Directional images obtained using DDFB with  $n = 8$ . (a) Input image, (b) the directional image corresponding to orientations in the range  $45-67.5^\circ$ , (c)  $67.5-90^\circ$ , (d)  $90-112.5^\circ$ , (e)  $112.5-135^\circ$ , (f)  $135-157.5^\circ$ , (g)  $157.5-180^\circ$ , (h)  $0-22.5^\circ$ , and (i)  $22.5-45^\circ$ .

resolution does not affect spatial resolution. Although in DDFB no downsamplers are employed at all, complexity will be higher due to the increased data size. Nevertheless, artifacts due to aliasing are avoided in reconstruction. This is important in medical images as some aliasing artifacts can be misleading.

Thirdly, in DDFB, since directional images are of same size as the original image, no interpolation step to establish one-to-one pixel correspondence is needed like in DFB. As a result, DDFB avoids false artifacts produced during interpolation in subbands.

Finally, the synthesis section of DFB requires exactly the reverse process of the analysis section. In contrast, at any stage in DDFB, synthesis can be achieved by the simple addition of directional images. So the overall process of synthesis section is simplified in DDFB.

### 3.2.3 Step 1: construction of directional images

The input image is decomposed to  $n = 2^k$  ( $k = 1, 2, \dots$ ) directional images  $T_i$ . The motivation here is to detect thin and low-contrast line-like structures while avoiding false detection of blob-like structures. Directional segregation property of DDFB is helpful in eliminating randomly oriented noise patterns and blob-like structures which normally yield similar amplitudes in all directional images (see Figure 3-4).

Before these directional images are enhanced in the next step, they are utilized to efficiently remove non-uniform illumination (NUI), which limits the correct enhancement. One conventional approach to correct NUI is to directly apply homomorphic filtering [50] on the original image. A general image can be characterized by two components: (1) the illumination component, which changes slowly in a neighborhood due to light source characteristics and thus is low-frequency and (2) the reflectance component, which is determined by the amount of light reflected by the objects and therefore is high-frequency. The homomorphic filter is to suppress the low-frequency component while enhance the

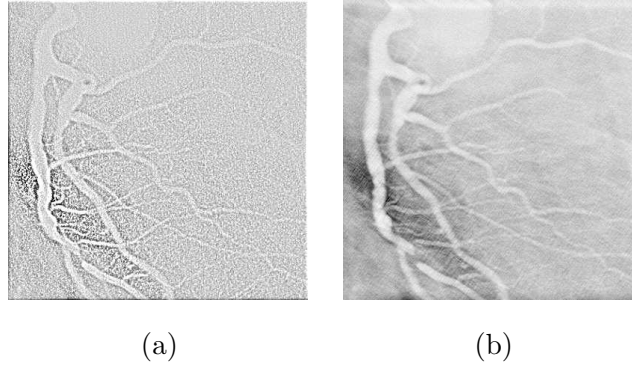


Figure 3-5: Results of NUI removal for the input image in Figure 3-4 using homomorphic filter. (a) Direct filtering on the original image and (b) filtering on directional images and then re-combining them. The former amplifies background noise whereas the latter does not.

high-frequency one. However, the direct application of homomorphic filtering is sometimes unsatisfactory because it may enhance high-frequency background noise as can be seen in Figure 3-5(a). Tuning the filter parameters in this case suffers from a compromise: the more NUI is removed, the more background noise is enhanced. Differently, one can employ several homomorphic filters, each of which matched with its corresponding directional image as shown in the dash-boundary box in Figure 3-1. This new arrangement provides a better control on the parameters of individual homomorphic filter. For the sake of comparison, the recombination of directional homomorphic filtered images is shown in Figure 3-5(b). The image is now largely uniformly illuminated without unexpected noise amplification.

### 3.2.4 Step 2: directional image enhancement

As pointed out in Section 3.1, in order to compute the Hessian eigenvalues with less noise sensitiveness, it is necessary to align the line direction with the  $x$ -axis. One possible way is to rotate the directional images. Nevertheless, image rotation requires interpolation

which is likely to create artifacts and thus is harmful especially in case of medical imagery. Therefore, one can rotate the coordinates rather than the directional images.

Suppose the directional image  $I_i$  ( $i = 1, \dots, n$ ) corresponds to the orientations ranging from  $\theta_{i,min}$  to  $\theta_{i,max}$  (counterclockwise angle). Its associated coordinates  $Oxy$  will be rotated to  $Ox'y'$  by an amount as large as the mean value  $\theta_i$

$$\theta_i = \frac{\theta_{i,min} + \theta_{i,max}}{2}. \quad (3.15)$$

According to (3.26)–(3.28) in the Appendix section, Hessian matrix of the directional image  $I_i$  in the new coordinates  $Ox'y'$  is determined as

$$H' \equiv \begin{bmatrix} h_{11} & h_{12} \\ h_{21} & h_{22} \end{bmatrix} = \begin{bmatrix} \frac{\partial^2 I_i}{\partial x'^2} & \frac{\partial^2 I_i}{\partial x' \partial y'} \\ \frac{\partial^2 I_i}{\partial x' \partial y'} & \frac{\partial^2 I_i}{\partial y'^2} \end{bmatrix} \quad (3.16)$$

where

$$\frac{\partial^2 I_i}{\partial x'^2} = \frac{\partial^2 I_i}{\partial x^2} \cos^2 \theta_i + \frac{\partial^2 I_i}{\partial x \partial y} \sin(2\theta_i) + \frac{\partial^2 I_i}{\partial y^2} \sin^2 \theta_i, \quad (3.17)$$

$$\frac{\partial^2 I_i}{\partial y'^2} = \frac{\partial^2 I_i}{\partial x^2} \sin^2 \theta_i - \frac{\partial^2 I_i}{\partial x \partial y} \sin(2\theta_i) + \frac{\partial^2 I_i}{\partial y^2} \cos^2 \theta_i, \quad (3.18)$$

$$\frac{\partial^2 I_i}{\partial x' \partial y'} = -\frac{1}{2} \frac{\partial^2 I_i}{\partial x^2} \sin(2\theta_i) + \frac{\partial^2 I_i}{\partial x \partial y} \cos(2\theta_i) + \frac{1}{2} \frac{\partial^2 I_i}{\partial y^2} \sin(2\theta_i). \quad (3.19)$$

The Hessian eigenvalues are then defined by the diagonal values of  $H'$ . As proven in (3.3)–(3.5), these values are

$$h_{11} = 0, \quad h_{22} = \frac{y'^2 - (\sigma_0^2 + \sigma^2)}{(\sigma_0^2 + \sigma^2)^2} I_0(x', y') \quad (3.20)$$

where  $\sigma$  selected in a range  $S$  is the standard deviation of the Gaussian kernel used in the multiscale analysis.

Practically, the line axis is not, in general, identical to the  $x'$ -axis and so  $h_{11} \approx 0$ . Inside the line,  $|y'| < \sqrt{\sigma_0^2 + \sigma^2}$  and thus  $h_{22}$  is negative. Therefore, line pixels are declared when  $h_{22} < 0$  and  $\left| \frac{h_{11}}{h_{22}} \right| < 1$ .

To distinguish background pixels from others, one define a structureness measurement

$$C = \sqrt{h_{11}^2 + h_{22}^2}. \quad (3.21)$$

This structureness  $C$  should be low for background which has no structure and small derivative magnitude.

Based on the above observations, the line filter output, which is similar to that in [48], can be defined as

$$\phi_\sigma(p) = \eta(h_{22}) \exp\left(-\frac{R^2}{2\beta^2}\right) \left[1 - \exp\left(-\frac{C^2}{2\gamma^2}\right)\right] \quad (3.22)$$

where  $p = (x', y')$ ,  $R = \frac{h_{11}}{h_{22}}$ ,  $\beta$  and  $\gamma$  are adjusting constants, and

$$\eta(z) = \begin{cases} 0 & \text{if } z \geq 0; \\ 1 & \text{if } z < 0. \end{cases} \quad (3.23)$$

The filter is analyzed at different scales  $\sigma$  in a range  $S$ . When the scale matches the size of the line, the filter response will be maximum. Therefore, the final line filter response is

$$\Phi(p) = \max_{\sigma \in S} \phi_\sigma(p). \quad (3.24)$$

One filter (3.24) is applied to one directional image to enhance line structures in it.

### 3.2.5 Step 3: recombination of enhanced directional images

Each directional image now contains enhanced lines in its directional range and is called the enhanced directional image.

Denote  $\Phi_i(p), i = 1, \dots, n$ , as the enhanced directional images. As mentioned in Section 3.2.2, the synthesis of DDFB is achieved by simply summing all directional images. Thus, the output enhanced image  $F(p)$  can be obtained by

$$F(p) = \frac{1}{n} \sum_{i=1}^n \Phi_i(p). \quad (3.25)$$

The whole filtering procedures can be summarized as follows. First, the input angiography image is decomposed into  $n = 2^k$  ( $k = 1, 2, \dots$ ) directional images  $T_i$  using DDFB. Then,  $n$  distinct homomorphic filters are employed to  $n$  respective directional images to remove non-uniform illumination. The output uniformly illuminated directional images  $I_i$  are enhanced according to (3.22)–(3.24). Finally, all enhanced directional images are recombined to yield the final filtered image  $F$  as in (3.25).

### 3.3 Application: Vessel Enhancement

Correct assessment, especially accurate visualization and quantification, of blood vessels reflected in X-ray angiograms or angiography images plays a significant role in a number of clinical procedures. For various medical diagnostic tasks, it is necessary to measure vessel width, reflectivity, tortuosity, and abnormal branching. For example, detecting the occurrence of vessels of a certain width may reveal the signs of stenoses. Grading of stenoses is of importance to diagnose the severity of vascular disease and then to determine the treatment therapy [87, 40]. Moreover, planning and performing neurosurgical procedures require an exact insight into blood vessels and their branches, which exhibit much variability. In planning, they provide information on where the blood is drawn and drained to differentiate between the feeding vessel and the transgressing vessel. While transgressing vessels need to be preserved, feeding ones are selectively closed through the artery in interventional neuroradiology such as brain arteriovenous malformations treatment. During surgery the vessels serve to provide landmarks and guidelines to the lesion. In short, the accuracy in navigation and localization of clinical procedures is determined by how minute and subtle the vascular information is. Although it is possible for medical experts to delineate vessels, manual delineation of the vasculature becomes tedious or even impossible when the number of vessels in an image is large or when a large number of images is acquired. Therefore, the development of automatic and accurate vessel-tree reconstruction

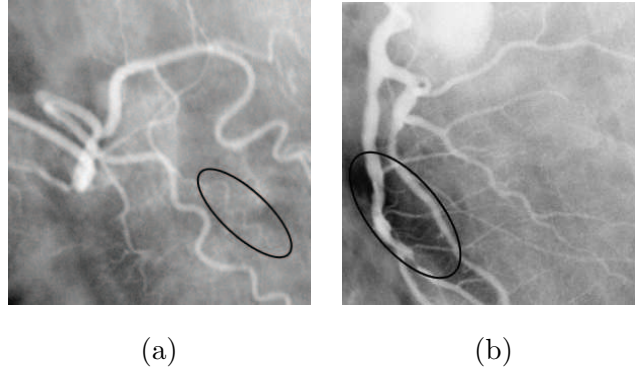


Figure 3-6: Angiography images with typical hindrances for accurate vessel-tree reconstruction such as (a) low-contrast vessels and (b) non-uniform illumination.

from angiograms is highly desirable. Unfortunately, it has proven to be a challenging task. The key fact is that vessels cannot be characterized uniformly. Because the blood either by itself or by the contrast agent it carries is responsible for the vessel contrast to the background, large vessels usually have high contrast while small ones resemble the background (see Figure 3-6(a)). Non-uniform illumination as shown in Figure 3-6(b), which is one of the major sources of angiography image degradation [52], is also a hindrance for accurate reconstruction because it is likely to make an individual vessel broken into several segments. According to [72, 58], current automatic computer-assisted procedures are still far from providing a precise spatial representation of the vessel tree.

In order to achieve an accurate vessel-tree reconstruction, the vessel enhancement procedure is an important preprocessing step. There are a variety of vessel enhancement methods in the literature. Some works have taken linear filtering approach. Poli and Valli [102] proposed a computationally efficient algorithm based on a set of linear filters, obtained as linear combinations of properly shifted Gaussian kernels, sensitive to vessels of different orientation and radius. Another type of linear filters, the morphological connected-set filter, was utilized by Wilkinson and Westenberg [85] to capture filamentous structures. Together with a shape criterion that can distinguish filamentous structures

from others, connected-set filters can help to extract filamentous details without distortion. Similarly, Eiho and Qian [38] and Zana and Klein [144] used morphological operators such as erosion, dilation, and Top-Hat to enhance the shape of the artery and remove other points. However, these methods were unable to suppress sudden noise and edge noise and were less efficient on capillaries. A different linear filtering approach which combined Laplacian filter with fuzzy logic was presented by Yan et al. [140]. Small vessels were not captured satisfactorily by this approach either.

Non-linear anisotropic filtering has also been applied to vessel enhancement (Krissian et al. [61, 60], Orkisz et al. [88]). This method searches for the local orientation of a vessel to perform anisotropic smoothing without blurring its edge. While Krissian et al. performed a particular version of anisotropic diffusion, Orkisz et al. used a kind of filter bank called “sticks”, which can be seen as a set of directional structuring elements. Similar approaches were also proposed by Czerwinski et al. [32, 33], Kutka and Stier [64], Chen and Hale [26], and Du et al. [36, 35]. The last two combined the outputs of directional operators without an explicit extraction of the vessel local orientation. The main disadvantage of the methods in this category is that they can hardly detect vessels in a wide range due to the fixed scale analysis. Although they can be extended to multiple scales by using sticks of variable length, the computation time would increase very much.

Hessian-based multiscale filtering has been proposed in a number of vessel enhancement approaches [48, 46, 47, 114, 71, 118]. One advantage of the approaches in this category is that vessels in a large range of diameters can be captured due to the multiscale analysis. In these methods, an input image is first convolved with the derivatives of a Gaussian at multiple scales and then the Hessian matrix is analyzed at each pixel in the resulting image to determine the local shape of the structures at that pixel (see Figure 3-7(a)). The ratio between the minimum and the maximum Hessian eigenvalues is small for line-like structures but it should be high for blob-like ones. Specifically, Krissian et al. [62]

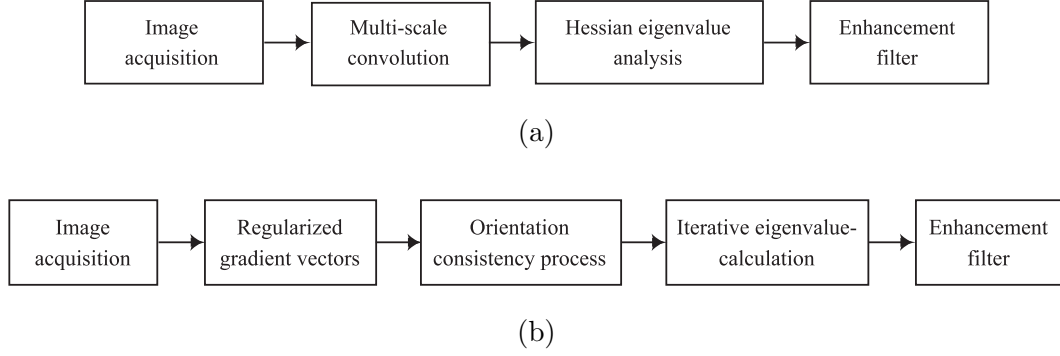


Figure 3-7: Block diagrams of a) conventional Hessian-based and b) correlation-based approaches.

introduced several models of vessels and used the Hessian eigenvalues to define a set of candidate pixels which could be the centerlines of vessels. At each of these candidates, pre-defined multiscale response functions were computed to determine the likelihood of the pixel corresponding to vessels of different scales (radii). The drawbacks of the Hessian-based approaches are that they are highly sensitive to noise due to the second-order derivatives and that they tend to suppress junctions since junctions are characterized same as the blob-like structures. Junction suppression leads to the discontinuity of the vessel network, which is of course undesirable. To deal with this problem, Agam et al. [3] proposed a filter model which is based on the correlation matrix of the regularized gradient vectors (first-order derivatives), to avoid the need for second-order derivatives as demonstrated in Figure 3-7(b). This model generated good performance when dealing with thoracic CT images. However, when dealing with angiography images, which are more noisy and suffer from the non-uniform illumination, it shares the same limitations of Hessian-based filters in finding small and low-contrast vessels. The reason is that it is still using the Hessian eigenvalues to pre-select the vessel-candidate pixels at which the filter is applied.

This section presents the evaluation of the DDFB-based enhancement filter on vessel

enhancement. The study focuses on the processing of 2D images such as X-ray angiography and retinal photography images. In such applications as intervention planning, blood vessel and retinal pathology, blood-flow analysis, or drug evaluation, 2D imaging is often the method of choice since it provides sufficiently good results although 3D imaging techniques would provide more information.

Experiments are performed with both synthetic images and real angiography and retinal photography images to verify the performance of the DDFB-based filter in comparison with the filters introduced by Frangi et al. [48] and Shikata et al. [118], which are considered as the standard techniques. In the DDFB-based filter, the input image is decomposed to 16 directional images ( $n = 16$ ) as a trade-off between performance and computation time. If not stated otherwise, the scale range  $S = \{1, \sqrt{2}, 2, 2\sqrt{2}, 4\}$  is used for all three models as proposed in [118]. The computation time (cpu time, in seconds), performed on an Intel Duo Core 1.86 GHz with 1 GB of RAM, will be given in each case.

### 3.3.1 Junction suppression

Figure 3-8 shows the results of an synthetic image of size  $158 \times 176$  which was processed by the three filter models. The synthetic image is designed to contain vessels of different sizes and junctions of different types. It is possible to see that the Frangi and Shikata filters suppress junctions while the DDFB-based approach does not. The suppressed junctions make vessels discontinuous. Although this error may be small, it can cause the splitting of a single vessel, which in turn has a critical effect on the vessel-tree reconstruction accuracy.

It is the use of directional image decomposition that makes the proposed model work. Normally, a vessel has one principal direction, which is mathematically indicated by a small ratio between the minimum and maximum Hessian eigenvalue. Meanwhile, at a junction, where a vessel branches off, there are more than two principal directions, and

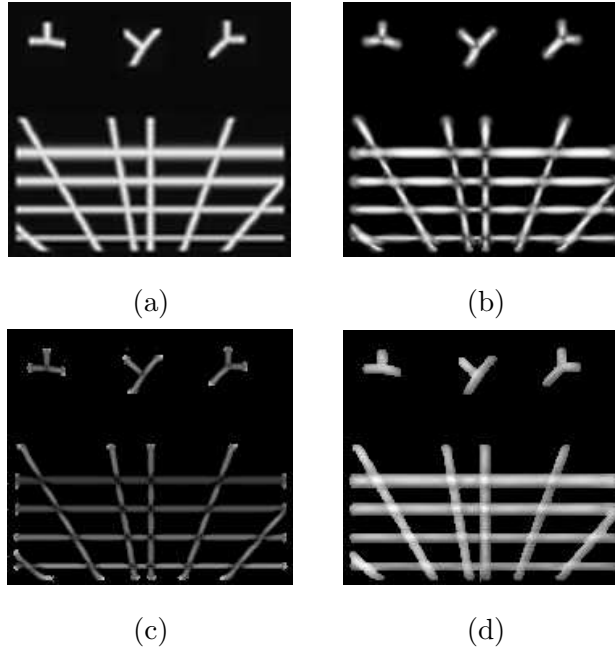


Figure 3-8: Vessel enhancement results. (a) The original synthetic image. (b) Enhanced image by the Frangi method,  $\text{cpu} = 6.70$  s, (c) by the Shikata method, 6.65 s, and (d) by our approach, 8.44 s. The Frangi and Shikata methods suppress the junctions while ours does not.

thus the ratio of two eigenvalues is no longer small. As a result, the Frangi and Shikata filters consider those points as noise and then suppress them. The DDFB-based approach, on the other hand, decomposes the input image to various directional images, each of which contains vessels with similar orientations. Consequently, junctions do not exist in directional images and so are not suppressed during the filtering process. After that, due to the recombination of enhanced directional images, junctions are re-constructed at those points which have vessel values in more than two directional images. Therefore, junctions are not only preserved but also enhanced in the final output image.

### 3.3.2 Noise sensitivity

To compare the performances of the filters with respect to noise levels, I construct a set of phantom images as follows. First of all, one original phantom image with various typical hindrances for accurate vessel detection is created (see Figure 3-9(a)) and later on used as the “ground truth”. In this  $512 \times 512$  sized phantom, fifteen vessel segments are constructed for a wide range of widths and directions to model a vascular image. For the sake of description, these segments are numbered in an increasing order from left to right and top to bottom. Segment 1 represents distinct branch points in a real angiography image, and Segments 4 through 7 characterize junctions with different widths while Segment 3 stands for vessel orientation diversity. Moreover, Segments 2, 12, and 14 are designed deliberately to have variable cross-sectional widths. In addition, common challenges such as the presence of close parallel vessels (Segments 8, 9, and 11), very thin vessels (Segment 10), discontinued vessels (Segment 13), and vessels with variable intensities along their length (Segment 15) are also incorporated into the phantom. Next, based on this original phantom, a series of testing data are generated by adding various levels of white noise, having standard deviation (SD) ranging from 5% to 80%. The noise SD is calculated as a percentage of the 8-bit dynamic range of the image (0 – 255). To

my experience, the data with noise SD of 80% represents the most possibly challenging situation, which is well beyond any worst case of real angiography images. Figures 3-9(b)-(d) present three samples of the testing data having noise SD of 5%, 45%, and 80%, respectively.

The three filters are then applied on those phantom images and the outputs are segmented using global thresholding to compare with the “ground truth”. The quantitative performance is measured with receiver operating characteristic (ROC) curves [43]. An ROC curve plots the rate of pixels correctly classified as vessels (i.e., true positive rate or *sensitivity*) against the rate of pixels incorrectly classified as vessels (i.e., false positive rate or  $1 - \text{specificity}$ ). The rates are obtained with all possible threshold choices. Each discrete threshold value produces a (sensitivity,  $1 - \text{specificity}$ ) pair corresponding to a single point in the curve. The closer the curve approaches the northwest corner, the better the filter performs. A single scalar value reflecting this behavior is the area under the ROC curve (AUC), which is 1 for perfect performance. Note that to get rid of the large number of background pixels correctly classified, one can compute the sensitivity and specificity in the vicinity of the “ground truth” vessels which can be obtained by dilation. In our experiment, the vicinity size is selected such that the number of background pixels is comparable to that of the vessel pixels.

Figure 3-10 shows sample enhancement results for the data with noise SD of 10%. The performances of the three filters applied on the whole testing data set are presented in Figure 3-11. In this figure, the AUC measures are plotted as a function of the noise SD. We can see that the DDFB-based filter outperforms the others for this data set. Specifically, compared to the Frangi filter, it generates similar results in case of low noise (i.e., SD of 5-10%) but performs much better when the noise level increases.

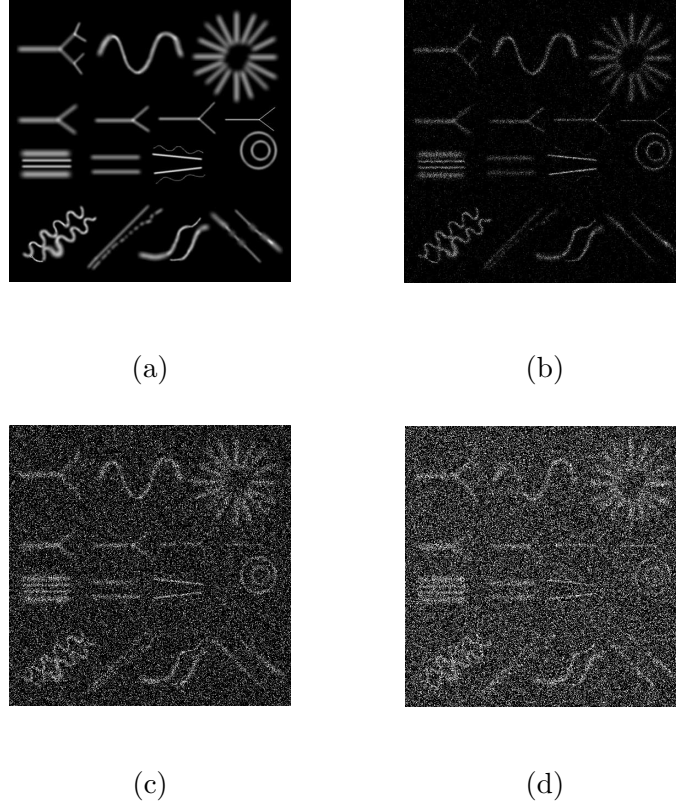
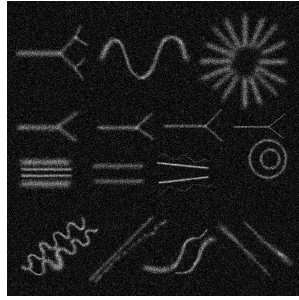
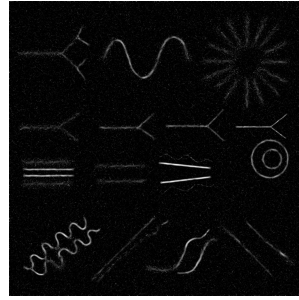


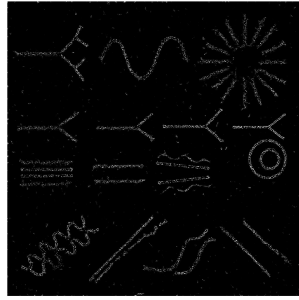
Figure 3-9: Testing data with a size of  $512 \times 512$  and various amount of white noise. (a) Original phantom (obtained from [www.ecse.rpi.edu/censsis/phantom](http://www.ecse.rpi.edu/censsis/phantom)). (b) Noisy phantom with noise SD of 5%, (c) 45%, and (d) 80%. The testing data incorporate most of the common challenges to exact vessel extraction procedure such as image noise and presence of close parallel vessels, very thin vessels, discontinued vessels, and vessels with variable intensities along their length.



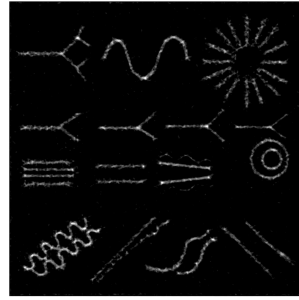
(a)



(b)



(c)



(d)

Figure 3-10: Sample vessel enhancement results. (a) Sample phantom image with noise SD of 10%. (b) Enhanced image by the Frangi filter,  $\text{cpu} = 66.42$  s, (c) by the Shikata filter, 65.86 s, and (d) by DDFB-based filter, 81.27 s.

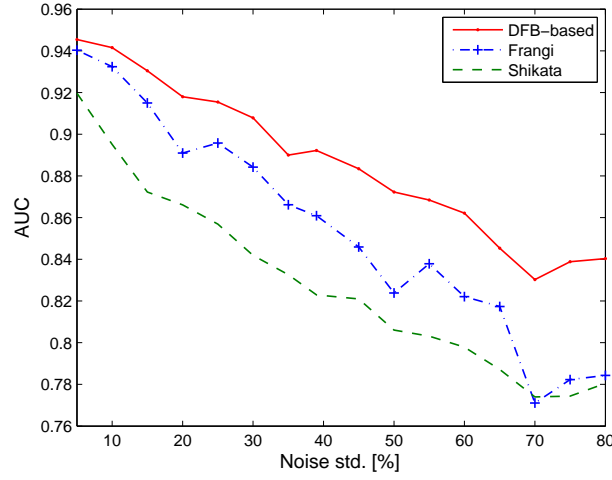


Figure 3-11: Performance plots vs. noise levels for the testing data described in Figure 3-9. In average, the AUC of DDFB-based filter is relatively 3.74% and 7.02% larger than that of Frangi and Shikata filters respectively.

### 3.3.3 Real data

Similar to junction suppression problem, small vessel enhancement is critical because those thin vessels which may appear broken or disconnected from larger structures will often be omitted in the reconstruction procedures. Figure 3-12 shows the enhancement results of the three filters applied on two real angiography images. The images are of size  $401 \times 401$  and belong to cardiac part of the human body. As can be observed, the Frangi filter gives good results with large vessels but fails to detect small ones while the Shikata model is able to enhance small vessels but unfortunately enhances background noise also. Conversely, the DDFB-based filter can enhance small vessels with more continuous appearances.

Due to lack of ground truths for the above images, I leave them as qualitative results but instead utilize the Utrecht database<sup>1</sup> to quantitatively evaluate the three filters on

<sup>1</sup>Available at <http://www.isi.uu.nl/Research/Databases/DRIVE/>

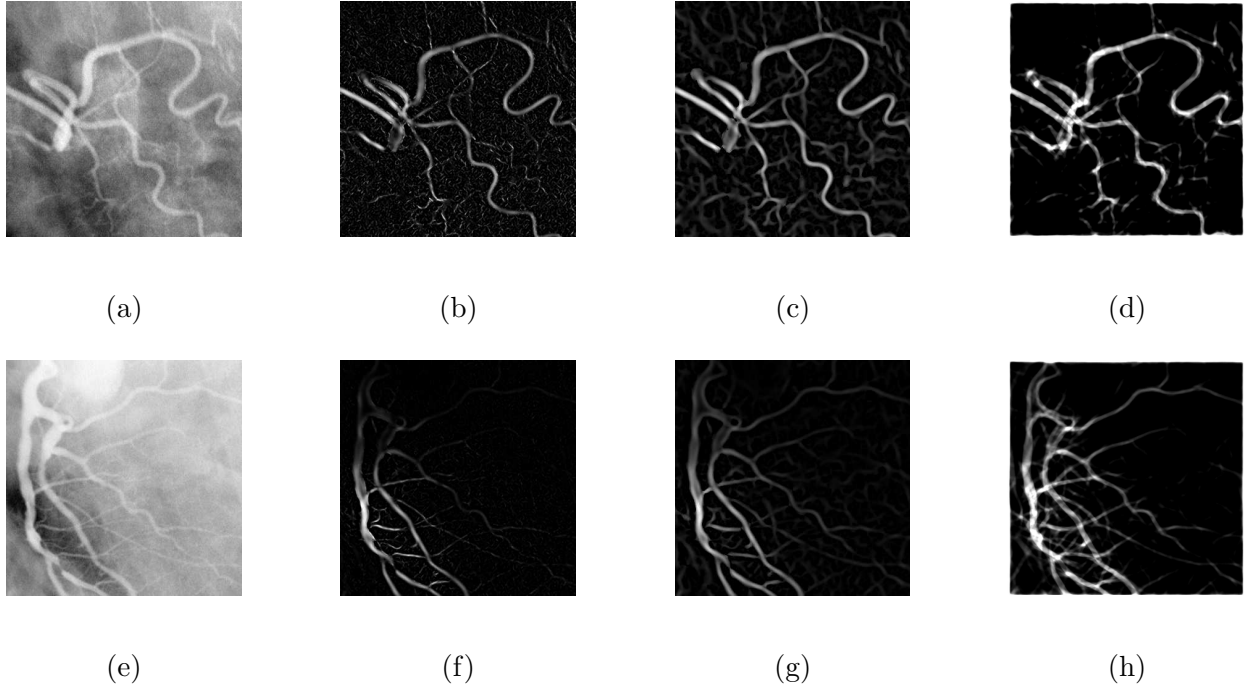


Figure 3-12: Qualitative results for two cardiac angiography images. (a) and (e): Original images, (b) and (f): Enhanced images by Frangi method,  $\text{cpu} = 43.22$  s each, (c) and (g): by Shikata method, 43.11 s, and (d) and (h): by DDFB-based approach, 49.08 s. The Frangi and Shikata models fail to correctly enhance small vessels but the proposed approach succeeds.

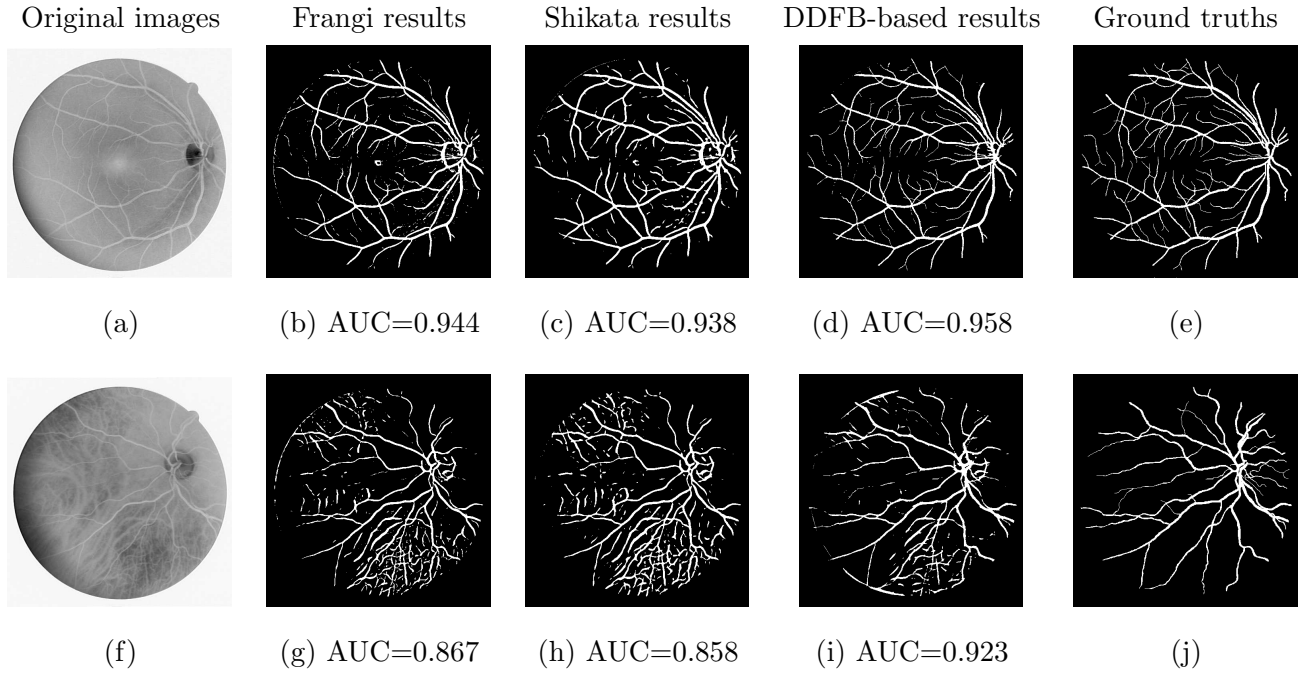


Figure 3-13: Best and worst results for the Utrecht database in terms of AUC measures. For each image, the Frangi method  $\text{cpu} = 87.02$  s, Shikata 85.55 s, and DDFB-based 93.46 s.

real medical images. This database contains 40 retinal color images of size  $584 \times 565$  and their corresponding vasculatures manually segmented by an expert, which are used as ground truths. In this experiment, the negative of the green channel of the image is used (see e.g., Figures 3-13(a) and (f)). The green channel is selected since it gives the highest contrast and it is made negative because the filters assume that vessels are brighter than the background as stated in Section 3.1. Since vessels in these images are relatively small, the scale range  $S = \{\sqrt{2}/2, 1, \sqrt{2}, 2, 2\sqrt{2}\}$  is used. The validation process is performed same as in Section 3.3.2.

Figure 3-13 shows for the results with highest and lowest AUC measures. The performances of the three filters for the whole database are presented in Figure 3-14 and the

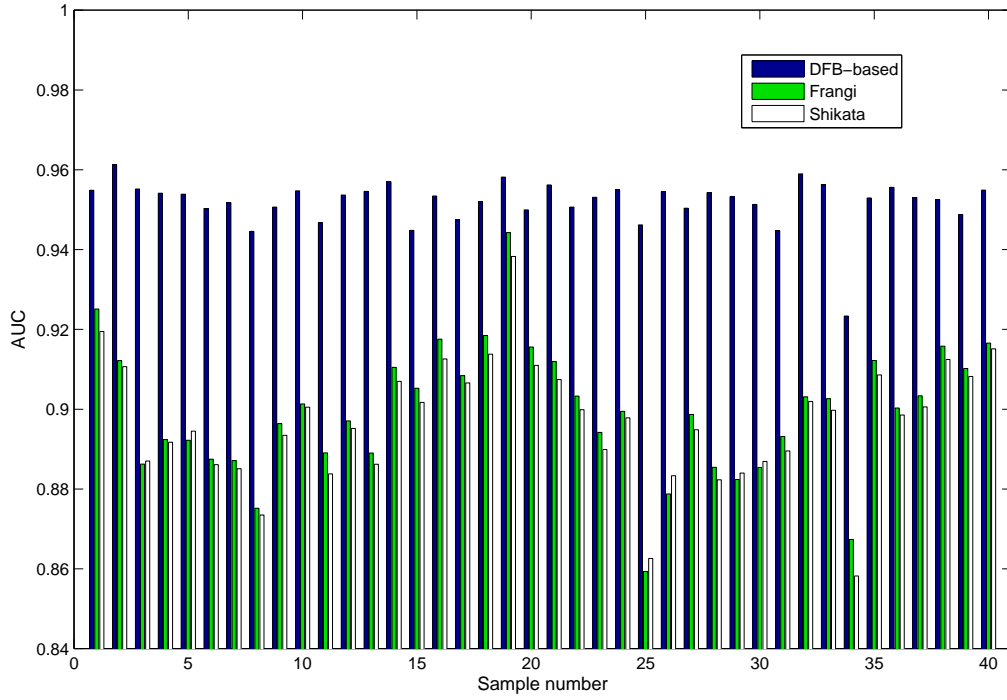


Figure 3-14: Performance plots vs. sample number for the Utrecht database. The mean and SD of these measurements are given in Table 3.1. In average, the DDFB-based filter is 5.8% and 6.2% better than the Frangi and the Shikata filters respectively.

Table 3.1: Mean and SD of the AUC of the three methods performed on the Utrecht database.

	Frangi	Shikata	DDFB-based
Mean	0.8994	0.8970	0.9519
SD	0.0162	0.0152	0.0060

mean and standard deviation are given in Table 3.1.

To evaluate the noise sensitivity of the filters for retinal images, I create a testing data set similar to the previous section. Here, I use 40 ground truths of the Utrecht database as original phantom images; each is added with noise having SD ranging from 5% to 80%. By this way, we will have several images per noise level. Figure 3-15 plots variation ranges of AUC per every noise level. Again, it can be seen that the DDFB-based filter is least sensitive to noise among the three filters.

### 3.3.4 Discussions

This section has presented a novel approach of vessel enhancement for 2D angiography images using directional decomposition. The novelty resides in adapting the Hessian-based filters to be used in the directional images. In particular, this permits the estimation of the vessel directions without the Hessian eigen-analysis. The advantage of the proposed approach is that it distinguishes all vessels at bifurcations and crossings. At these configurations, one will obtain different vessel directions and thus different second derivatives that are different from the Hessian eigenvalues (of the original image).

The larger the number of directional images  $n$ , the smaller the directional range and as a result the more accurate the eigenvalue estimation is, at the cost of the computation time. While the cpu time increases rather linearly with  $n$ , the performance does not increase as much. A pilot experiment showed that the DDFB-based filter with  $n = 16$

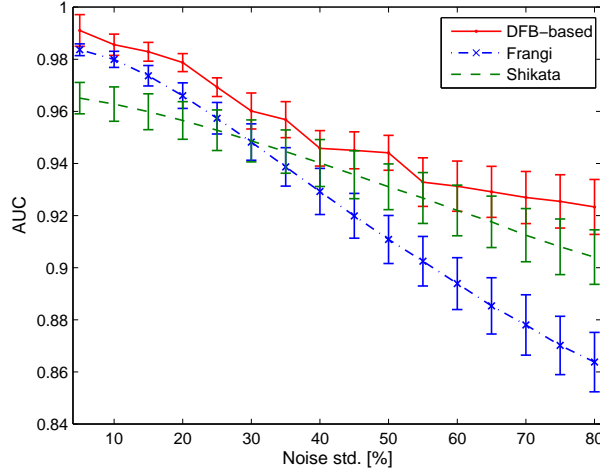


Figure 3-15: Mean and SD bar plots of AUC vs. noise levels for 40 noise-added ground truths of the retinal images. In average, the AUC of DDFB-based filter is relatively 3.47% and 2.36% larger than that of Frangi and Shikata filters respectively.

performed about 4% better than that with  $n = 8$  but the cpu time almost doubled. Also, it can be seen from the previous section that the cpu time of the this filter with  $n = 16$  is comparable to those of the Frangi and Shikata filters (e.g., respectively, 93 s, 87 s, and 85 s for a retinal image of size  $584 \times 565$ ). With those remarks, the author chose  $n = 16$  rather than 32 or higher because the benefit on the relatively small performance gain is not worth the cost of much more computation time.

Another advantage of the DDFB-based approach is the NUI removal using homomorphic filters on directional images. Looking at the dark disks in the retinal images in Figures 3-13(a) and (f), one can see that the DDFB-based filter can reduce these artifacts compared to the two other filters. Also, it has removed the bright blob at the center of the image in Figure 3-13(a) whereas the others could not.

The experimental results show that the DDFB-based filter overcomes the limitations

of conventional Hessian-based methods such as junction suppression and noise sensitivity. It also performs better on real angiography images. In conclusion, the author considers the proposed DDFB-based filter a better candidate for pre-processing in an accurate vessel-tree reconstruction in clinical tasks.

Although this work focuses on 2D images, the proposed approach can be extended to deal with 3D images by extending DDFB to 3D, which is a future work. The 2D-to-3D DDFB extension can be done on the same lines as 2D DFB being converted to 3D DFB as described in [96]. Another aspect of future study will be on the clinical usage of the proposed technique.

## Appendix

### Hessian Matrix in New Rotated Coordinates

Given a function  $f(x, y)$  in the coordinates  $Oxy$ . Suppose that:

1. Hessian matrix  $H$  of  $f(x, y)$ ,  $H = \begin{bmatrix} \frac{\partial^2 f}{\partial x^2} & \frac{\partial^2 f}{\partial x \partial y} \\ \frac{\partial^2 f}{\partial x \partial y} & \frac{\partial^2 f}{\partial y^2} \end{bmatrix}$  is known a priori.
2. The coordinates  $Oxy$  is rotated to  $Ox'y'$  by an counterclockwise angle  $\theta$ ; see Figure 3-16.

Let us compute the Hessian matrix  $H'$  of  $f$  in  $Ox'y'$

$$H' = \begin{bmatrix} \frac{\partial^2 f}{\partial x'^2} & \frac{\partial^2 f}{\partial x' \partial y'} \\ \frac{\partial^2 f}{\partial x' \partial y'} & \frac{\partial^2 f}{\partial y'^2} \end{bmatrix}.$$

We have

$$\begin{bmatrix} x \\ y \end{bmatrix} = \begin{bmatrix} \cos \theta & -\sin \theta \\ \sin \theta & \cos \theta \end{bmatrix} \begin{bmatrix} x' \\ y' \end{bmatrix} = \begin{bmatrix} x' \cos \theta - y' \sin \theta \\ x' \sin \theta + y' \cos \theta \end{bmatrix}.$$

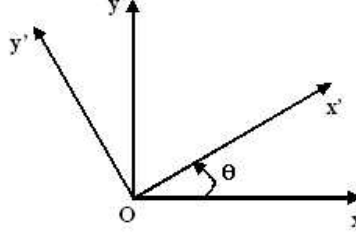


Figure 3-16: The coordinates  $Oxy$  is rotated to  $Ox'y'$  by a counterclockwise angle  $\theta$ .

Thus,

$$\frac{\partial f}{\partial x'} = \frac{\partial f}{\partial x} \frac{\partial x}{\partial x'} + \frac{\partial f}{\partial y} \frac{\partial y}{\partial x'} = \frac{\partial f}{\partial x} \cos \theta + \frac{\partial f}{\partial y} \sin \theta,$$

$$\frac{\partial f}{\partial y'} = \frac{\partial f}{\partial x} \frac{\partial x}{\partial y'} + \frac{\partial f}{\partial y} \frac{\partial y}{\partial y'} = \frac{\partial f}{\partial x} (-\sin \theta) + \frac{\partial f}{\partial y} \cos \theta.$$

Then

$$\begin{aligned} \frac{\partial^2 f}{\partial x'^2} &= \frac{\partial}{\partial x'} \left( \frac{\partial f}{\partial x'} \right) = \frac{\partial}{\partial x'} \left[ \frac{\partial f}{\partial x} \cos \theta + \frac{\partial f}{\partial y} \sin \theta \right] \\ &= \cos \theta \left[ \frac{\partial^2 f}{\partial x^2} \frac{\partial x}{\partial x'} + \frac{\partial^2 f}{\partial x \partial y} \frac{\partial y}{\partial x'} \right] + \sin \theta \left[ \frac{\partial^2 f}{\partial y^2} \frac{\partial y}{\partial x'} + \frac{\partial^2 f}{\partial y \partial x} \frac{\partial x}{\partial x'} \right] \\ &= \frac{\partial^2 f}{\partial x^2} \cos^2 \theta + \frac{\partial^2 f}{\partial x \partial y} \sin (2\theta) + \frac{\partial^2 f}{\partial y^2} \sin^2 \theta. \end{aligned} \quad (3.26)$$

Similarly,

$$\frac{\partial^2 f}{\partial y'^2} = \frac{\partial^2 f}{\partial x^2} \sin^2 \theta - \frac{\partial^2 f}{\partial x \partial y} \sin (2\theta) + \frac{\partial^2 f}{\partial y^2} \cos^2 \theta, \quad (3.27)$$

and

$$\begin{aligned} \frac{\partial^2 f}{\partial x' \partial y'} &= \frac{\partial}{\partial x'} \left( \frac{\partial f}{\partial y'} \right) = \frac{\partial}{\partial x'} \left[ \frac{\partial f}{\partial x} (-\sin \theta) + \frac{\partial f}{\partial y} \cos \theta \right] \\ &= -\sin \theta \left[ \frac{\partial^2 f}{\partial x^2} \frac{\partial x}{\partial x'} + \frac{\partial^2 f}{\partial x \partial y} \frac{\partial y}{\partial x'} \right] + \cos \theta \left[ \frac{\partial^2 f}{\partial y \partial x} \frac{\partial x}{\partial x'} + \frac{\partial^2 f}{\partial y^2} \frac{\partial y}{\partial x'} \right] \\ &= -\frac{1}{2} \frac{\partial^2 f}{\partial x^2} \sin (2\theta) + \frac{\partial^2 f}{\partial x \partial y} \cos (2\theta) + \frac{1}{2} \frac{\partial^2 f}{\partial y^2} \sin (2\theta). \quad \diamond \end{aligned} \quad (3.28)$$

## Chapter 4

# Inhomogeneous Object Segmentation

As a first definition, image segmentation is to partition the image into its constituent parts which correspond to separated objects. One then may think of the extraction of object boundaries, where simple edge detectors like gradient-based and second-order derivative-based operators [50] or a more elaborated approach like Canny edge detector [18] are widely used. However, an edge detector is usually not suitable for extracting object boundaries due to many reasons. Firstly, extracted edges do not always correspond to object boundaries. For example, one may think of texture. Secondly, edge detectors usually yield discontinued edges whereas objects are necessarily separated by closed contours. So post-processing tasks are needed to link discontinued edges, which are complex and prone to be erroneous. Finally, edge detectors depend on the local information in a neighborhood of a pixel. Being local is sometimes advantageous, yet in many cases, the global view of the object appearance is of significant clues. Therefore, image segmentation in general is different from edge detection. The former is to provide regions, represented by closed boundaries, not edges.

*Region growing* [13, 50] is one of the simple techniques that provide regions. Starting with a set of seed points, the algorithm successively appends to each seed point its neighboring pixels that share similar image features like intensity, texture, or color, etc. to form larger regions. It is an iterative process that stops when all pixels are processed. The algorithm can be regarded as a heuristic minimization for the Mumford-Shah functional (see Chapter 2) where the energy decreases while the regions are growing. Therefore, just like its energy optimization counterpart, region growing suffers from the sensitivity to seed selection as the initial condition, which can lead to under- or over-growing.

On the other hand, since it was first introduced in [57], active contour (AC) has attracted a large amount of researches and become one of the most widely used techniques in image segmentation. One advantage of AC models is that they are always closed, yielding continuous object boundaries, which no longer requires post-processing tasks to connect discontinued segments. Parametric ACs depend on the parameterizations of the contours and thus cannot naturally handle topological changes whereas geometric ACs can, making themselves suitable for applications where the number of objects in an image is not known in advance.

In general, geometric ACs are evolved under the level-set framework

$$\frac{\partial \phi}{\partial t} = \underbrace{b\kappa |\nabla \phi|}_{\text{CurvatureBased}} + \underbrace{V_N |\nabla \phi|}_{\text{NormalDirection}} + \underbrace{\vec{S} \cdot \nabla \phi}_{\text{VectorFieldBased}} \quad (4.1)$$

where  $\kappa$  is the Euclidean curvature and  $b$ ,  $V_N$ , and  $\vec{S}$  are three parameters determining the velocity and direction of the evolution. The curvature-based force is to smooth the curve; the normal direction force shrinks or expands the curve along its normal direction; and the external vector field-based force acts as a translation operator. Depending on how to choose those three parameters, we have different AC models such as the (original) *Geometric AC*, the *Geodesic AC*, the *GVF Geometric AC* (shortly, GVF-Geo AC), and the *Chan-Vese (CV) AC* as introduced in Chapter 2 and summarized in Table 4.1.

Table 4.1: Level-set parameters of the classical AC models.

	$b$	$V_N$	$\vec{S}$
Geometric	$g(\mathbf{x})$	$V_0 g(\mathbf{x})$	$\vec{0}$
Geodesic	$g(\mathbf{x})$	$V_0 g(\mathbf{x})$	$\nabla g$
GVF-Geo	$g(\mathbf{x})$	$V_0 K(\mathbf{x}) g(\mathbf{x})$	$g(\mathbf{x})(1 -  K(\mathbf{x}) )[\hat{u}, \hat{v}]$
CV	$\gamma$	$V_0 + (I - c_{in})^2 - (I - c_{out})^2$	$\vec{0}$

$\gamma$  and  $V_0$  are constants,  $g(\mathbf{x})$  an edge function, e.g.,  $g(\mathbf{x}) = e^{-\frac{1}{\sigma_e^2} |\nabla I_\sigma(\mathbf{x})|^2}$  with  $\sigma_e$  a scaling factor,  $[\hat{u}, \hat{v}]$  the GVF, and  $K(\mathbf{x})$  a function depending on the curve normal and the GVF.

## 4.1 Problems of Chan-Vese Active Contours

We can see from Table 4.1 that the first three models depend heavily on the edge function  $g(|\nabla I_\sigma|^2)$ , making themselves prone to be trapped in false edges caused by noises. This can be alleviated by performing smoothing with larger  $\sigma$ , yet it in turn leads to inexact results because edges are smoothed as well. The CV AC, on the other hand, does not depend on  $g$  (this gives it the name “without-edge AC”) but on the homogeneity assumption, i.e., image features within a segment should be similar. In this case, the image  $I$  is assumed to consist of two segments with approximately piecewise-constant intensities. The CV “fitting” term (2.52) is an approximation of the Mumford - Shah functional and rewritten here for readable convenience

$$F(C) = F_1(C) + F_2(C) = \int_{inside(C)} |I(\mathbf{x}) - c_{in}|^2 d\mathbf{x} + \int_{outside(C)} |I(\mathbf{x}) - c_{out}|^2 d\mathbf{x} \quad (4.2)$$

where  $c_{in}$  and  $c_{out}$  are respectively the average intensities inside and outside the variable curve  $C$ . Compared to the other three AC models, the CV AC can detect the objects more exactly since it does not need to smooth the initial image (via the edge function  $g(|\nabla I_\sigma|^2)$ ), even if it is very noisy. In other words, this model is more robust to noise; see

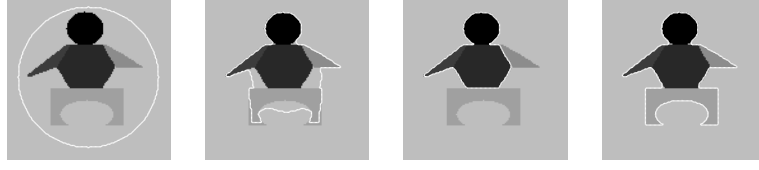


Figure 4-1: CV AC's failure on capturing an inhomogeneous object,  $\text{cpu} = 58\text{s}$ . Left to right: initial ( $F(C) = 645$ ), intermediate (312), final (34), and desired position (197). The plot of  $F(C)$  at every iteration is given in Figure 4-2.

Sections 4.3.7 and 4.3.8. This model was also shown to provide a relaxed initial position requirement [24].

However, the convergence of the CV AC depends on the homogeneity of the segmented objects. When the inhomogeneity becomes large like in carpal bones or knee bones, the CV AC provides unsatisfactory results. To address this, let us consider a synthetic image (size  $128 \times 128$ ) with an inhomogeneous object having five different parts over the bright background as shown in Figure 4-1. The image intensity is scaled on the range  $[0, 1]$ , with 1 the brightest. The CV fitting term  $F(C)$  is calculated at each iteration during the evolution and plotted in Figure 4-2. As expected, the curve moves in the direction of decreasing  $F(C)$  and stops when  $F(C)$  reaches a minimum value, which is  $F(C^*) = 34$  (at iteration number 16) in this case. Nevertheless, this is not the “desirable” result, whose minimum fitting term is  $F(C^{des}) = 197$ . Clearly, the desirable minimum here is larger (more local) than the practically resulting minimum  $F(C^*)$ .

## 4.2 Density Distance Augmented Chan-Vese Active Contours (Aug. CV AC)

From the above example, we can see that the global minimum of the CV energy functional does not always guarantee the desirable results, especially when a segment is highly

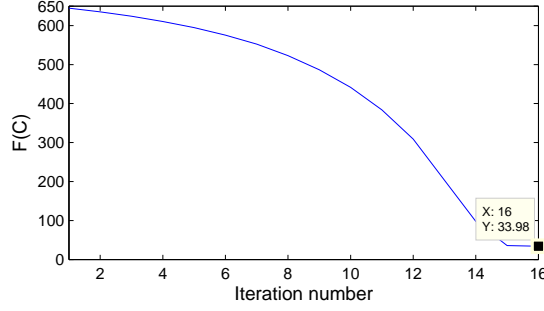


Figure 4-2: CV fitting term  $F(C)$  at every iteration of the CV AC evolution process. The obtained minimum ( $\approx 34$ ) is not the “desirable” one ( $\approx 197$ ).

inhomogeneous. To provide flexibility in searching for the desirable minimum (which is often neither the most local nor global), Li and Yezzi [67] proposed a dual-front AC model with the active region’s width as a controlling factor. The model is an iterative process consisting of the active region relocation and the dual front evolution which is another iterative process, demanding a high computational cost.

Alternatively, this section presents a novel model, called *Density distance augmented Chan-Vese Active Contour* (Aug. CV AC) to tackle the problem of CV AC. The reason CV AC fails is that in this model, a segment is represented by only its mean value, which is not sufficient for a highly inhomogeneous object. Hence, the proposed model uses the whole density function instead of only the mean value. The intrinsic knowledge incorporated here is that distinct organs shall generate distinct configurations in a medical image, i.e., I assume that the density function of one organ should be different from that of another one. The difference between density functions, given by the Bhattacharyya distance [55], is reflected as an additional energy term into the CV fitting term  $F(C)$  in order to balance the differences within every segment and the distances between separate segments. By properly weighting the two terms, the new evolution flow, which is implemented in a level-set framework, can flexibly drive the contour towards the desirable position without the

overhead required by the iterative dual-front evolution. If one considers segmentation as a classification problem, the proposed flow searches for a classifier that provides optimal classification errors since it both minimizes the error within one class and maximizes the distances between classes.

Although there are alternative measures defining the distance between probability distributions such as the Fisher ratio, the Kullback-Leibler divergence [63], the Bhattacharyya distance is chosen for both its better performance in applications of signal selection as observed in [55] and its simple analytical form. Specifically, in the active contour framework, the Bhattacharyya distance between the density functions inside and outside the curve  $C$ , i.e.,  $p_{in}(z)$  and  $p_{out}(z)$ ,  $z \in \mathbb{R}^n$ , is defined as  $[-\log B(C)]$  where  $B(C) \equiv B = \int_{\mathbb{R}^n} \sqrt{p_{in}(z)p_{out}(z)}dz$  and thus the maximization of this distance is equivalent to the minimization of  $B(C)$ . The additional term  $B(C)$  is incorporated as

$$E_0(C) = \beta F(C) + (1 - \beta)B(C) \quad (4.3)$$

where  $\beta \in [0, 1]$ . Note that to be comparable to the  $F(C)$  term, in practice,  $B(C)$  is multiplied by the area of the image because its value is always within the interval  $[0, 1]$  whereas  $F(C)$  is calculated based on the integral over the image plane. As usual [24], one regularizes the solution by constraining the length of the curve and the area of the region inside it, yielding the total energy functional as

$$E(C) = \gamma \text{Length}(C) + V_0 \text{Area}(\text{inside}(C)) + \beta F(C) + (1 - \beta)B(C) \quad (4.4)$$

where  $\gamma$  and  $V_0$  are non-negative constants.

The intuition behind the proposed model,  $\inf_C E(C)$ , is that we seek for a curve which is regular (the first two terms) and partitions the image into two regions such that the differences within each region are minimized (the  $F(C)$  term) and the distance between the two regions is maximized (the  $B(C)$  term).

For the level-set formulation, let us define  $\phi$  as the level-set function,  $I : \Omega \rightarrow \mathcal{Z} \subset \mathbb{R}^n$  as a certain image feature such as intensity, color, texture, or a combination thereof, and

$H(\cdot)$  and  $\delta_0(\cdot)$  as the Heaviside and the Dirac functions respectively.

$$H(u) = \begin{cases} 1, & \text{if } u \geq 0 \\ 0, & \text{if } u < 0 \end{cases} \quad \delta_0(u) = \frac{d}{du}H(u). \quad (4.5)$$

The energy functional can then be rewritten as

$$\begin{aligned} E(\phi) = & \gamma \int_{\Omega} |\nabla H(\phi(\mathbf{x}))| d\mathbf{x} + V_0 \int_{\Omega} H(-\phi(\mathbf{x})) d\mathbf{x} \\ & + \beta \left[ \int_{\Omega} |I(\mathbf{x}) - c_{in}|^2 H(-\phi(\mathbf{x})) d\mathbf{x} + \int_{\Omega} |I(\mathbf{x}) - c_{out}|^2 H(\phi(\mathbf{x})) d\mathbf{x} \right] \\ & + (1 - \beta) \int_{\mathcal{Z}} \sqrt{p_{in}(z)p_{out}(z)} dz \end{aligned} \quad (4.6)$$

where

$$p_{in}(z) = \frac{\int_{\Omega} \delta_0(z - I(\mathbf{x})) H(-\phi(\mathbf{x})) d\mathbf{x}}{\int_{\Omega} H(-\phi(\mathbf{x})) d\mathbf{x}} \quad p_{out}(z) = \frac{\int_{\Omega} \delta_0(z - I(\mathbf{x})) H(\phi(\mathbf{x})) d\mathbf{x}}{\int_{\Omega} H(\phi(\mathbf{x})) d\mathbf{x}}. \quad (4.7)$$

In a general form, it reads

$$E(\phi) = \underbrace{\int_{\Omega} f(\phi, \phi_{x_1}, \phi_{x_2}, \dots, \phi_{x_n}) d\mathbf{x}}_{\tilde{F}(\phi)} + (1 - \beta)B(\phi) \quad (4.8)$$

where  $\mathbf{x} = [x_1, x_2, \dots, x_n] \in \mathbb{R}^n$ ,  $\phi_{x_i} = \frac{\partial \phi}{\partial x_i}$ ,  $i = \overline{1..n}$ ,  $B(\phi) = \int_{\mathcal{Z}} \sqrt{p_{in}(z)p_{out}(z)} dz$ , and  $f = \gamma \delta_0(\phi) |\nabla \phi| + V_0 H(-\phi) + \beta |I - c_{in}|^2 H(-\phi) + \beta |I - c_{out}|^2 H(\phi)$ .

The first variation (w.r.t  $\phi(\mathbf{x})$ ) is given by

$$\frac{\delta E}{\delta \phi} = \frac{\delta \tilde{F}}{\delta \phi} + (1 - \beta) \frac{\delta B}{\delta \phi}. \quad (4.9)$$

Using Euler-Lagrange equation, one has

$$\frac{\delta \tilde{F}}{\delta \phi} = \frac{\partial f}{\partial \phi} - \sum_{i=1}^n \frac{\partial}{\partial x_i} \frac{\partial f}{\partial \phi_{x_i}} = \delta_0(\phi) [-V_0 - \beta(I - c_{in})^2 + \beta(I - c_{out})^2 - \gamma \kappa]. \quad (4.10)$$

On the other hand,

$$\frac{\delta B}{\delta \phi} = \frac{1}{2} \int_{\mathcal{Z}} \left( \frac{\partial p_{in}(z)}{\partial \phi} \sqrt{\frac{p_{out}(z)}{p_{in}(z)}} + \frac{\partial p_{out}(z)}{\partial \phi} \sqrt{\frac{p_{in}(z)}{p_{out}(z)}} \right) dz \quad (4.11)$$

where  $p_{in}(z)$  and  $p_{out}(z)$  are given in (4.7). Differentiating them w.r.t  $\phi(\mathbf{x})$ , one obtains

$$\frac{\partial p_{in}(z)}{\partial \phi} = \frac{\delta_0(\phi)}{A_{in}} [p_{in}(z) - \delta_0(z - I)] \quad \frac{\partial p_{out}(z)}{\partial \phi} = \frac{\delta_0(\phi)}{A_{out}} [\delta_0(z - I) - p_{out}(z)] \quad (4.12)$$

where  $A_{in}$  and  $A_{out}$  are respectively the areas inside and outside the contour and are given by

$$A_{in} = \int_{\Omega} H(-\phi(\mathbf{x})) d\mathbf{x} \quad A_{out} = \int_{\Omega} H(\phi(\mathbf{x})) d\mathbf{x}. \quad (4.13)$$

Substituting (4.12) into (4.11) and taking some simple modifications, one obtains

$$\frac{\delta B}{\delta \phi} = \delta_0(\phi) V(\mathbf{x}) \quad (4.14)$$

where

$$V(\mathbf{x}) = \frac{B}{2} \left( \frac{1}{A_{in}} - \frac{1}{A_{out}} \right) + \frac{1}{2} \int_{\mathcal{Z}} \delta_0(z - I(\mathbf{x})) \left( \frac{1}{A_{out}} \sqrt{\frac{p_{in}(z)}{p_{out}(z)}} - \frac{1}{A_{in}} \sqrt{\frac{p_{out}(z)}{p_{in}(z)}} \right) dz. \quad (4.15)$$

Combining (4.9), (4.10), and (4.14), one can derive the first variation of  $E(\phi)$  as

$$\frac{\partial E}{\partial \phi} = \delta_0(\phi) [-\gamma\kappa - V_0 - \beta(I - c_{in})^2 + \beta(I - c_{out})^2 + (1 - \beta)V]. \quad (4.16)$$

Hence, the evolution flow associated with minimizing the energy functional in (4.6) is given by

$$\begin{aligned} \frac{\partial \phi}{\partial t} &= -\frac{\delta E}{\delta \phi} \\ &= \delta_0(\phi) \left\{ \gamma\kappa + V_0 + \beta [(I - c_{in})^2 - (I - c_{out})^2] \right. \\ &\quad \left. - (1 - \beta) \left[ \frac{B}{2} \left( \frac{1}{A_{in}} - \frac{1}{A_{out}} \right) + \frac{1}{2} \int_{\mathcal{Z}} \delta_0(z - I) \left( \frac{1}{A_{out}} \sqrt{\frac{p_{in}}{p_{out}}} - \frac{1}{A_{in}} \sqrt{\frac{p_{out}}{p_{in}}} \right) dz \right] \right\}. \end{aligned} \quad (4.17)$$

### 4.2.1 Implementation

There are a couple of possible regularizations of function  $H$  (and  $\delta_0$ ) [24, 145] which determine the number of level curves that the evolution flow for  $\phi$  acts on. Some regularizations make the flow acts on a few level curves around the zero level set  $\{\phi(\mathbf{x}) = 0\}$  whilst some others acts on all level curves. In this model,  $\delta_0(\phi)$  is replaced by  $|\nabla\phi|$  so that the evolution is extended to all level sets of  $\phi$  as suggested in [145].

The pseudo-code for the proposed algorithm can be outlined as follows:

- $k = 0$ , initialize  $\phi^k$  by  $\phi_0$ .
- Compute the mean values  $c_{in}$  and  $c_{out}$ .
- Compute  $p_{in}(z)$  and  $p_{out}(z)$  according to (4.7).
- Compute  $A_{in}$  and  $A_{out}$  by (4.13).
- Evolve the curve using (4.17) to obtain  $\phi^{k+1}$ .
- Reinitialize  $\phi$  as the signed distance function of the current curve (see [89] for details).
- Check whether convergence is met. If not,  $k = k + 1$  and go back to the second step.

### 4.2.2 Preliminary results

Let us get back to the phantom image in the example in Section 4.1. Figure 4-3 shows the results of the Aug. CV AC with various  $\beta$  values. The object is correctly detected with a large range of  $\beta$  while neither of the two extremum cases ( $\beta = 0$  and  $\beta = 1$ ) succeeds. Figure 4-4 plots the energy minimization process where  $\beta = 0.5$  for a comparison with that in Figure 4-2. The “desirable” minimum  $F(C^{des}) = 197$  was successfully found.

Figure 4-5 shows the segmentation results for a real CT image. We can see that the CV AC provides unsatisfactory result (the inner region is excluded due to its intensity similarity to the background’s) whereas the proposed model can capture the whole bone

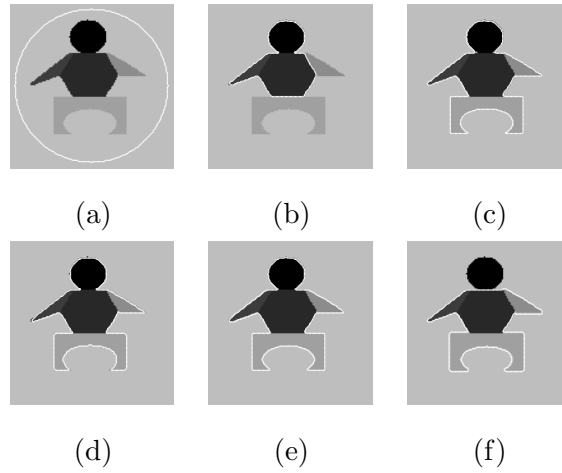


Figure 4-3: Results of the Aug. CV AC applied on the example image in Figure 4-1 using various values of  $\beta$ : (a) initial curve in white, (b) final curve with  $\beta = 1.0$  (purely the CV term),  $\text{cpu} = 57s$ , (c)  $\beta = 0.8$ ,  $\text{cpu} = 21s$ , (d)  $\beta = 0.5$ ,  $\text{cpu} = 71s$ , (e)  $\beta = 0.3$ ,  $\text{cpu} = 18s$ , and (f)  $\beta = 0.0$  (purely the Bhattacharyya term),  $\text{cpu} = 25s$ . The whole body is segmented correctly with a large range of  $\beta$ , i.e., (c)-(e).

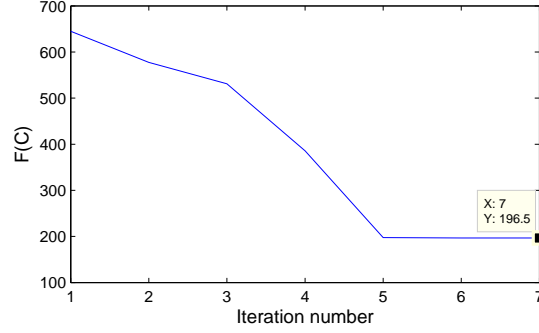


Figure 4-4: CV fitting term  $F(C)$  at every iteration of the Aug. CV AC evolution process with  $\beta = 0.5$ . The “desirable” minimum is found.

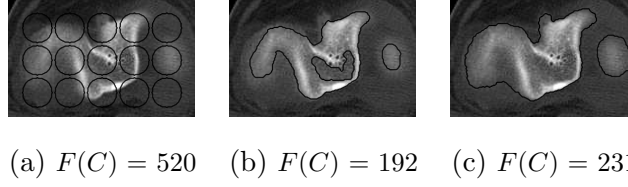


Figure 4-5: Segmentation result for a CT image (size  $120 \times 190$ ). (a) Initial, (b) CV AC,  $\text{cpu} = 72s$ , and (c) Aug. CV AC,  $\text{cpu} = 179s$ .

region although the former reaches the smaller value of energy term ( $F(C) = 192$  as compared to 231). This again proves that the global minimum is not always the desirable one.

In summary, this section presents a novel active contour model, called the Aug. CV AC. The model incorporates into the CV energy functional the Bhattacharyya distance between the density functions inside and outside the curve to drive it towards a “desirable” minimum which is often not the global one. The evolution flow of the proposed model is derived using the level-set framework, making itself inherit advantages of a geometric AC such as topology adaptability. The experimental results with both synthetic and real medical images show that the Aug. CV AC overcomes limitations of the CV AC

when dealing with inhomogeneous objects. It is also possible to see that the cpu time of the new model is comparable to or even less than that of the CV AC despite the higher computational cost. This is due to the fact that the additional evolving term helps to move the curve faster towards convergence. Its effectiveness in medical image segmentation is further evaluated in the next section using larger data sets of CT bone images, acquired in a clinical setting.

### 4.3 Application: Bone Segmentation From CT Images

Along with the advancements in medical imaging modalities such as ultrasound, magnetic resonance imaging (MRI) and computed tomography (CT), medical image analysis has drastically increased its importance in clinical procedures [101]. Current research works can be classified into four categories according to their purposes: enhancement, registration, visualization, and segmentation of the images. *Image enhancement* [25] deals with yielding more accurate images with improved contrast and reduced noise. *Image registration* [31] is an essential technique for multi-modality imaging where MRI, SPECT, PET, or angiography could be registered to each other to complement information. For instance, the complementary information such as soft-tissue information from MRI could be added to CT or vascular data to the anatomical MRI. *Image visualization* [112] is to provide more effective viewing of complex structures or information of human body. *Image segmentation* deals with an extraction of targeted regions of interests (ROIs) from the original image with minimum human interaction. Nowadays, due to increasing computing power, a combination of these research topics is integrated into the computer-aided surgery planning or the image-guided surgery system [101].

In computer-assisted orthopedic surgery, automatic image segmentation, especially *automatic bone segmentation* from CT imagery, is a critical but challenging component. Challenges are twofold: in developing good segmentation algorithms and in automating

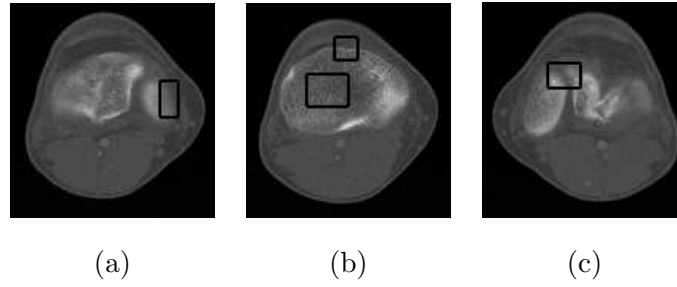


Figure 4-6: Typical CT bone images with challenging obstacles for accurate segmentation such as (a) weak edges, (b) gaps and texture areas, and (c) blurred inter-bone regions as indicated with boxes.

them. The former has three main hindrances: i) inhomogeneous bone structures, ii) low contrast edges, and iii) overlapping intensity values of bones, whereas the latter is even more challenging because it requires high performance to be obtained with minimal *user interactions* such as image-dependent initialization or prior information about the number of bones and/or their shapes. Inhomogeneous regions are due to the nature of bone structure in which the outer layer (i.e., cortical bone) is denser than the inner one (i.e., spongy bone). As a result, the cortical bone appears brighter in CT images while the spongy bone is darker and sometimes textured. Moreover, during image acquisition process, small gaps can exist in the bone surfaces where blood vessels go through. Also, when the boundaries of two bone regions are close to each other, they tend to be diffused, making the background pixels between them brighter and thus lower contrast. The boxes in Figure 4-6 indicate these challenging characteristics.

There have been several attempts including global thresholding, region growing [2], region competition [147], atlas-based [37], artificial intelligence, watershed segmentation approaches, and various combinations thereof as surveyed in [130, 115]. Most of the methods have shown success in certain anatomical structures where they have been optimized such as carpal bones [115], acetabulum and femoral head [148], spinal canal [17], pelvis [141, 37],

vertebrae [76], ribs [120], and phalanx bones [105]. In [130], two methods were validated on knee bone segmentation, which is also the subject of this study. The first one is a four-step process [56] which contains region-growing using local adaptive thresholds, discontinued-boundary closing, anatomically oriented boundary adjustment, and manual correction. The other one is a seeded edge-detection and tracing algorithm [141] where initial seeds are obtained by thresholding in intensity histograms. The aforementioned methods often require several steps with certain degrees of user interaction, especially additional tasks are in need to close discontinued object boundaries.

On the other hand, traditional snakes and many modified versions have also been used for bone segmentation. In [103], the authors incorporated region-based image features to the snakes model of Kass et al. [57], which was edge-based, to improve its convergence and dependence on initial position and to reduce its sensitivity to noise. Sharing the same idea, Pardo et al. [94] introduced new region potential term which did not rely on prior knowledge about image statistics. Although the integration of edge and region information made the model more robust to noise and permitted a more precise segmentation of bones, the automatic selection of relative weighting between edge and region terms remains an unsolved problem. In another work [115], Sebastian et al. combined conventional approaches such as bubbles active contours [124], region growing, region competition, and morphological operations in a unified framework. Specifically, from initialized seeds, region growing was taken place under the evolution implementation of bubbles. The growth of seeds was also modulated by the inter-seed skeleton-mediated competition between neighbor regions. The method inherited the advantages of each individual approach to overcome the discretization drawbacks of the region competition method, the convergence problems and initial placement sensitiveness of curve evolution methods. Nevertheless, it had limited performance in case of narrow and diffused inter-bone spaces. Ballerini and Bocchi [7] proposed the use of multiple genetic snakes whose energy minimization was

based on the Genetic Algorithms (GA) which helped to tackle the initialization problem. However, the method required much user interaction in determining the energy weights and the functionals governing the snake behavior.

Although those modified AC models can overcome the drawbacks of conventional ones in some particular situations, they are still far from the automatic bone segmentation procedure that requires high accuracy, initialization insensitivity, and topology adaptability (i.e., automatic splitting and merging ability to capture multiple objects). This section presents the evaluations of five recently developed AC models, namely the Geometric AC, the Geodesic AC, the GVF-Geo AC, the CV AC, and the Aug. CV AC, in extracting knee bones from CT images in comparison against 3D-DOCTOR software<sup>1</sup>, which is considered as a semi-automatic method. Other models that incorporate prior knowledge about object shape [110, 30, 126] or texture [92] are not considered since they require a training stage and thus are hardly automated and cannot fairly compared. The motivation here is to find the most appropriate technique that produces highest segmentation accuracy with least user interaction. From a clinical perspective, the development of such an algorithm is of great value since it can significantly reduce the amount of time a practitioner spends to inspect and modify the results of a more or less automatic segmentation. Knee bones are chosen as the regions of interest because they have all segmentation challenges as described above. Together with both qualitative and quantitative evaluations on real CT images, the influences of noise and contrast are also investigated with simulated data.

### 4.3.1 Parameter setting and tuning

There are four parameters for the above-mentioned AC models:  $\sigma$ ,  $\sigma_e$ ,  $V_0$ , and  $\nu$ .  $\sigma$  determines the width of the smoothing Gaussian kernel used in the edge function  $g$  and is

---

<sup>1</sup>A commercial software (Able software Corp., <http://www.ablesw.com/3d-doctor/>), approved by FDA (US Food and Drug Administration) for medical imaging and visualization applications and currently used by leading hospitals, medical schools, and research organizations around the world.

chosen small enough to retain minute details. It is fixed as  $\sigma = 0.3$  for all experiments. The rest are chosen depending on each specific case. Decreasing  $\sigma_e$  helps to detect weak edges but in turn traps the contour in false edges that are caused by noise. Since  $V_0$  constantly moves the contour along its normal direction regardless of its current position, increasing  $V_0$  will speed up the evolution but can march the contour over weak edges. So,  $\sigma_e$  and  $V_0$  should be large for noisy images and vice versa.  $\nu$  weights the length constraint of the CV and the Aug. CV ACs. If we have to detect all or as many objects as possible and of any size, then  $\nu$  should be small. If we have to not detect smaller objects (like points, due to noises), then  $\nu$  has to be larger.

In practice, some preliminary testing are needed for a new set of images with similar characteristics. In my experiments, I estimate the noise and contrast levels of one or two images from a testing set to provide an initial guess of the parameter set based on the above guidelines. Then I use a coarse to fine scheme to obtain the “best” parameters based on both visual evaluation and quantitative measures.

### 4.3.2 Testing data

Three testing data sets, named Contrast, Noisy, and Real CT images, are used to test the five techniques on CT bone segmentation. The last consists of sixteen CT images covering the knee regions of one person; see Figure 4-7. The former two are of synthetic data made to see how these techniques behave at different contrast and noise levels respectively and were created as follows. First, a medical expert was asked to carefully extract bone regions from the sixteen CT images, which will be used as “ground truths” later on. Then, each extracted bone region was placed on ten homogenous backgrounds with various intensities to obtain ten images having contrast varying from 1% to 20%. Here, I adopt the definition of contrast introduced by Morrow et al. [81]

$$C_t = \frac{B_0 - B}{B_0 + B} 100\% \quad (4.18)$$

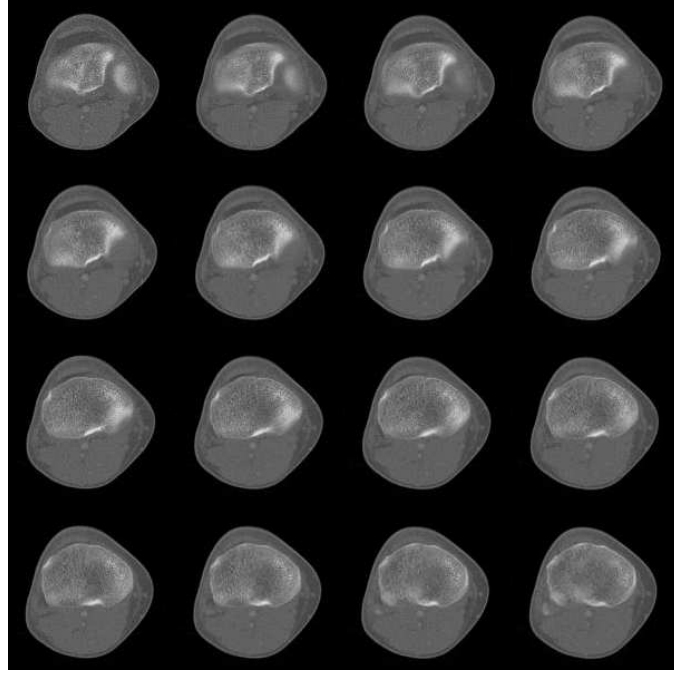


Figure 4-7: Real CT data set.

where  $B$  and  $B_0$  are respectively the mean intensity of the object (foreground) and the surrounding region (background) in an image. In my real CT data, the contrast is about 8%. To my knowledge, CT images with the contrast of 20% are quite clear and those with the contrast of 1% are beyond the worst case. By this way, I had a *Contrast* data set consisting of 160 images (16 images  $\times$  10 contrast levels each) with typical CT bone segmentation challenges. Similarly, placing extracted bones on noisy backgrounds with SNR of 50, 40, 30, 20, and 10 dB, I formed a *Noisy* data set consisting of 80 images (16 images  $\times$  5 noise levels each). Images with SNR of 10 dB are beyond the worst case.

### 4.3.3 Evaluation method

For quantitative comparison, I use two error measures,  $\epsilon_1$  and  $\epsilon_2$ , defined as

$$\begin{aligned}\epsilon_1 &= 1 - \frac{\#(\textit{Extracted regions} \cap \textit{True regions})}{\#(\textit{Extracted regions} \cup \textit{True regions})} \\ \epsilon_2 &= \text{Hd}(\textit{Extracted boundaries}, \textit{True boundaries})\end{aligned}\quad (4.19)$$

where  $\#$  denotes the number of points in a set and  $\text{Hd}(A, B)$  the Hausdorff distance between two polygons  $A$  and  $B$ .

$$\text{Hd}(A, B) = \max\{h(A, B), h(B, A)\} \quad (4.20)$$

where  $h(A, B) = \max_{a \in A} \min_{b \in B} \{dist(a, b)\}$  and  $dist(a, b)$  is the Euclidean distance between points  $a$  and  $b$ .

The error measure  $\epsilon_1$  quantifies the relative overlap between the segmented and the true regions and  $\epsilon_2$  measures the difference of the extracted and the true contours. The former provides a global goodness of the result whereas the latter determines how much details of the object shape are captured. The more these measures are close to zero, the better the segmentation is.

### 4.3.4 Sensitivity to $\beta$

Similar to the experiment in the previous section, the sensitivity of the Aug. CV AC with respect to the  $\beta$  parameter is investigated here using the real CT data set. The result is shown in Figure 4-8. It can be seen that this AC model is not much  $\beta$ -sensitive since it provides small error measures with many  $\beta$  values ranging from 0.4 to 0.7.

### 4.3.5 Topology-adaptability and initialization-insensitivity

I consider an AC to be topology-adaptable if it can naturally split and merge to capture multiple objects in the image without any prior information and initialization-insensitive

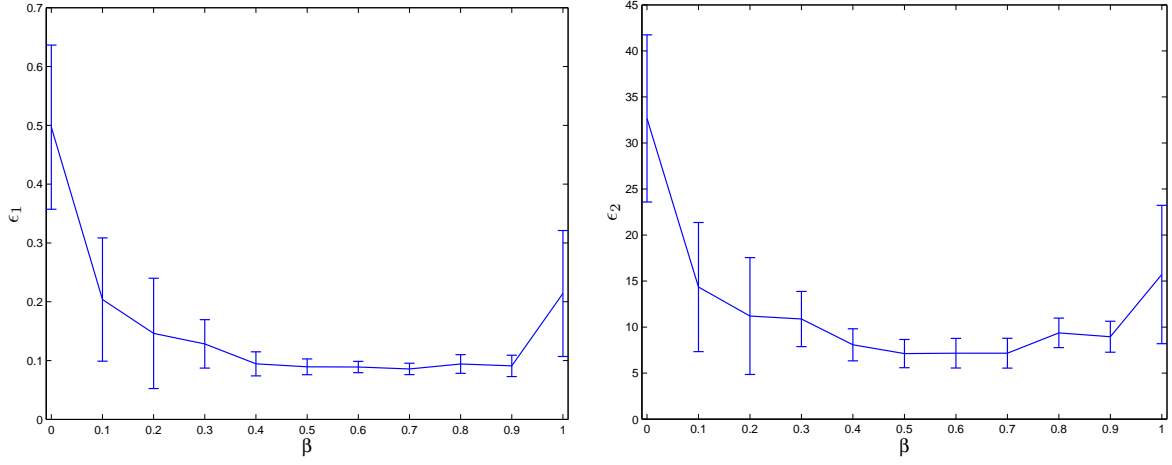


Figure 4-8: Performances of Aug. CV AC applied on the real CT data set vs.  $\beta$  values.

if it can do that regardless of its initial position and size. Figure 4-9 shows three types of initialization and the corresponding results. Note that only one representative result is shown for three models: Geometric, Geodesic, and GVF-Geo AC because they yield similar results for this synthetic image. We can see that these three models work well with the first two types (the initial contour is totally outside or inside the objects) but fail with the last one (initial contour is cross the objects) whereas the CV and the Aug. CV ACs succeed with all three types. The reason is that the former three models can only move in a fixed direction based on the sign of the constant  $V_0$ ; see (2.43)-(2.51). When  $V_0$  is positive (negative), the whole contour will shrink (expand) all the time. Meanwhile, the image-dependent term  $[V_0 + (I - c_1)^2 - (I - c_2)^2]$  in the CV AC flow (2.56) (or similar term in the Aug. CV AC flow (4.17)) allows the contour to expand and shrink where appropriate because it can be negative at some points and positive at others.

### 4.3.6 Experiment 1 - Performance at Various Contrast Levels

In this experiment, I use the Contrast data set to evaluate the performance of the AC models with respect to different contrast levels. The parameter settings are chosen as

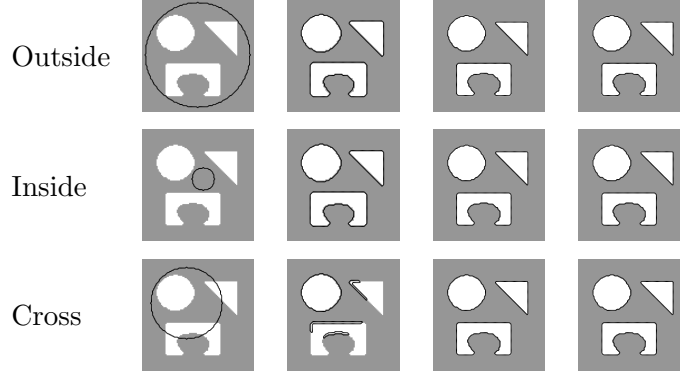


Figure 4-9: Topology-adaptability and initialization-sensitivity. Left to right: initialization, Geometric/Geodesic/GVF-Geo, CV, and Aug. CV ACs. The latter two models succeed with all three types of initialization whereas the others fail with the cross-type.

Table 4.2: Parameter settings for Experiment 1.

Geometric ( $\sigma_e^2, V_0$ )	Geodesic ( $\sigma_e^2, V_0$ )	GVF-Geo ( $\sigma_e^2, V_0$ )	CV ( $\nu, V_0$ )	Aug. CV ( $\nu, V_0$ )
0.2, 0.5	0.2, 0.7	0.2, 0.5	1, 0	1, 0

described in Section 4.3.1 and shown in Table 4.2. Figure 4-10 shows visual results from two samples having contrast of 13% and 1%, respectively. Mean values of error measures as functions of contrast level are plotted in Figure 4-11 and corresponding SD values are given in Table 4.3. We can see that although the CV AC performs well when image contrast is high (more than 15%), its performance decreases very quickly with the contrast whereas the others are more robust to contrast level. One possible reason is that the homogeneity assumption of CV model cannot be guaranteed in low contrast images, i.e., many parts of the object resemble background and thus are likely to be misclassified (see Figure 4-10, lower row).

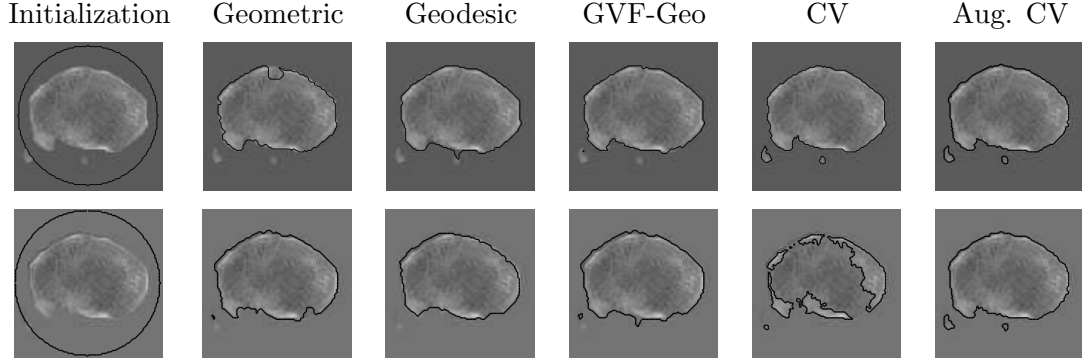


Figure 4-10: Performance at various contrast levels. Upper row: contrast = 13% and lower row: contrast = 1%.

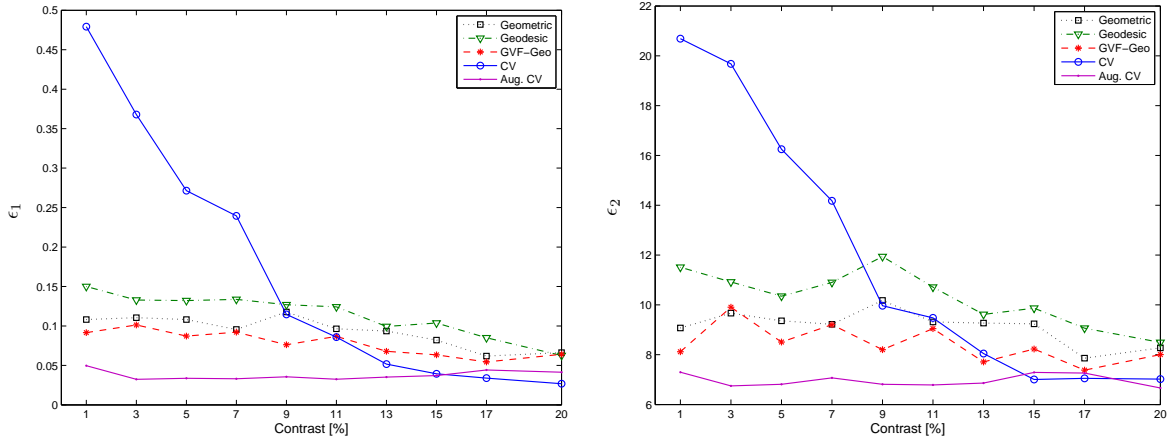


Figure 4-11: Plots of error means vs. contrast levels. Mean value is calculated over sixteen samples at each contrast level.

Table 4.3: Mean and SD of error measures for Contrast data set.

	Contrast [%]	Mean (SD)				
		Geometric	Geodesic	GVF-Geo	CV	Aug. CV
$\epsilon_1$	1	0.108 (0.074)	0.150 (0.095)	0.092 (0.029)	0.479 (0.055)	0.050 (0.041)
	3	0.110 (0.082)	0.133 (0.070)	0.101 (0.060)	0.368 (0.159)	0.032 (0.022)
	5	0.108 (0.096)	0.132 (0.077)	0.087 (0.046)	0.271 (0.109)	0.034 (0.024)
	7	0.096 (0.078)	0.134 (0.088)	0.092 (0.079)	0.239 (0.105)	0.033 (0.020)
	9	0.118 (0.105)	0.127 (0.088)	0.076 (0.051)	0.115 (0.080)	0.036 (0.026)
	11	0.096 (0.100)	0.124 (0.109)	0.087 (0.066)	0.086 (0.036)	0.032 (0.024)
	13	0.094 (0.073)	0.099 (0.080)	0.068 (0.038)	0.052 (0.034)	0.035 (0.024)
	15	0.082 (0.070)	0.104 (0.072)	0.063 (0.051)	0.039 (0.023)	0.037 (0.023)
	17	0.062 (0.039)	0.085 (0.054)	0.054 (0.018)	0.034 (0.018)	0.044 (0.029)
	20	0.066 (0.033)	0.063 (0.021)	0.064 (0.042)	0.027 (0.012)	0.041 (0.024)
$\epsilon_2$	1	9.07 (3.47)	11.51 (3.51)	8.12 (1.47)	20.69 (2.41)	7.30 (2.09)
	3	9.67 (3.84)	10.92 (3.39)	9.91 (3.60)	19.68 (4.39)	6.75 (1.76)
	5	9.36 (3.52)	10.35 (3.10)	8.51 (2.79)	16.25 (6.63)	6.81 (1.75)
	7	9.22 (3.07)	10.90 (3.49)	9.20 (3.51)	14.18 (6.77)	7.07 (2.53)
	9	10.18 (4.14)	11.94 (3.82)	8.20 (2.79)	9.97 (6.72)	6.81 (1.80)
	11	9.31 (3.94)	10.71 (4.09)	9.05 (2.86)	9.48 (4.48)	6.78 (1.85)
	13	9.27 (3.02)	9.62 (3.77)	7.71 (2.17)	8.05 (2.23)	6.86 (1.89)
	15	9.24 (3.69)	9.87 (3.40)	8.23 (3.23)	7.00 (1.88)	7.29 (2.24)
	17	7.86 (2.25)	9.07 (3.31)	7.38 (1.81)	7.05 (1.85)	7.26 (2.21)
	20	8.27 (1.89)	8.49 (2.48)	8.00 (2.69)	7.02 (1.86)	6.66 (3.01)

Table 4.4: Parameter settings for Experiment 2.

SNR [dB]	Geometric ( $\sigma_e^2, V_0$ )	Geodesic ( $\sigma_e^2, V_0$ )	GVF-Geo ( $\sigma_e^2, V_0$ )	CV ( $\nu, V_0$ )	Aug. CV ( $\nu, V_0$ )
10	20, 3	20, 7	30, 7	1, 0	1.5, 0
20	3, 3	3, 9	4, 6	0.5, 0	1, 0
30	1, 1	2, 1	3, 1	0.05, 0	0.5, 0
40	1, 1	2, 1	3, 1	0.05, 0	0.5, 0
50	1, 1	2, 1	3, 1	0.05, 0	0.5, 0

#### 4.3.7 Experiment 2 - Performance at Various Noise Levels

Similarly, the Noisy data set is used to evaluate the performance of the five AC models with respect to various noise levels. The parameter settings are shown in Table 4.4 and sample results in Figure 4-12. Quantitative comparisons for this testing data set are given in Figure 4-13 and Table 4.5. The Geometric, the Geodesic, and the GVF-Geo ACs provide similar performance to the others when noise level is low. However, they tend to get stuck in false edges caused by noise when noise level increases due to the edge function  $g$ . On the other hand, the CV and the Aug. CV are more robust to noise as they do not depend on the edge information.

#### 4.3.8 Experiment 3 - Performance with Real Data

The aim of this experiment is to investigate how the AC models work with real CT images in comparison against 3D-DOCTOR software. The parameter settings are shown in Table 4.6.

Figure 4-14 shows segmentation results for two sample CT images. It can be seen that the first three models, i.e., the Geometric, the Geodesic, and the GVF-Geo ACs, do not generate visually satisfactory results whereas the other two do. The Geometric AC

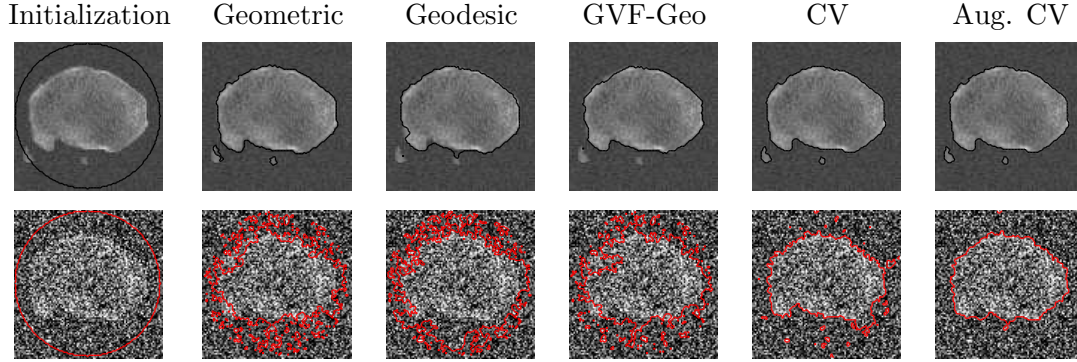


Figure 4-12: Performance at various noise levels. Upper row: SNR = 30dB, lower row: 10dB.

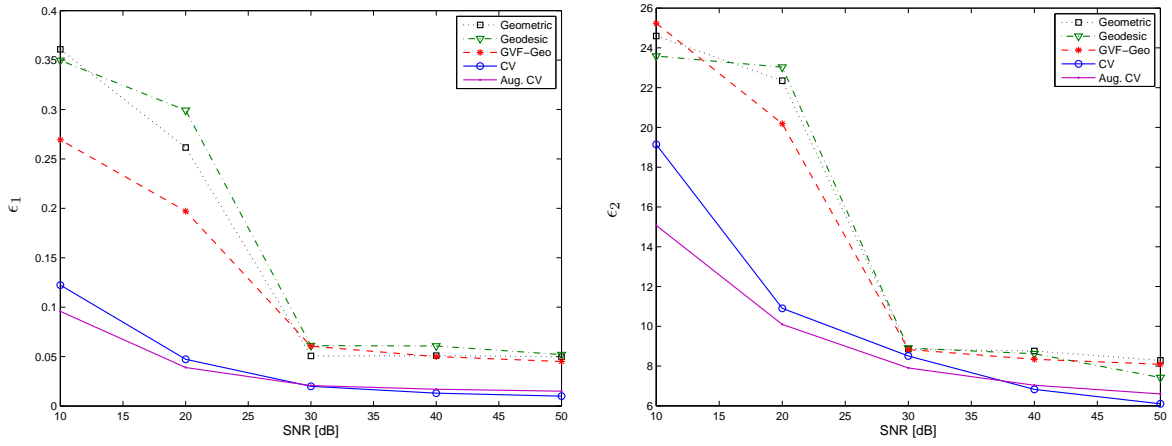


Figure 4-13: Plots of error means vs. SNR. Mean value is calculated over sixteen samples at each SNR.

Table 4.5: Mean and SD of error measures for Noisy data set.

	SNR [dB]	Mean (SD)				
		Geometric	Geodesic	GVF-Geo	CV	Aug. CV
$\epsilon_1$	10	0.361 (0.090)	0.350 (0.087)	0.269 (0.067)	0.122 (0.031)	0.096 (0.024)
	20	0.262 (0.065)	0.299 (0.075)	0.197 (0.049)	0.047 (0.012)	0.039 (0.010)
	30	0.051 (0.013)	0.061 (0.015)	0.061 (0.016)	0.020 (0.018)	0.021 (0.003)
	40	0.051 (0.020)	0.061 (0.011)	0.050 (0.010)	0.013 (0.005)	0.017 (0.007)
	50	0.050 (0.011)	0.052 (0.009)	0.045 (0.012)	0.010 (0.004)	0.015 (0.004)
$\epsilon_2$	10	24.597 (5.402)	23.586 (5.403)	25.237 (5.406)	19.144 (4.785)	15.074 (3.771)
	20	22.347 (5.594)	23.030 (5.594)	20.186 (5.051)	11.903 (3.117)	10.094 (3.270)
	30	8.854 (2.213)	8.902 (2.231)	8.833 (2.362)	8.507 (2.381)	7.906 (2.235)
	40	8.756 (3.217)	8.620 (2.457)	8.339 (3.215)	6.827 (2.103)	7.036 (2.671)
	50	8.282 (3.031)	7.421 (1.543)	8.090 (2.232)	6.102 (2.142)	6.597 (1.328)

Table 4.6: Parameter settings for Experiment 3.

Geometric	Geodesic	GVF-Geo	CV	Aug. CV
$(\sigma_e^2, V_0)$	$(\sigma_e^2, V_0)$	$(\sigma_e^2, V_0)$	$(\nu, V_0)$	$(\nu, V_0)$
0.2, 0.4	0.2, 0.8	0.2, 1.2	0.5, 0	5.0, 0

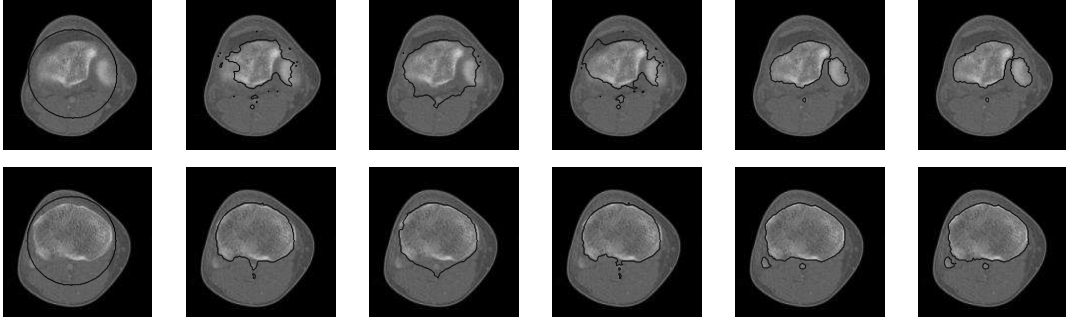


Figure 4-14: Two sample segmentation results. Left to right: initialization, Geometric, Geodesic, GVF-Geo, CV, and Aug. CV ACs' results.

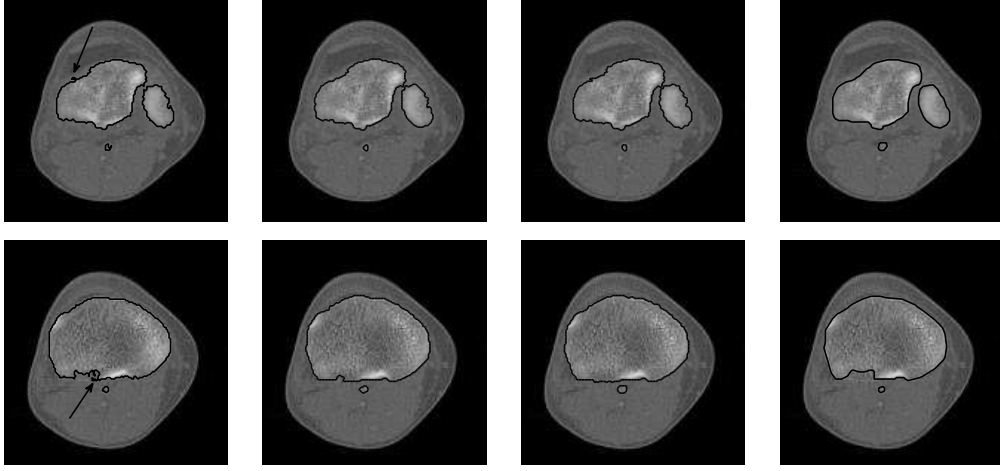


Figure 4-15: Qualitative comparison. Left to right: 3D-DOCTOR, CV AC, Aug. CV AC, and the “ground truth”. The contours from the 3D-DOCTOR software contain cross-over parts whereas the others do not.

tends to pass through some areas in the bone boundary where the stopping function  $g$  is not small enough due to weak edges and/or gaps. In this situation, the Geodesic AC with the extra stopping term  $\nabla g \cdot \nabla \phi$  (2.49) can pull back the boundary-passing-through contour in weak-edge regions but it is likely to get stuck in false edges caused by noises. The GVF-Geo AC model (2.51) has similar problem. Differently, the CV and the Aug. CV AC models can successfully find the bone boundaries. The qualitative comparisons between these two models and the 3D-DOCTOR software are presented in Figure 4-15. These ACs yield better results in the sense that the contours are smoother and do not contain cross-over parts as the commercial software does.

The mean and standard deviation of the error measures for sixteen images are given in Table 4.7. Among the five AC models, the last two perform well and their performance is comparable to that of the 3D-DOCTOR software. The smaller  $\epsilon_2$  value of these models over the commercial software can be explained by the better boundary shapes they yielded.

Table 4.7: The mean and SD of error measures of AC models and the 3D-DOCTOR software performed on sixteen CT images.

	Geome.	Geode.	GVF-Geo.	CV	Aug. CV	3D-DOCTOR
$\epsilon_1$	0.184 (0.078)	0.155 (0.078)	0.147 (0.068)	0.086 (0.016)	0.089 (0.013)	0.078 (0.012)
$\epsilon_2$	12.74 (3.24)	10.84 (3.92)	11.62 (3.31)	6.76 (1.54)	7.12 (1.53)	7.49 (1.49)

#### 4.3.9 Discussions

The feasibility of five different AC models on automatic bone segmentation from CT images have been examined. By “automatic”, I mean that a model can provide high accuracy with minimal user interactions such as initialization and prior information about the number of bones and/or their shapes. Due to the level-set framework, all five models showed their ability to capture complex shapes without any prior information. Furthermore, in case of ideal image (see Figure 4-9), the CV AC and the Aug. CV AC’s performances were invariable to different initial contour positions and sizes. Before assessing the performance on real images, I investigated the influence of noise and contrast level on the segmentation result, which is why Experiments 1 and 2 were carried on. Results show that the Geometric, the Geodesic, and the GVF-Geo ACs are robust to image contrast but sensitive to noise whereas the CV AC is robust to noise but sensitive to image contrast. Meanwhile, the Aug. CV AC is robust to both noise and contrast levels.

The purpose of Experiment 3 is to evaluate the accuracy of the models on real patient data, acquired in a clinical setting. Results show that the first three models provide unsatisfactory results when dealing with bones that have smooth edges and/or gaps. On the other hand, the CV AC and the Aug. CV AC models show excellent ability in segmenting bone regions with the error measures comparable to those of the 3D-DOCTOR software. These models even generate visually better results than the commercial software does in the sense that the contours are smoother and do not contain cross-over parts which cannot truthfully represent real bone structures.

From these findings, I consider that the CV and the Aug. CV AC models offer best potential for the automatic bone segmentation work. Moreover, when dealing with low contrast images, the latter is more suitable.

## Chapter 5

# Contributions and Conclusions

*All intelligent thoughts have already been thought;  
what is necessary is only to try to think them again.*

Johann Wolfgang von Goethe (1749-1832).

Variational methods have emerged for the past two decades as a pool of high-level mathematical tools for image processing as opposed to the conventional low-level mathematical operators which are largely heuristic and thus often lack of proofs of correctness. However, they have shown to suffer from limited performance in medical applications since medical images are very noisy and low contrast. This thesis has dealt with knowledge-incorporated variational methods in medical image processing in order to improve their performance and robustness. The work contributes to both technical and medical research community. As contributions to technical researches, it has appended to the variational methods two models to be used in enhancement and segmentation each.

It has presented a novel approach for Hessian eigen-analysis with emphasis on preserving junctions while enhancing curvilinear structures. The conventional Hessian-based enhancement approaches first estimate the object's direction and the direction orthogonal to it using the Hessian eigenvectors and then calculate the second-derivatives in those

directions to determine the object's structure (in fact, these directional derivatives are reflected by the Hessian eigenvalues and thus one does not need to calculate them again). The proposed approach replaces the directional estimation using Hessian eigenvectors with the directional information available in directional images obtained using the DDFB. By this way, the proposed approach can distinguish all line-like structures at junctions and bifurcations. At these configurations, one will obtain different directions and thus different second derivatives that are different from the Hessian eigenvalues (of the original image). Also, directional decomposition alleviates the removal of NUI which is usually a challenge for correct enhancement algorithm. Normally, NUI is directly removed from the input image using homomorphic filter whose parameter tuning suffers from a compromise between the amount of NUI removal (desirable) and that of the high-frequency noise enhancement (undesirable). In the proposed approach, homomorphic filter is not applied on the input image, but on its directional components. Here, a set of homomorphic filters is used; each is optimized matched with its corresponding directional image. This new arrangement provides a better control on the parameter of individual homomorphic filter.

In segmentation, the thesis has introduced a new energy functional that can help to efficiently detect inhomogeneous objects. The proposed energy incorporates a density distance term into the Chan-Vese fitting term (which is an approximation of the Mumford-Shah functional). The minimization of the energy is mathematically solved using the calculus of variations and the gradient descent, leading to a new active contour model, called Aug. CV AC, whose evolution flow is implemented using the level-set framework. The resulting AC searches for a segmentation solution where not only the dissimilarity within each segment is minimized but also the distance between distinct segments is maximized. This reduces the misclassification errors in cases of inhomogeneous objects where the minimal dissimilarity within each object by its own cannot guarantee the desirable result. Incorporating another term into an existing term means that a new weighting

parameter is introduced. On one hand, it makes the flow more flexible in finding desirable result. On the other hand, the additional parameter requires more effort from the user to select suitable values for it. Fortunately, the proposed model has been shown to be rather insensitive to the weighting parameter, i.e., it can converge with a large range of the parameter's value.

As contributions to medical researches, the thesis has applied the two proposed models to vessel enhancement and bone segmentation, respectively. Enhancement of blood vessels reflected in X-ray angiograms or angiography images is necessary yet challenging for their accurate visualization and quantification which play a significant role in a number of clinical procedures such as stenosis diagnosis or neurosurgical planning and performing. The challenges are due to the fact that vessel's width varies much, leading to various local contrast level reflected in the image and due to non-uniform illumination caused by the image acquisition. Extensive experiments have been performed in a number of synthetic and real medical images to evaluate the performance of the proposed filter in comparison with two conventional filters, i.e., the Frangi's and the Shikata's. The proposed filter has shown its effectiveness in enhancing vessels of various sizes and types with more robustness to noise. Furthermore, it overcomes the junction suppression problem of the conventional ones. Although the error caused by junction suppression may be small, it can yield serious clinical problem due to the resulting discontinued vessel tree.

Similar to vessel enhancement, automatic bone segmentation from CT images is a critical but challenging task. Challenges are twofold: in developing a good segmentation algorithm and in automating it. The former is difficult because of the inhomogeneous nature of bones and the noisy and low contrast characteristics of CT images. By automating the segmentation algorithm, it is meant that high accuracy is obtained with minimal user interactions. The thesis has evaluated the performances of five segmentation models, namely the Geometric AC, the Geodesic AC, the GVF-Geo AC, the CV AC, and

the proposed Aug. CV AC, in many synthetic and real CT images. Findings show that the Aug. CV AC possesses many advantages such as topology adaptability, initialization insensitivity, and noise and low-contrast robustness. The last advantage ensures high accuracy to be obtained whereas the former two make it less dependent on user interaction. This model also provides superior results compared to a commercial software in a set of medical images. Therefore, the Aug. CV AC is the most suitable candidate for automatic bone segmentation. From a clinical perspective, the development of such an algorithm is of great value since it can significantly reduce the amount of time a practitioner spends to inspect and modify the results of a more or less automatic segmentation.

According to Goethe, one does not have many chances to create any reasonably new thought as all truly wise thoughts had already been thought thousands of time before. There might be several arguments against this absolute statement, e.g., one may doubt whether people in the Renaissance period talked about topics like internet or genetics. Nonetheless, the statement is reasonable in the sense that a new thought cannot pop up from nowhere but is based on several thoughts that have been thought before. At least, this has been proven by the history of science. Revolutions are really rare in science; instead, breakthroughs are usually obtained via an evolution process in which many small ideas are sum up together. This statement is also true for this thesis: the idea of incorporating prior knowledge for better performance is not new. However, this idea has been re-thought in a different way: intrinsic knowledge obtained from medical objects is naturally embedded into the proposed methods without additional efforts of defining external models like in conventional approaches. In this sense, novel contributions of the thesis are significant.

# Publications

## Patents

1. P. T. H. Truc, M. Khan, S. Y. Lee, and T.-S. Kim, Vessel Enhancement using Decimation-free Directional Filter Bank, US Patent (application number: 11/892,030).

## Journals

1. P. T. H. Truc, M. Khan, Y.-K. Lee, S. Y. Lee, T.-S. Kim, Vessel Enhancement Filter using Directional Filter Bank, Comput. Vis. Image Understand. 113 (1), pp. 101-112, 2009 (doi:10.1016/j.cviu.2008.07.009).
2. P. T. H. Truc, T.-S. Kim, Y. H. Kim, Y.-K. Lee, and S. Y. Lee, Automatic Bone Segmentation from CT Images using Chan-Vese Multiphase Active Contour, Journal of Biomedical Engineering Research, vol. 28 (6), pp. 713-720, 2007.
3. M. Khan, P. T. H. Truc, R. Bahadur and S. Javed, Vessel Enhancement using Directional Features, Information Technology Journal 6 (6), pp. 851-857, 2007.
4. P. T. H. Truc, T.-S. Kim, Y.-K. Lee, S. Y. Lee, A study on the feasibility of Active Contours on CT bone segmentation, J. Digit. Imaging, under review.

## Conferences

1. P. T. H. Truc, S. Y. Lee, and T.-S. Kim, A Density Distance Augmented Chan-Vese Active Contour for CT Bone Segmentation, 30th Annual Int. Conf. of IEEE in Medicine and Biology Society (IEEE EMBC08), pp. 482-485, Vancouver, Canada, Aug. 2008.
2. P. T. H. Truc, M. Khan, S. Y. Lee, and T.-S. Kim, Vessel Enhancement in Angiography Images using Decimation-free Directional Filter Bank, IPCV'07, pp. 175-181, USA, Jun. 2007.
3. P. T. H. Truc, M. Khan, S. Y. Lee, and T.-S. Kim, A New Approach to Vessel Enhancement in Angiography Images, IEEE/ICME Int. Conf. on Complex Medical Engineering, pp. 878-884, Beijing, China, May 2007.
4. P. T. H. Truc, Y. H. Kim, Y.-K. Lee, S. Y. Lee, and T.-S. Kim, Evaluation of Active Contour-based Techniques toward Bone Segmentation from CT Images, World Congress on Medical Physics and Biomedical Engineering, pp. 2997-3000, Seoul, Korea, 2006.
5. Nguyen Duc Thang, P. T. H. Truc, Young-Koo Lee, Sungyoung Lee, and Tae-Seong Kim, 3-D Human Pose Estimation from 2-D Depth Images, Int. Conf. Ubiquitous Healthcare, Busan, Korea, Nov. 2008.
6. A. M. Khan, P. T. H. Truc, Y. K. Lee, and T.-S. Kim, A Tri-axial Accelerometer Sensor-based Human Activity Recognition via Augmented Signal Features and Hierarchical Recognizer, Int. Conf. Ubiquitous Healthcare, Busan, Korea, Nov. 2008.
7. J. J. Lee, Md. Zia Uddin, P. T. H. Truc, and T.-S. Kim, Spatiotemporal Depth Information-based Human Facial Expression Recognition Using FICA and HMM, Int. Conf. Ubiquitous Healthcare, Busan, Korea, Nov. 2008.

8. Jehad Sarkar, P.T.H. Truc, Y.-K. Lee, and S.Y. Lee, Statistical Language Modeling approach to Activity Recognition, Int. Conf. Ubiquitous Healthcare, Busan, Korea, Nov. 2008.
9. Md. Zia Uddin, J. J. Lee, P. T. H. Truc, and T.-S. Kim, Human Activity Recognition Using Independent Component Features from Depth Images, Int. Conf. Ubiquitous Healthcare, Busan, Korea, Nov. 2008.

# Bibliography

- [1] A. J. Abrantes and J. S. Marques. A class of constrained clustering algorithms for object boundary extraction. *IEEE Trans. Image Proc.*, 5:1507–21, 1996.
- [2] R. Adams and L. Bischof. Seeded region growing. *IEEE Trans. Patt. Anal. Mach. Intell.*, 16:641–7, 1994.
- [3] G. Agam, I. S.G. Armato, and C. Wu. Vessel tree reconstruction in thoracic CT scans with application to nodule detection. *IEEE Trans. Med. Imag.*, 24(4):486–99, Apr. 2005.
- [4] L. Alvarez, F. Guichard, P.-L. Lions, and J.-M. Morel. Axioms and fundamental equations in image processing. *Archive for Rational Mechanics and Analysis*, 123:199–257, 1993.
- [5] L. Alvarez, P. Lions, and J. Morel. Image selective smoothing and edge detection by nonlinear diffusion. *SIAM J. Numer. Anal.*, 29:845–66, 1992.
- [6] G. Aubert and L. Vese. A variational method for image recovery. *SIAM J. Appl. Math.*, 34:1948–79, 1997.
- [7] L. Ballerini and L. Bocchi. Multiple genetic snakes for bone segmentation. In *Applications of Evolutionary Computing: EvoWorkshops*, volume 2611 of *LNCS*, pages 346–56, 2003.
- [8] G. Bamberger and M. J. T. Smith. A filter bank for the directional decomposition of images - theory and design. *IEEE Trans. Sig. Proc.*, 40(4):882–93, 1992.
- [9] R. H. Bamberger. *The directional filter bank: A multirate filterbank for the directional decomposition of images*. PhD thesis, Georgia Institute of Technology, USA, Nov. 1990.

- [10] R. H. Bamberger. New subband decompositions and coders for image and video compression. In *IEEE Int. Conf. on Acoustics, Speech and Signal Processing*, pages 217–20, 1992.
- [11] R. H. Bamberger. New results on two and three dimensional directional filter banks. In *IEEE Twenty-Seventh Asilomar Conference on Signals, Systems and Computers*, volume 2, pages 1286–90, Nov. 1993.
- [12] R. H. Bamberger and M. J. T. Smith. A multirate filter bank based approach to the detection and enhancement of linear features in images. In *IEEE. Int. Conf. Acoustics, Speech and Signal Processing*, volume 4, pages 2557–60, Apr. 1991.
- [13] J. Beveridge, J. Griffith, R. Kohler, A. Hanson, and E. Riseman. Segmenting images using localized histograms and region merging. *Int. J. Comp. Vis.*, 2:311–52, 1989.
- [14] J. Bigün and G. H. Granlund. Optimal orientation detection of linear symmetry. In *Proc. First ICCV*, pages 433–8, 1987.
- [15] J. Bigün, G. H. Granlund, and J. Wiklund. Multidimensional orientation estimation with applications to texture analysis and optical flow. *IEEE Trans. Pattern Anal. Mach. Intell.*, 13:775–90, 1991.
- [16] A. Bruhn, J. Weickert, and C. Schnörr. Lucas/Kanade meets Horn/Schunck: Combining local and global optic flow methods. *Int. J. Comp. Vis.*, 61:211–31, 2005.
- [17] S. Burnett, G. Starschalla, C. Stevens, and Z. Liao. A deformable-model approach to semi-automatic segmentation of ct images demonstrated by application to the spinal canal. *Med. Phys.*, 21:251–63, 2004.
- [18] J. Canny. A computational approach to edge detection. *IEEE Trans. Patt. Anal. Mach. Intell.*, 8:679–98, 1986.
- [19] R. Carmona and S. Zhong. Adaptive smoothing respecting feature directions. *IEEE Trans. Image Proc.*, 7(3):353–8, 1998.
- [20] Caselles, F. Catte, T. Coll, and F. Dibos. A geometric model for active contours in image processing. *Numerische Mathematik*, 66:1–31, 1993.

- [21] V. Caselles, R. Kimmel, and G. Sapiro. Geodesic active contours. *Int. J. Comp. Vis.*, 22:61–79, 1997.
- [22] F. Catte, T. Coll, P. Lions, and J. Morel. Image selective smoothing and edge detection by nonlinear diffusion. *SIAM J. Numer. Anal.*, 29(1):182–93, 1992.
- [23] T. Chan and J. Shen. *Image Processing and Analysis - Variational, PDE, Wavelet, and Stochastic methods*. SIAM, Philadelphia, USA, 2005.
- [24] T. Chan and L. Vese. Active contours without edges. *IEEE Trans. Image Proc.*, 10:266–77, 2001.
- [25] D. Chang and W. Wu. Image contrast enhancement based on a histogram transformation of local standard deviation. *IEEE Trans. Med. Imag.*, 17(4):518–31, 1998.
- [26] H. Chen and J. Hale. An algorithm for MR angiography image enhancement. *MRM*, 33(4):534–40, Apr. 1995.
- [27] L. Cohen. On active contour models and balloons. *CVGIP: Image Und.*, 53:211–8, 1991.
- [28] L. Cohen and I. Cohen. Finite element methods for active contour models and balloons for 2D and 3D images. *IEEE Trans. Patt. Anal. Mach. Intell.*, 15(11):1131–47, 1993.
- [29] M. Crandall, H. Ishii, and P.-L. Lions. User’s guide to viscosity solutions of second order partial linear differential equations. *Bull. Am. Math. Soc.*, 27:1–67, 1992.
- [30] D. Cremers, F. Tischhauser, J. Weikert, and C. Schnorr. Diffusion snakes: introducing statistical shape knowledge into the Mumford-Shah functional. *Int. J. Comp. Vis.*, 50(3):295–313, 2002.
- [31] W. Crum, L. Griffin, D. Hill, and D. Hawkes. Zen and the art of medical image registration: correspondence, homology, and quality. *Neuroimage*, 20:1425–37, 2003.
- [32] R. Czerwinski, D. Jones, and W. O’Brien, Jr. An approach to boundary detection in ultrasound imaging. In *Proc. IEEE Ultrasonics Symposium*, pages 951–5, 1993.
- [33] R. Czerwinski, D. Jones, and W. O’Brien, Jr. Detection of lines and boundaries in speckle images-application to medical ultrasound. *IEEE Trans. Med. Imag.*, 18(2):126–36, 1999.

- [34] C. Davatzikos and J. L. Prince. An active contour model for mapping the cortex. *IEEE Trans. Med. Imag.*, 14:65–80, 1995.
- [35] Y. P. Du and D. L. Parker. Vessel enhancement filtering in three-dimensional MR angiograms using long-range signal correlation. *JMRI*, 7(2):447–50, 1997.
- [36] Y. P. Du, D. L. Parker, and W. L. Davis. Vessel enhancement filtering in three-dimensional MR angiography. *JMRI*, 5(3):353–9, 1995.
- [37] J. Ehrhardt, H. Handels, T. Malina, B. Strathmann, W. Plotz, and S. Poppl. Atlas-based segmentation of bone structures to support the virtual planning of hip operations. *Int. J. Med. Inform.*, 64:439–47, 2001.
- [38] S. Eiho and Y. Qian. Detection of coronary artery tree using morphological operator. In *IEEE Comput. Cardiol.*, pages 525–8, 1997.
- [39] C. Epstein and M. Gage. The curve shortening flow. In A. Chorin and A. Majda, editors, *Wave Motion: Theory, Modeling, and Computation*. Springer-Verlag, 1987.
- [40] European Carotid Surgery Trialists Collaborative Group. Randomised trial of endarterectomy for recently symptomatic carotid stenosis: Final results of the MRC European Carotid Surgery (ECST). *Lancet*, 351:1379–87, 1999.
- [41] B. L. Evans, R. H. Bamberger, and J. H. McCellan. Rules for multidimensional multirate structures. *IEEE Trans. on Signal Processing*, 42(4):762–71, Apr 1994.
- [42] L. C. Evans and J. Spruck. Motion of level sets by mean curvature I. *J. Diff. Geometry*, 33:635–81, 1991.
- [43] T. Fawcett. ROC graphs: Notes and practical considerations for researchers. Technical report, HP Laboratories, Palo Alto, USA, 2004.
- [44] L. Florack, B. Romeny, J. Koenderink, and M. Viergever. Scale and the differential structure of images. *Image Vis. Comput.*, 10(6):376–88, 1992.
- [45] W. Förstner and E. Gülch. A fast operator for detection and precise location of distinct points, corners and centres of circular features. In *Proc. ISPRS Intercommission Conference on Fast Processing of Photogrammetric Data*, pages 281–305, 1987.

- [46] A. Frangi, W. Niessen, R. Hoogeveen, T. van Walsum, and M. Viergever. Model-based quantitation of 3-D magnetic resonance angiographic images. *IEEE Trans. Med. Imag.*, 18(10):946–56, 1999.
- [47] A. Frangi, W. Niessen, P. Nederkoorn, J. Bakker, W. Mali, and M. Viergever. Quantitative analysis of vascular morphology from 3D MR angiograms: In vitro and in vivo results. *MRM*, 45:311–22, 2001.
- [48] A. Frangi, W. Niessen, K. Vincken, and M. Viergever. Multiscale vessel enhancement filtering. In *Medical Image Computing Computer-Assisted Intervention, LNCS*, volume 1496, pages 130–7, 1998.
- [49] G. Gerig, O. Kubler, R. Kikinis, and F. Jolesz. Nonlinear anisotropic filtering of mri data. *IEEE Trans. Med. Imag.*, 11:221–32, 1992.
- [50] R. Gonzalez and R. Woods. *Digital Image Processing*. Prentice Hall, New Jersey, USA, 2002.
- [51] C. L. Guyader and L. A. Vese. Self-repelling snakes for topology-preserving segmentation models. *IEEE Trans. Image Proc.*, 17(5):767–79, 2008.
- [52] E. M. Haacke, R. W. Brown, M. R. Thompson, and R. Venkatesan. *Magnetic Resonance Imaging: Physical Principles and Sequence Design*. Wiley, New York, 1999.
- [53] C. G. Harris and M. Stephens. A combined corner and edge detector. In *Proc. Fourth Alvey Vision Conference*, pages 147–52, 1988.
- [54] A. K. Jain. Partial differential equations and finite-difference methods in image processing, part 1: image representation. *J. Optimiz. Theory Appl.*, 23:65–91, 1977.
- [55] T. Kailath. The divergence and Bhattacharyya distance measures in signal selection. *IEEE Trans. Commun. Technol.*, 15:52–60, 1967.
- [56] Y. Kang, K. Engelke, and W. A. Kalender. A new accurate and precise 3-D segmentation method for skeletal structures in volumetric CT data. *IEEE Trans. Med. Imag.*, 22(5):586–98, 2003.
- [57] M. Kass, A. Witkin, and D. Terzopoulos. Snakes: active contour models. *Int. J. Comp. Vis.*, 1(4):321–31, 1988.

- [58] C. Kirbas and F. Quek. A review of vessel extraction techniques and algorithms. *ACM Computing Surveys*, 36(2):81–121, June 2004.
- [59] J. J. Koenderink. The structure of images. *Biol. Cyber.*, 50:363–70, 1984.
- [60] K. Krissian. Flux-based anisotropic diffusion applied to enhancement of 3-D angiogram. *IEEE Trans. Med. Imag.*, 21(11):1440–2, 2002.
- [61] K. Krissian, G. Malandain, and N. Ayache. Directional anisotropic diffusion applied to segmentation of vessels in 3D images. In *Scale-Space Theory in Computer Vision, LNCS*, pages 345–8, 1997.
- [62] K. Krissian, G. Malandain, N. Ayache, R. Vaillant, and Y. Troussset. Model-based detection of tubular structures in 3D images. *Comput. Vis. Image Und.*, 80(2):130–71, 2000.
- [63] S. Kullback and R. A. Leibler. On information and sufficiency. *Ann. Math. Statist.*, 22:79–86, 1951.
- [64] R. Kutka and S. Stier. Extraction of line properties based on direction fields. *IEEE Trans. Med. Imag.*, 15(1):51–8, 1996.
- [65] Leitner and Cinquin. Dynamic segmentation: Detecting complex topology 3D objects. In *Proc. of Eng. in Medicine and Biology Society*, 1991.
- [66] M. E. Leventon, W. Eric, L. Grimson, and O. Faugeras. Statistical shape influence in geodesic active contours. In *Proc. of the IEEE Conf. on CVPR*, pages 316–23, 2000.
- [67] H. Li and A. Yezzi. Local or global minima: Flexible dual-front active contours. *IEEE Trans. Patt. Anal. Mach. Intell.*, 29:1–14, 2007.
- [68] X. Li and T. Chen. Nonlinear diffusion with multiple edginess thresholds. *Pattern Recognition*, 27:1029–37, 1994.
- [69] T. Lindeberg. *Scale-Space Theory in Computer Vision*. Kluwer Academic, Dordrecht, Netherlands, 1994.
- [70] T. Lindeberg. Edge detection and ridge detection with automatic scale selection. In *IEEE Conf. on Computer Vision and Pattern Recognition (CVPR)*, pages 465–70, San Francisco, 1996.

- [71] C. Lorenz, I.-C. Carlsen, T. Buzug, C. Fassnacht, and J. Weese. A multi-scale line filter with automatic scale selection based on the Hessian matrix for medical image segmentation. *Proc. Scale-Space Theories in Computer Vision, LNCS*, 1252:152–63, 1997.
- [72] L. Lorigo, O. Faugeras, W. Grimson, Keriven, Kikinis, Nabavi, and C.-F. Westin. CURVES: Curve evolution for vessel segmentation. *Medical Image Analysis*, 5:195–206, 2001.
- [73] J. Malik, S. Belongie, T. Leung, and J. Shi. Contour and texture analysis for image segmentation. *Int. J. Comp. Vis.*, 43:7–27, 2001.
- [74] R. Malladi, J. A. Sethian, and B. C. Vemuri. Shape modeling with front propagation: a level set approach. *IEEE Trans. Patt. Anal. Mach. Intell.*, 17(2):158–75, 1995.
- [75] U. Massari and I. Tamanini. Regularity properties of optimal segmentation. *J. Reine Angew. Math.*, 420:61–84, 1991.
- [76] A. Mastmeyer, K. Engelke, C. Fuchs, and W. Kalender. A hierarchical 3D segmentation method and the definition of vertebral body coordinate systems for QCT of the lumbar spine. *Med. Image Anal.*, 10:260–77, 2006.
- [77] T. McInerney and D. Terzopoulos. T-snakes: Topology adaptive snakes. *Med. Image Anal.*, 4(2):73–91, 2000.
- [78] J. Melonakos, E. Pichon, S. Angenent, and A. Tannenbaum. Finsler active contours. *IEEE Trans. Patt. Anal. Mach. Intell.*, 30(3):412–23, 2008.
- [79] J. Morel and S. Solimini. Segmentation of images by variational methods: A constructive approach. *Rev. Math. Univ. Complut. Madrid*, 1:169–82, 1988.
- [80] J. Morel and S. Solimini. *Variational methods in Image Segmentation*. Basel, 1995.
- [81] W. M. Morrow, R. B. Paranjape, R. M. Rangayyan, and J. E. L. Desautels. Region-based contrast enhancement of mammograms. *IEEE Trans. Med. Imag.*, 11:392–406, 1992.
- [82] F. Mujica, J.-P. Leduc, R. Murenzi, and M. J. T. Smith. Spatio-temporal continuous wavelets applied to missile warhead detection and tracking. In *Proc. SPIE Visual Communication and Image Processing*, volume 3024, pages 787–98, Feb. 1997.

- [83] F. Mujica, R. Murenzi, J.-P. Leduc, and M. J. T. Smith. Robust object tracking in compressed image sequences. *SPIE Journal of Electronic Imaging*, 7:746–54, Oct. 1998.
- [84] D. Mumford and J. Shah. Optimal approximation by piecewise smooth functions and associated variational problems. *Commun. Pure Appl. Math.*, 42:577–685, 1989.
- [85] M. Wilkinson and M. Westenberg. Shape preserving filament enhancement filtering. In *Proc. Int. Conf. Medical Image Computing and Computer-Assisted Intervention, LNCS*, volume 2208, pages 770–7, Utrecht, The Netherlands, 2001.
- [86] M. Nitzberg and T. Shiota. Nonlinear image filtering with edge and corner enhancement. *IEEE Trans. Pattern Anal. Mach. Intell.*, 14:826–33, 1992.
- [87] North American Symptomatic Carotid Endarterectomy Trial (NASCET) Steering Committee. North American symptomatic carotid endarterectomy trial. *Stroke*, 22:711–20, 1991.
- [88] M. Orkisz, C. Bresson, I. Magnin, O. Champin, and P. Douek. Improved vessel visualization in MR angiography by nonlinear anisotropic filtering. *MRM*, 37(6):914–9, June 1997.
- [89] S. Osher and R. P. Fedkiw. *Level set methods and dynamic implicit surfaces*. Springer-Verlag, New York, USA, 2003.
- [90] S. Osher and L. Rudin. Feature-oriented image enhancement using shock filters. *SIAM J. Num. Anal.*, 27:919–40, 1990.
- [91] S. Osher and J. A. Sethian. Fronts propagating with curvature dependent speed: algorithms based on Hamilton-Jacobi formulations. *J. Comput. Phys.*, 79:12–49, 1988.
- [92] N. Paragios and R. Deriche. Geodesic active regions and level set methods for supervised texture segmentation. *Int. J. Comp. Vis.*, 46(3):223–47, 2002.
- [93] N. Paragios, O.M-Gottardo, and V. Ramesh. Gradient vector flow fast geometric active contours. *IEEE Trans. Patt. Anal. Mach. Intell.*, 26:402–7, 2004.
- [94] X. M. Pardo, M. J. Carreira, A. Mosquera, and D. Cabello. A snake for CT image segmentation integrating region and edge information. *Image Vis. Comput.*, 19:461–75, 2001.

- [95] C. H. Park, J. J. Lee, M. J. T. Smith, S. Park, and K. J. Park. Directional filter bank-based fingerprint feature extraction and matching. *IEEE Trans. on Circuits and Systems for Video Technology*, 14(1):74–85, Jan. 2004.
- [96] S. Park. *New Directional Filter Banks and Their Applications in Image Processing*. PhD thesis, Georgia Institute of Technology, USA, Nov. 1999.
- [97] S. Park, M. J. T. Smith, and J. J. Lee. Fingerprint enhancement based on the directional filter bank. In *IEEE Int. Conf. on Image Processing (ICIP'00)*, pages 793–6, Sept. 2000.
- [98] S. Park, M. J. T. Smith, and R. M. Mersereau. A new directional filter bank for image analysis and classification. *ICASSP*, 3:1417–20, 1999.
- [99] S. Park, M. J. T. Smith, and R. M. Mersereau. Improved structures of maximally decimated directional filter banks for spatial image analysis. *IEEE Trans. Image Processing*, 13(11):1424–31, Nov. 2004.
- [100] P. Perona and J. Malik. Scale-space and edge detection using anisotropic diffusion. *IEEE Trans. Pattern Anal. Mach. Intell.*, 12(7):629–39, 1990.
- [101] T. M. Peters. Image-guidance for surgical procedures. *Phys. Med. Biol.*, 51:505–40, 2006.
- [102] R. Poli and G. Valli. An algorithm for real-time vessel enhancement and detection. *Comput. Meth. Prog. Biomed.*, 52:1–22, 1996.
- [103] C. S. Poon and M. Braun. Image segmentation by a deformable contour model incorporating region analysis. *Phys. Med. Biol.*, 42:1833–41, 1997.
- [104] C. Price, P. Wambacq, and A. Oosterlink. Image enhancement and analysis with reaction-diffusion paradigm. *IEE Proc.*, 137:136–45, 1990.
- [105] A. J. Ramme, N. DeVries, N. A. Kallemyn, V. A. Magnotta, and N. M. Grosland. Semi-automated phalanx bone segmentation using the expectation maximization algorithm. *J. Digit. Imaging*, DOI: 10.1007/s10278-008-9151-y, Sep. 2008.
- [106] A. R. Rao and B. G. Schunck. Computing oriented texture fields. *CVGIP: Graphical Models and Image Processing*, 53:157–85, 1991.

- [107] N. Ray and S. T. Acton. Motion gradient vector flow: an external force for tracking rolling leukocytes with shape and size constrained active contours. *IEEE Trans. Med. Imag.*, 23(12):1466–78, 2004.
- [108] M. Rochery, I. H. Jermyn, and J. Zerubia. Higher order active contours. *Int. J. Comp. Vis.*, 69(1):27–42, 2006.
- [109] B. Ronemy. *Geometry Driven Diffusion in Computer Vision*. Kluwer, 1994.
- [110] M. Rousson and N. Paragios. Shape priors for level set representations. In *ECCV*, pages 78–92. Springer, 2002.
- [111] J. Russ. *The image processing handbook*. CRC Press, Boca Raton, 2nd edition, 1995.
- [112] P. Saiviroonporn, A. Robatino, J. Zahajszky, R. Kikinis, and F. Jolesz. Real-time interactive three-dimensional segmentation. *Acad. Radiol.*, 5:49–56, 1998.
- [113] G. Sapiro. From active contours to anisotropic diffusion: connections between the basic pde’s in image processing. In *Proc. IEEE ICIP*, New York, 1996.
- [114] Y. Sato, S. Nakajima, N. Shiraga, H. Atsumi, S. Yoshida, T. Koller, G. Gerig, and R. Kikinis. Three-dimensional multi-scale line filter for segmentation and visualization of curvilinear structures in medical images. *Med. Image Anal.*, 2(2):143–68, 1998.
- [115] T. Sebastian, H. Tek, J. Crisco, and B. Kimia. Segmentation of carpal bones from CT images using skeletally coupled deformable models. *Med. Image Anal.*, 7:21–45, 2003.
- [116] J. Sethian. *Level set methods = evolving interface in geometry, computer vision*. Cambridge University Press, New York, USA, 1996.
- [117] J. Shah. A common framework for curve evolution, segmentation, and anisotropic diffusion. In *Proc. IEEE CVPR*, 1996.
- [118] H. Shikata, E. A. Hoffman, and M. Sonka. Automated segmentation of pulmonary vascular tree from 3D CT images. In *Proc. SPIE Int. Symp. Medical Imaging*, volume 5369, pages 107–16, San Diego, CA, 2004.
- [119] J. Sporring, M. Nielsen, L. Florack, and P. Johansen, editors. *Gaussian scale-space theory*. Kluwer, 1997.

- [120] J. Staal, van Ginneken B, and M. A. Viergever. Automatic rib segmentation and labeling in CT scans using a general framework for detection, recognition, and segmentation of objects in volumetric data. *Med. Image Anal.*, 11:35–46, 2007.
- [121] G. Sundaramoorthi and A. Yezzi. Global regularizing flows with topology preservation for active contours and polygons. *IEEE Trans. Image Proc.*, 16(3):803–12, 2007.
- [122] G. Sundaramoorthi, A. Yezzi, and A. Mennucci. Sobolev active contours. *Int. J. Comp. Vis.*, 73(3):345–66, 2007.
- [123] R. Szeliski, D. Tonnesen, and D. Terzopoulos. Modeling surfaces of arbitrary topology with dynamic particles. In *Proc. CVPR*, pages 82–7, 1999.
- [124] H. Tek and B. Kimia. Volumetric segmentation of medical images by three-dimensional bubbles. *Computer Vision and Image Understanding*, 64:246–58, 1997.
- [125] R. Toledo, X. Orriols, X. Binefa, P. Radeva, J. Vitrià, and J. J. Villanueva. Tracking of elongated structures using statistical snakes. In *Proc. of the IEEE Conf. on CVPR*, pages 1157–62, 2000.
- [126] A. Tsai, A. Yezzi, A. Wells, C. Tempany, D. Tucker, A. Fan, W. Grimson, and A. Willsky. A shape-based approach to the segmentation of medical imagery using level sets. *IEEE Trans. Med. Imag.*, 22(2):137–54, 2003.
- [127] G. Turk. Generating synthetic textures using reaction-diffusion. *Comput. Graph.*, 25:289–98, 1991.
- [128] R. van den Boomgaard and J. van de Weijer. Robust estimation of orientation for texture analysis. In *Proc. Texture 2002, 2nd International Workshop on Texture Analysis and Synthesis*, 2002.
- [129] L. Vese and T. Chan. A multiphase level set framework for image segmentation using Mumford and Shah model. *Int. J. Comp. Vis.*, 50(3):271–93, 2002.
- [130] L. Wang, M. Greenspan, and R. Ellis. Validation of bone segmentation and improved 3-D registration using contour coherence in CT data. *IEEE Trans. Med. Imag.*, 25:324–34, 2006.

- [131] J. Weickert. A review of nonlinear diffusion filtering. In *Scale-space Theory in Computer Vision*, volume 1252 of *LNCS*, pages 3–28, 1997.
- [132] J. Weickert. Coherence-enhancing diffusion filtering. *Int. J. Comp. Vis.*, 31:111–27, 1999.
- [133] J. Weickert. Coherence-enhancing diffusion of colour images. *Image Vis. Comput.*, 17:199–210, 1999.
- [134] J. Weickert, S. Ishikawa, and A. Imiya. On the history of gaussian scale-space axiomatics. In J. Sporring, M. Nielsen, L. Florack, and P. Johansen, editors, *Gaussian scale-space theory*, pages 45–59. Kluwer, 1997.
- [135] R. Whitaker and S. Pizer. A multi-scale approach to nonuniform diffusion. *CVGIP: Image Understanding*, 57:99–110, 1993.
- [136] A. Witkin and M. Kass. Reaction-diffusion textures. *Comput. Graph.*, 25:289–308, 1991.
- [137] A. P. Witkin. Scale-space filtering. In *Proc. Int. Joint Conf. Artificial Intelligence*, pages 1019–22, 1983.
- [138] X. Xie and M. Mirmehdi. MAC: magnetostatic active contour model. *IEEE Trans. Patt. Anal. Mach. Intell.*, 30(4):632–46, 2008.
- [139] C. Xu and J. Prince. Snakes, shapes, and gradient vector flow. *IEEE Trans. Image Proc.*, 7:359–69, 1998.
- [140] C. Yan, S. Hirano, and Y. Hata. Extraction of blood vessel in CT angiography image aided by fuzzy logic. In *IEEE Proc. Int. Conf. Signal Processing*, pages 926–9, 2000.
- [141] W. Yao, P. Abolmaesumi, M. Greenspan, and R. Ellis. An estimation/correction algorithm for detecting bone edges in CT images. *IEEE Trans. Med. Imag.*, 24:997–1010, 2005.
- [142] A. Yezzi, S. Kichenassamy, A. Kumar, P. Olver, and A. Tannenbaum. A geometric snake model for segmentation of medical imagery. *IEEE Trans. Med. Imag.*, 16:199–209, 1997.
- [143] Y. You, W. Xu, A. Tannenbaum, and M. Kaveh. Behavioral analysis of anisotropic diffusion in image processing. *IEEE Trans. Image Process.*, 5:1539–53, 1996.

- [144] F. Zana and J.-C. Klein. Segmentation of vessel-like patterns using mathematical morphology and curvature evaluation. *IEEE Trans. Image Proc.*, 10:1010–9, 2001.
- [145] H.-K. Zhao, T. Chan, B. Merriman, and S. Osher. A variational level set approach to multiphase motion. *J. Comput. Phys.*, 127:179–95, 1996.
- [146] S. Zhu and D. Mumford. GRADE: Gibbs reaction and diffusion equations. In *Proc. IEEE ICCV*, pages 847–54, 1999.
- [147] S. Zhu and A. Yuille. Region competition: unifying snakes, region growing, and Bayes/MDL for multiband image segmentation. *IEEE Trans. Patt. Anal. Mach. Intell.*, 18:884–900, 1996.
- [148] R. Zoroofi, Y. Sato, and T. Sasama et al. Automated segmentation of acetabulum and femoral head from 3D CT images. *IEEE Trans. Inf. Technol. Biomed.*, 7:329–43, 2003.